

Active Cancellation of Tollmien-Schlichting Waves under Varying Inflow Conditions for In-Flight Application

Vom Fachbereich Maschinenbau
an der Technischen Universität Darmstadt
zur

Erlangung des Grades eines Doktor-Ingenieurs (Dr.-Ing.)
genehmigte

Dissertation

vorgelegt von

Bernhard Jochen Simon, M.Sc.

aus Offenbach am Main

Berichterstatter:	Prof. Dr.-Ing. Cameron Tropea
1. Mitberichterstatter:	Prof. Dr.-Ing. Sven Grundmann
2. Mitberichterstatter:	Prof. Dan Henningson
Tag der Einreichung:	27.03.2017
Tag der mündlichen Prüfung:	27.06.2017

Darmstadt 2017

Active Cancellation of Tollmien-Schlichting Waves under Varying Inflow Conditions for In-Flight Application

Bitte zitieren Sie dieses Dokument als:

URN: urn:nbn:de:tuda-tuprints-61614

URL: <http://tuprints.ulb.tu-darmstadt.de/id/eprint/6161>

Dieses Dokument wird bereitgestellt von TU Prints, E-Publishing-Service der Technischen Universitaet Darmstadt <http://tuprints.ulb.tu-darmstadt.de>
tuprints@ulb.tu-darmstadt.de



Die Veroeffentlichung steht unter folgender Creative Commons Lizenz:

Namensnennung - Keine kommerzielle Nutzung - Keine Bearbeitung

4.0 Deutschland

<https://creativecommons.org/licenses/by-nc-nd/4.0/>

Erklärung

Hiermit erkläre ich, dass ich die vorliegende Arbeit, abgesehen von den in ihr ausdrücklich genannten Hilfen, selbständig verfasst habe

Darmstadt, den 27.03.2017

Abstract

Active flow control in laminar boundary layers can reduce wall friction on a wing, if laminar-turbulent transition is delayed. In this thesis, (re-)active flow control for active cancellation of Tollmien-Schlichting (TS) waves in a two-dimensional laminar boundary layer is investigated. The TS-waves that initiate the transition to turbulence are attenuated with a DBD plasma actuator by superposition.

Active wave cancelation requires the use of control algorithms and their stability is influenced by variable inflow conditions. Model-based (Linear-Quadratic-Gaussian) and adaptive control algorithms (filtered-x-LMS) are investigated under realistic (varying) inflow conditions in wind-tunnel and in-flight experiments. The further developed delayed-x-LMS algorithm allows a stable and robust controller operation for active wave cancelation in flight. All experimental results are validated by direct numerical simulations and linear stability theory.

Furthermore, the challenges for the application of DBD plasma actuator arrays to delay natural transition are pointed out. The simplification of transfer paths for reducing the required computational power is discussed.

Kurzfassung

Aktive Strömungskontrolle in der laminaren Strömungsgrenzschicht kann die Wandreibung am Tragflügel durch Verzögerung der laminar-turbulenten Transition verringern. In dieser Arbeit wird die (re-)aktive Strömungskontrolle zur Dämpfung von Tollmien-Schlichting (TS) Wellen in einer zweidimensionalen laminaren Grenzschicht untersucht. Die TS-Wellen, welche die Transition einleiten, werden nach dem Superpositionsprinzip mit DBD Plasmaaktuatoren ausgelöscht.

Die aktive Wellendämpfung setzt den Einsatz von Regelalgorithmen voraus, deren Stabilität von variablen Anströmbedingungen beeinflusst wird. Der Einsatz modellbasierter (Linear-Quadratic-Gaussian) und adaptiver Regelalgorithmen (filtered-x-LMS) wird in Windkanal- und Flugexperimenten unter realistischen (variablen) Anströmbedingungen untersucht. Die Weiterentwicklung des delayed-x-LMS Algorithmus ermöglicht einen stabilen sowie robusten Betrieb des Reglers für die aktive Wellendämpfung im Flug. Die gewonnenen Ergebnisse werden durch direkte numerische Simulationen sowie lineare Stabilitätstheorie validiert.

Die Herausforderungen für den Einsatz von DBD Plasmaaktor-Arrays zur Verzögerung der natürlichen Transition werden in der Arbeit aufgezeigt. Für die Reduzierung der benötigten Rechenleistung wird die Vereinfachung von Übertragungspfaden diskutiert.

Acknowledgments

First of all I would like to thank Prof. Cameron Tropea and Prof. Sven Grundmann for giving me the opportunity to pursue my research at the Institute for Fluid Dynamics and Aerodynamics (SLA) of the Technische Universität Darmstadt. The unique facilities with the motorized glider contributed a lot to this thesis. Although he moved to Rostock, Sven was still involved in my work. Thank you for your support and for refereeing my thesis!

The financial support from the German Research Foundation (DFG) under grant GR 3524/4-1 is gratefully acknowledged. My project gave me the opportunity to meet many people at places all around the world, which inspired me a lot. In particular I want to mention the colleagues of the Linné FLOW Centre at KTH Stockholm. I would like to thank Prof. Dan Henningson for a fruitful collaboration over the years and for refereeing this thesis. I enjoyed the joint experiments with Nicolò Fabbiane. This collaboration is a good example how simulation and experiment can complement each other.

Without the help of students my research would not have been so successful. The long list underlines the support I experienced: Alexander Burkl, Marco Schleyer, Charlie Guan, Felix Fischer, Jonathan Burmester, Nemanja Babić, Askar Kazbekov, Paul Schnabel, Tobias Hofmann, Maximilian Kuhnenn, Timotheus Nemitz, Adrian Filius, Yasin Turkac, Daniel Markus, Ariane Auernhammer, Zacharias Kraus, Max Luh and Yannick Fischer. I also want to thank Jens Rohlfing from Fraunhofer LBF in Darmstadt, who taught me much about control theory when we supervised two of my Master's students.

I was able to conduct save in-flight experiments because Martin Stenger maintained the aircraft. Many thanks also to the pilots: Andreas Reeh, Markus Jenkner and Tobias Hofmann. In addition I want to thank all former and current colleagues, also the workshop, for a great time at the campus in Griesheim. Many thanks to Ulrike Cordes, Timo Nemitz, Daniel Freudenhammer and Max Kuhnenn for proof reading this thesis.

Finally, I would like to thank my family and friends for the support during my time in Darmstadt and abroad.

Thank you.

Bernhard

Contents

Abstract	iii
1. Introduction	1
1.1. Motivation	1
1.2. Boundary-Layer Flow Control with Plasma Actuators	4
1.3. Objectives and Outline of the Thesis	6
2. Background and Theoretical Considerations	11
2.1. Hydrodynamic Stability	11
2.1.1. Governing Fluid Mechanic Equations	11
2.1.2. Boundary-Layer Theory	12
2.1.3. Linear Stability Theory	14
2.1.4. Development and Properties of Tollmien-Schlichting waves	16
2.2. Control Theory	20
2.2.1. Spectral Density and Coherence	20
2.2.2. Digital Filters and the Least-Mean-Squares Algorithm .	21
2.2.3. Filtered-x-LMS Algorithm	23
2.2.4. Delayed-x-LMS Algorithm	24
2.2.5. Multichannel Adaptive Control Algorithms	29
3. Methods and Facilities	33
3.1. Dielectric Barrier Discharge Plasma Actuator	33
3.2. Flat Plate Setup for 2D Investigations	37
3.3. Particle Image Velocimetry for Boundary-Layer Measurements	40
3.4. Flat Plate Setup for 3D Investigations	43
3.5. Experimental Flight Setup	46
3.5.1. Laminar Wing Glove	47
3.5.2. In-Flight Testing Procedure	50
3.6. Implementation and Execution of the Control Algorithms . . .	52

4. Phase-Locked Particle Image Velocimetry Measurements	55
4.1. Base Flow on the Flat Plate	57
4.2. The Effect of Steady Plasma Actuator Forcing on the Base Flow	59
4.3. Artificially Generated Tollmien-Schlichting Waves	61
4.3.1. Influences on the Tollmien-Schlichting Wave Generation	61
4.3.2. Characterisation of the Tollmien-Schlichting Waves . . .	64
4.4. The Effect of Steady Plasma Actuator Forcing on Tollmien-Schlichting Waves	66
4.5. Counter-waves Generated by the Plasma Actuator	68
4.6. Active Cancellation of Tollmien-Schlichting Waves	70
4.7. Conclusions	74
5. Stability Impacts on Static and Adaptive Control Algorithms	75
5.1. Base Flow on the Flat Plate	75
5.1.1. Boundary-Layer Receptivity	77
5.1.2. A Direct Numerical Simulation Model of the Flow . . .	80
5.2. Active Wave Cancellation with Static and Adaptive Control Algorithms	83
5.3. Influences on the Controller Stability	86
5.3.1. Compensators under Varying Inflow Conditions	86
5.3.2. Phase-Angle Dependent Stability of the fxLMS Algorithm	90
5.4. Adaptive Secondary Path for the fxLMS Algorithm	94
5.4.1. Scaling and Stretching of the Secondary Path	94
5.4.2. Controller Stability with Adaptive Secondary Path . . .	95
5.4.3. Embedded Sensors for Flow-state Identification	96
5.5. Conclusions	99
6. In-Flight Experiments under Varying Inflow Conditions	101
6.1. Base Flow around the Wing Glove	101
6.1.1. A Direct Numerical Simulation Model of the Flow . . .	102
6.1.2. Boundary-layer Stability of the Base Flow	106
6.2. Active Wave Cancellation with dxLMS and fxLMS Controller .	109
6.2.1. Varying Inflow Conditions	113
6.2.2. dxLMS Controller Stability and Model Adaptation . . .	115
6.3. Conclusions	120

7. Potential of Plasma Actuator Arrays for Transition Delay	123
7.1. Vortex Identification by IR Thermography	123
7.2. Coupling of Tansfer Paths in the Plasma Actuator Array Setup	126
7.2.1. Capacitive Coupling in the High-voltage Generator . . .	126
7.2.2. Capacitive Coupling of the Plasma Actuator Array . . .	128
7.2.3. Coupling of the Secondary Paths	130
7.2.4. Potential for Future Applications	130
7.3. Transmission Behavior of the Generated Waves.	132
7.3.1. Counter-waves Generated by the Plasma Actuator . . .	133
7.3.2. Waves Generated by the Disturbance Source	134
7.4. Conclusions	134
8. Conclusions and Outlook	137
Nomenclature	143
Bibliography	153
A. Additional PIV Results	165
B. Outlook for Future MIMO Controller Operation	167
B.1. Simplifications for the Secondary Paths	167
B.2. Simplifications for the Control Kernel	168

1. Introduction

1.1. Motivation

Since the first systematic investigations of Lilienthal in the 1890s, researchers have gained increasing insight into the fundamentals of aerodynamics and flight mechanics. Nowadays transport aircraft are reliable, tickets are affordable for everybody, but increasing global air traffic and environmental considerations demand more efficient aircraft designs. Although transport aircraft have looked similar for the past 60 years, performance, fuel efficiency and noise emissions have improved significantly. This is not only due to new materials and more efficient engines, but also due to improved aerodynamics.

Computers control and optimize processes during flight by calculating the most efficient route or even allow accurate automatic landings. Nevertheless, the flow around the aircraft during flight is passively influenced by the airfoil shape and not actively controlled. For example, passive vortex generators on the wing surface create additional lift during take-off/landing and cause a minimum of drag increase at one design point, but their advantage is offset with additional drag during off-design conditions. This classic passive flow control method is limited and flow control strategies will develop from purely passive methods (wing shape, passive vortex generators) to active methods in the future (Gad-el-Hak, M. (2007)). Active flow control, where energy is added to the flow by actuators, can be adapted dependent on the (varying) inflow conditions or even switched off.

The complex demands on the reliability of modern transport aircraft lead to a conservative design process, but future aircraft must be more efficient in terms of fuel consumption. One possible contribution to achieve this goal is the reduction of skin friction drag by laminar wing technology. The skin friction in a laminar boundary layer (BL) is lower compared to a turbulent BL. Therefore, the goal is to prevent an early transition from a laminar to a turbulent BL state. Depending on Reynolds number Re , surface rough-

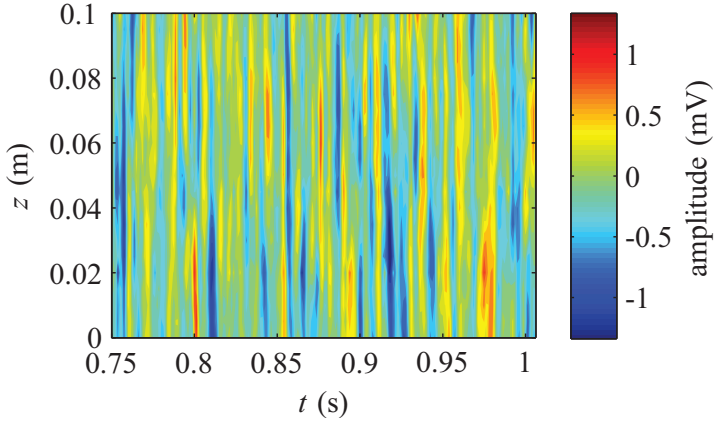


Figure 1.1.: The measurement signals of an uncalibrated hot-film array show natural TS-wave packets on the pressure side of the wing glove in spanwise (z) direction as a function of time t , Reeh (2014).

ness, inflow turbulence and wing shape, the mechanisms causing a transition to turbulence differ. In this thesis the Tollmien-Schlichting (TS) wave dominated transition is investigated: velocity fluctuations in the BL, which travel downstream and grow in amplitude, become unstable and finally lead to a transition to turbulence (Kachanov (1994)). The hot-film measurements in Fig. 1.1 show the temporal evolution of naturally occurring TS-waves on the pressure side of a natural laminar flow (NLF) wing. The low amplification scenario on the pressure side of the wing causes a viscous instability (Schlichting and Gersten (2000)) and the waves occur in spanwise (3D) wave packages in a narrow frequency band, cf. section 2.1.3. Phase speed and amplitude of the waves vary with Re and angle of attack α , leading to a change of the transition location.

NLF wings were developed and successfully applied on gliders for decades. In combination with smooth surfaces (glass/carbon fiber construction) and with no engine induced noise or vibrations, the laminar BL can cover up to 90% of the pressure side of a wing Boermans (2006). Transport aircraft fly at higher Re and additional sources of noise or surface roughness influence the BL development. Therefore, additional active flow control techniques are required (Braslow (1999)) to enable laminar flow over a long percentage of chord. The

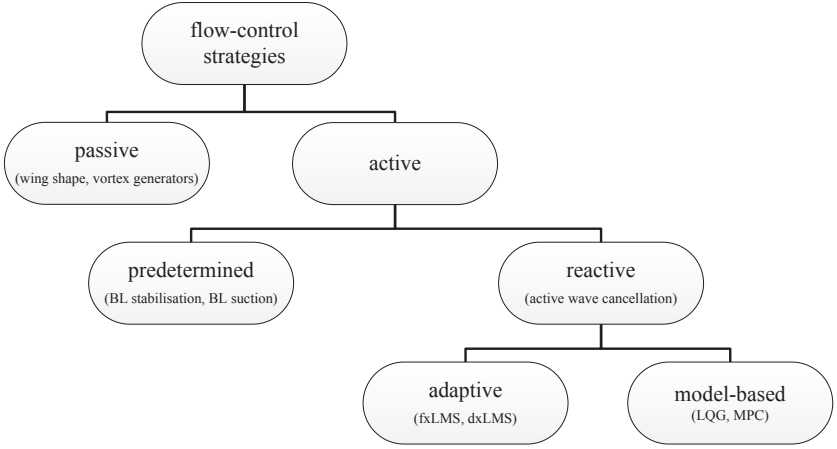


Figure 1.2.: Classification of boundary layer flow-control strategies, after Gad-el-Hak, M. (2007).

hybrid laminar flow control (HLFC) wing concept combines the well-known approach of passive flow control (NLF wing shape) with active control techniques. Boeing introduced a suction system on the leading edge of the vertical stabilizer of the Boeing 787-9. The system is passive because the required pressure difference for the suction system is not realized by a pump but with a pressure difference that occurs at the aircraft body (Parikh (2011)). The predetermined active flow control strategies, like BL suction, are relatively simple in terms of control complexity and active systems could be applied on a commercial aircraft in the near future (Schrauf (2004)).

The scope of this thesis is reactive flow control (Fig. 1.2). It is one step further and promising in terms of energy efficiency, because the actuator only acts on distinct perturbations in the flow instead of changing the mean flow. In this thesis control strategies for a robust control of these TS-waves are developed, with the goal to delay transition under varying inflow conditions. The Dielectric-Barrier-Discharge (DBD) plasma actuator, which has been used for the investigations presented in this thesis, and related flow control strategies are introduced in the following.

1.2. Boundary-Layer Flow Control with Plasma Actuators

The DBD plasma actuator (PA) as a flow control device has emerged since Roth et al. (1998, 2000) published first investigations on BL flow control with this device. Encouraged by these investigations, an increasing number of researchers started to work on two major topics:

1. Working principles and characterisation, including numerical models.
2. Possible applications for the promising new flow control device.

A classification of the PA as a flow control device among all other classical actuators is given in an extensive review by Cattafesta and Sheplak (2011).

Until now, the PA as a flow control device has only been used in the scientific environment. During the last decade, many developments of the actuator, like different electrode designs and operation modes, have been investigated and research is ongoing. The development and characterisation of plasma actuators as well as different applications were summarized in numerous review papers (Benard and Moreau (2014); Corke et al. (2010); Kotsonis (2015); Kriegseis et al. (2016); Moreau (2007); Wang et al. (2013)).

Initially, the application of the PA was dominated by experiments on circulation (separation) control. Limited momentum production and the poor fluid-dynamic efficiency of the PA suggest that the focus be placed on boundary-layer control approaches. The flow velocity in the BL is lower than in the free stream and therefore less momentum for a successful flow control is necessary. In the following, flow control in the laminar BL with PAs is discussed in more detail. Only certain aspects are discussed here, for a more detailed review the reader is referred to Kriegseis et al. (2016).

Besides the vortex generation with PAs for control of cross flow transition (Chernyshev et al. (2016); Dörr and Kloker (2017); Wicks et al. (2015)), the PA has mainly been applied for forcing in streamwise direction in order to stabilise the BL by changing the mean flow properties (Duchmann et al. (2013); Grundmann and Tropea (2007); Jousot et al. (2013)). BL stabilisation is relatively easy to implement and no additional control circuits are necessary. Experiments on boundary-layer stabilisation with DBD plasma actuators in

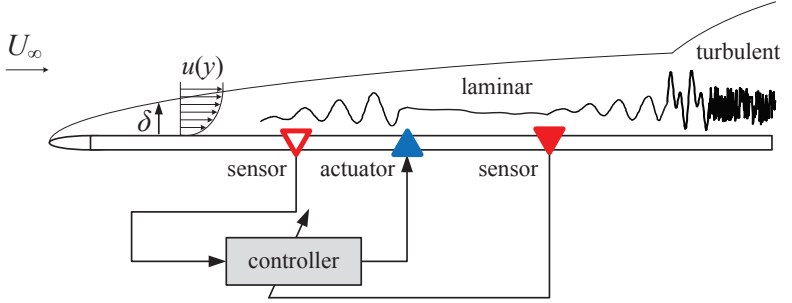


Figure 1.3.: Transition scenario of a flat-plate boundary layer with applied active wave cancellation. The TS-wave is sensed by a sensor, travels downstream and is cancelled out by superposition with the actuator.

flight have been conducted by Duchmann et al. (2014) and hot-wire measurements showed a delay of laminar-turbulent transition by 3% chord. For this flight setup an infra-red (IR) thermography based transition detection system has been developed (Simon et al. (2016c)) and the impact of the steady PA forcing on the transition was measured with a high spatial resolution. It was shown that the PA has an uniform effect on the transition location in spanwise direction, but the overall efficiency does not exceed $\eta_{\text{eff}} = 5\%$, where $\eta_{\text{eff}} = 1$ is the break even in terms of energy consumption/savings.

Active wave cancellation (AWC) of TS-waves is a promising alternative to the BL stabilisation, because the mean velocity profile of the boundary layer is not significantly modified. As sketched in Fig. 1.3, the downstream moving TS-waves that initiate the transition process are measured by a sensor and cancelled out with an actuator by superposition. Attenuation of the TS-wave amplitude then leads to a delayed transition to turbulence further downstream. The TS-waves have an amplitude of about 1% of the free-stream velocity; hence their cancellation requires less energy compared to the boundary-layer stabilisation. Motivated by early work on AWC (Liepmann and Nosenchuck (1982); Milling (1981); Thomas (1983)), Grundmann and Tropea (2008) used a single PA to cancel out artificially generated TS-waves in a laminar BL. Other researchers conducted numerical investigations on AWC (Dadfar et al. (2014, 2015); Kotsonis et al. (2013)). Experiments on attenuation of single frequency 2D TS-waves by Kurz et al. (2014) showed

the first application of the PA for AWC in flight. The concept of amplitude attenuation by superposition is widely spread in other disciplines. Active noise cancellation (Hansen (2002)) is the most prominent example and already available in consumer goods like headphones.

Arrays of actuators and sensors are required to account for the three-dimensional character of naturally occurring TS-waves, cf. Fig. 1.1. Recently, the successful application of arrays of actuators in a multi-channel system was reported in literature (Goldin et al. (2013); Opfer (2002); Pätzold (2013); Peltzer et al. (2009)). Numerical simulations of a multi-channel system with an array of PAs by Fabbiane et al. (2017) showed a delay of transition of a flat plate flow ($Re_1 = 1000$, $U_\infty = 60 \text{ m/s}$).

In literature, different control algorithm strategies for active flow control are reported, as reviewed by Brunton and Noack (2015). Numerical investigations mainly focus on model-based control algorithms like the LQG (Bagheri and Henningson (2011); Fabbiane et al. (2014); Semeraro et al. (2013)), which are based on DNS simulations and a model reduction of the system (Bewley and Liu (1998); Moore (1981)). The experimental community mostly uses adaptive control algorithms such as the filtered-x-LMS (fxLMS) algorithm (Kotsonis et al. (2015); Kurz et al. (2014); Sturzebecher and Nitsche (2003)). Adaptive control algorithms can adapt to changes in the transfer paths of the controlled system, which can be caused by varying inflow conditions during controller operation.

Technical applications will have to cope with varying inflow conditions and should work reliably over a certain range of operation conditions. The work presented in this thesis investigates and evaluates the robustness of different control strategies under such conditions.

1.3. Objectives and Outline of the Thesis

Boundary-layer flow control with DBD plasma actuators has been investigated by researchers worldwide and at the Institute for Fluid Mechanics and Aerodynamics at TU Darmstadt. The PA has been operated continuously (steady forcing) for boundary-layer stabilisation and with a modulated operating voltage (unsteady forcing) for active wave cancellation of Tollmien-Schlichting waves. Both operation modes can successfully delay transition to

turbulence but need to be further analyzed. This thesis is devoted to the investigation of open questions that arise from previous experiments and to the investigation of flow control under varying inflow conditions. In collaboration with the Linné FLOW Centre of the KTH Stockholm, these questions were investigated both numerically and experimentally. Two publications about the joint wind-tunnel experiments (Fabbiane et al. (2015)) and in-flight experiments (Simon et al. (2016a)) conducted at TU Darmstadt and supported with direct numerical simulation (DNS) by KTH, have been published, and the content of this thesis is partly based on these results.

The main questions addressed in this thesis are stated below and outlined in more detail in the following.

- Active wave cancellation: How exactly do the counter-waves, generated by the PA, interact with the TS-wave disturbances in the boundary layer? (Chapter 4)
- Are model-based control algorithms (e.g. LQG) or adaptive algorithms (e.g. fxLMS) better suited for active wave cancellation in terms of performance and controller stability? (Chapter 5)
- What are the implications for the controller stability under more realistic, varying inflow conditions in flight? (Chapter 6)
- How can naturally occurring TS-wave dominated transition be controlled with an array of spanwise arranged plasma actuators? What are the challenges of applying AWC to this transition scenario? (Chapter 7)

In **Chapter 2** of this thesis the physical background and theoretical considerations are discussed. Boundary-layer theory and linear stability theory (LST) are introduced. Another main issue of this chapter is the control theory of the algorithms used for active cancellation of TS-waves.

Chapter 3 gives an overview of the experimental methods. The working principle and design of DBD plasma actuators is discussed first, followed by the descriptions of the flat plate setup used for fundamental wind-tunnel experiments on the controller stability. The research aircraft and the laminar wing glove, prepared for in-flight experiments on AWC, are introduced and the implementation and execution of the required control algorithms is presented.

The PIV measurements presented in **Chapter 4** show the cancellation process of the TS-waves in a flat plate boundary layer. Phase-locked PIV measurements are performed with artificially generated single-frequency TS-waves with a 2D even wavefront and the results are compared to LST.

The AWC of broad-band TS-wave disturbances requires a detailed knowledge about the transmission behavior of the boundary layer. Theoretically, this transmission behavior can be modelled numerically with DNS computations and transferred to an experiment. This model-based control technique is applied with a LQG control algorithm and compared to an adaptive fxLMS control algorithm in terms of controller performance for varying inflow conditions. The experimental results obtained with the single-input-single-output (SISO) system with one 2D actuator are discussed in **Chapter 5** and were published in Fabbiane et al. (2015). Based on these investigations, the controller stability of the fxLMS algorithm and its dependency on the secondary path model between PA and error sensor is analyzed. In order to extend the working range of the controller, an adaptive secondary path model is introduced. A calibration of the secondary path model for different wind-tunnel speeds extends the stable operation range of the controller to the whole calibrated domain (Simon et al. (2015)).

The know-how about the controller stability allows the development of a new algorithm with significantly reduced complexity. The delayed-x-LMS (dxLMS) algorithm and its application for in-flight experiments on a glider wing is introduced in **Chapter 6**. The narrowband character of the TS-waves allows a simplification of the secondary path to a simple delay. The online measurement of the TS-wave group speed by correlation of two upstream sensor signals is the key to a “black box” system, which makes a system identification prior to the controller operation obsolete. This is an important step towards a stable controller operation under changing inflow conditions in a realistic flight scenario (Simon et al. (2016a)).

Chapter 7 discusses the application of a spanwise PA array, which is necessary to damp TS-waves occurring in a natural transition scenario. The experiments on AWC mentioned above deal with artificially generated 2D TS-waves to reduce the system complexity for controller stability investigations and algorithm development. The 3D scenario with the multiple-input-multiple-output (MIMO) system requires more complex control algorithms and therefore a detailed look on the transmission behavior between all sen-

sors and actuators. Flat plate wind-tunnel experiments are conducted with an array of spanwise aligned PAs. Vortex generation at the edges of the PA electrodes and the effect on the boundary-layer stability are experimentally investigated with IR measurements downstream of the PA array. The design of the PA array shape and minimization of occurring electromagnetic interference between the PAs are crucial for a successful application.

The thesis concludes with final conclusions and an outlook in **Chapter 8**.

2. Background and Theoretical Considerations

Active cancellation of Tollmien-Schlichting waves requires background knowledge of several disciplines. In this chapter, the basic equations for hydrodynamic stability of a boundary-layer flow are discussed in section 2.1. The control theory required for the active wave cancellation is introduced in section 2.2. Both disciplines are closely connected to each other as the transmission behavior in the laminar boundary layer primarily depends on its stability properties and therefore influences the controller stability and control success.

2.1. Hydrodynamic Stability

This section first introduces the governing fluid mechanic equations for the given BL flow problem in section 2.1.1. Important BL parameters are defined in section 2.1.2 and a short introduction to linear stability theory (LST) is presented in section 2.1.3. The resulting properties of the occurring TS-waves and the effects of moderate pressure gradients are discussed in section 2.1.4.

2.1.1. Governing Fluid Mechanic Equations

For sufficiently low Mach numbers, $Ma = U_\infty/a < 0.3$, the flow can be assumed incompressible and (2.1) is valid. U_∞ indicates the free stream velocity while a is the sonic speed (Spurk and Aksel (2006)).

$$\frac{D\rho}{Dt} = \frac{\partial\rho}{\partial t}\vec{u} \cdot \nabla\rho = 0 \quad (2.1)$$

The three velocity components u , v and w are described by the velocity vector \vec{u} and ρ is the density of the fluid. The incompressible continuity equation can be written as

$$\nabla \cdot \vec{u} = 0 \quad (2.2)$$

and the corresponding Navier-Stokes equation without body forces as

$$\rho \left(\frac{\partial \vec{u}}{\partial t} + \vec{u} \cdot \nabla \vec{u} \right) = -\nabla p + \mu \nabla^2 \vec{u}, \quad (2.3)$$

where μ is the dynamic viscosity and p is the pressure. For the flight experiments (Chapter 6), the change in density due to compressible effects is only $\approx 2\%$ and makes the assumption of incompressible flow valid (Reeh (2014)).

Besides the Mach number, the Reynolds number $Re = ul_{\text{ref}}/\nu$ is an important dimensionless number and describes the ratio between inertial forces and viscous forces. It is calculated with a characteristic length scale l_{ref} and the kinematic viscosity $\nu = \eta/\rho$. For the specific problem of a wing (chord length l) surrounded by fluid with the free-stream velocity U_∞ it is defined as $Re_l = U_\infty l/\nu$.

2.1.2. Boundary-Layer Theory

Ludwig Prandtl introduced the concept of the boundary layer in direct vicinity to a body surface, where the fluid is decelerated/accelerated to the velocity of the body surface. In this thin layer the viscous forces dominate the flow behaviour, while inertial forces dominate the flow outside of the BL.

The flow over a flat plate or a straight aircraft wing can be assumed two-dimensional (2D) and the BL starts to develop from the stagnation point. The high aspect ratio of the glider wing (Chapter 6) leads to an almost parallel inflow and a 2D boundary-layer flow problem. The wind-tunnel experiments (Chapters 4, 5, 7) on the flat plate are assumed 2D because the leading edge is perpendicular to the inflow and no significant spanwise pressure gradient is present. Assuming a 2D inflow, moderate pressure gradients and a low turbulence intensity, which is valid for the in-flight and wind-tunnel experiments in this thesis, the laminar-turbulent transition is dominated by TS-waves.

A laminar BL starts to develop from the leading edge and the boundary-layer thickness δ grows in downstream direction, cf. Fig. 2.1. In the laminar

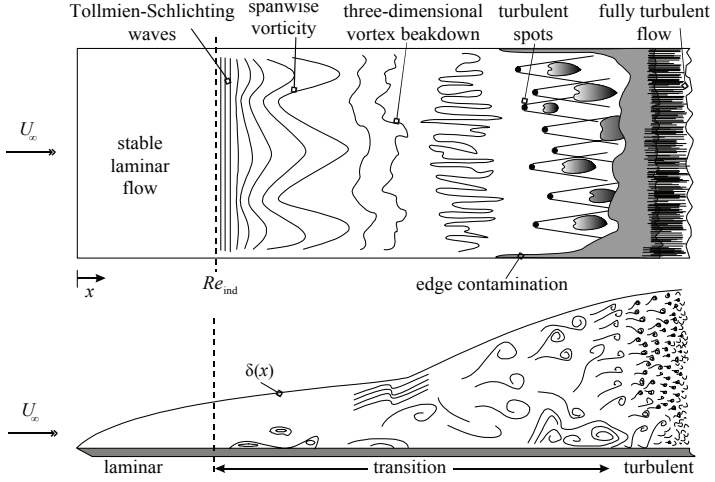


Figure 2.1.: Different states of a flat plate boundary-layer transition, reproduced from White (1974).

BL the fluid elements move tangential to the wall, yielding an undisturbed flow above the wall. Numerous sources can induce perturbations in the laminar BL and may lead to a transition to turbulence. The laminar-turbulent transition on a flat plate or on a NLF airfoil can be divided into different stages, as shown in Fig. 2.1. The TS-wave disturbances grow in amplitude while travelling downstream, break down to vortices and finally lead to a fully turbulent BL flow. The amplification or attenuation of the TS-wave velocity fluctuations, which occur in a narrow frequency band, is determined by the local stability of the BL profile and the receptivity process (Saric et al. (2002)). For the investigations presented in this thesis, the non-linear interactions and the final breakdown to turbulence are not of interest. The flow control action takes place in the first stage of the transition process sketched in Fig. 2.1, the Tollmien-Schlichting wave region.

The shapes of laminar and turbulent BL profiles differ, as the sketch in Fig. 2.2 indicates. The turbulent profile is less sensitive to flow separation and beneficial for cooling processes, because more momentum is transferred from the upper layers to the wall. This leads to a higher skin friction in a

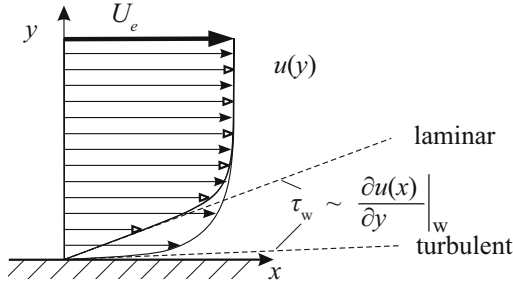


Figure 2.2.: Sketch of a laminar and turbulent boundary-layer profile.

turbulent compared to a laminar BL because the shear stress τ_w depends on the velocity gradient at the wall:

$$\tau_w(x) = \mu \left. \frac{\partial u(x)}{\partial y} \right|_w. \quad (2.4)$$

The BL thickness δ is defined as the wall normal distance y , where $u = 0.99 U_e$ of the boundary-layer edge velocity U_e . The displacement thickness δ_1 (2.5) and the momentum thickness δ_2 (2.6) are important integral boundary-layer parameters.

$$\delta_1(x) = \int_0^\infty \left(1 - \frac{u(x, y)}{U_e(x)} \right) dy \quad (2.5)$$

$$\delta_2(x) = \int_0^\infty \frac{u(x, y)}{U_e(x)} \left(1 - \frac{u(x, y)}{U_e(x)} \right) dy \quad (2.6)$$

The ratio between δ_1 and δ_2 is the shape factor

$$H_{12}(x) = \frac{\delta_1(x)}{\delta_2(x)}. \quad (2.7)$$

For a zero pressure gradient (ZPG) laminar BL, called Blasius BL, the shape factor $H_{12, \text{lam}} = 2.59$. The value for the turbulent case is always lower; for the ZPG BL case $H_{12, \text{turb}} \approx 1.4$.

2.1.3. Linear Stability Theory

Based on the Navier-Stokes equation the linear stability theory (LST) describes the evolution of TS-waves in the linear stage of the transition process

that is independent of the disturbance amplitude. The flow \vec{u} is divided into a steady base flow \vec{U} and superimposed fluctuations \vec{u}' :

$$\vec{u} = \vec{U} + \vec{u}'. \quad (2.8)$$

In accordance to \vec{u} the pressure is divided as follows:

$$p = P + p'. \quad (2.9)$$

Inserting equations (2.8) and (2.9) into (2.2) and (2.3) leads to

$$\nabla \cdot \vec{u}' = 0 \quad (2.10)$$

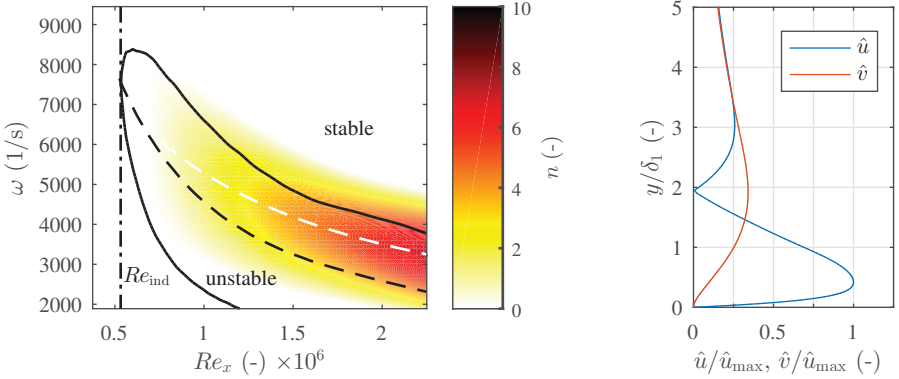
$$\frac{\partial \vec{u}'}{\partial t} + \vec{u}' \cdot \nabla \vec{U} + \vec{U} \cdot \nabla \vec{u}' + \vec{u}' \cdot \nabla \vec{u}' = -\nabla p' + \frac{1}{Re} \Delta \vec{u}'. \quad (2.11)$$

A 2D flow situation ($\vec{U} = U(y)\vec{e}_x$) and small velocity/pressure fluctuations are assumed. The fluctuations can be described by a wave-like approach:

$$\vec{q}'(\vec{x}, t) = \vec{\hat{q}}(y)e^{i(k_x x + k_z z - \omega t)}, \quad (2.12)$$

where ω is the angular frequency and k_x, k_z are the streamwise and spanwise wavenumbers, respectively. The amplitude vector $\vec{\hat{q}} = (\hat{u}, \hat{v}, \hat{w}, \hat{p})^T$ includes the amplitudes of the velocity fluctuations in all three directions as well as the amplitude of the pressure fluctuations. Dependent on whether the spatial or temporal evolution of the wave is considered, the complex or real values of \vec{k} and ω are considered. In the following, the spatial evolution is chosen in order to capture the spatial growth of the TS-wave disturbances. Inserting the wave approach (2.12) into the continuity- and NS-equation finally leads to the Orr-Sommerfeld equation. It describes an eigenvalue problem for \vec{k} and can be solved numerically (Schmid and Henningson (2012)). For the problems presented in this thesis, a BL solver and a LST code developed by Reeh (2014) and modified by Turkac (2016) are used.

For a 2D wavefront ($k_z = 0$) the problem reduces to the imaginary part of k_x , called spatial growth rate $k_{x,i}$. The most prominent eigenvalues are identified by the LST code for all combinations of ω and the local Reynolds number $Re_x = U_\infty x / \nu$ in the chosen grid. The solution of the Orr-Sommerfeld equation for the flow around the wing glove used in this study (Chapter 6) is



(a) Neutral stability curve ($k_{x,i} = 0$, black solid line) and n -factor contours. The dashed black line shows the most amplified frequency ($k_{x,i} = \min$) while the dashed white line indicates the local n -factor maximum N_{\max} .

(b) Amplitude of the TS-wave eigenform of the u and v component.

Figure 2.3.: Linear stability theory solutions.

plotted in a stability diagram in Fig. 2.3(a). The black solid curve indicates the neutral stability curve that connects all eigenvalues $k_{x,i} = 0$. It marks the border, where the TS-waves are neither amplified nor attenuated due to the local stability of the BL profile.

2.1.4. Development and Properties of Tollmien-Schlichting waves

The LST computations only characterize the local behavior of the BL, because $\tilde{q}(y)$ is only a function of the wall-normal coordinate y . Going from left to right in Fig. 2.3(a) (downstream), the disturbances are first attenuated ($k_{x,i} > 0$) for all frequencies ω ; the BL is stable. Downstream of the indifference Reynolds number Re_{ind} , when the neutral stability curve ($k_{x,i} = 0$) is crossed, a narrow band of disturbance frequencies is amplified ($k_{x,i} < 0$). All values of $k_{x,i}$ inside the neutral stability curve are negative, the TS-waves are unstable, while all other values are positive. The most amplified frequency at each Re_x inside the stability curve is marked with a dashed black line ($k_{x,i} = \min$). According to Schlichting and Gersten (2000) the point at Re_{ind}

is called indifference point, yet denoted critical Reynolds number (Re_{crit}) in many other text books. In this thesis the critical point is the location where the transition to turbulence is completed.

The n-Factor

The spatial evolution of the TS-wave amplitude can be determined with the n -factor (2.13). It is calculated by integrating the local amplification rate $k_{x,i}$ in streamwise direction. The left handed side of the neutral stability curve, which defines the lower integration border, is called branch I, while the right handed side is called branch II. Starting integration from branch I for each individual frequency ω at $x_I(\omega)$ leads to

$$n(x, \omega) = \int_{x_I(\omega)}^x -k_{x,i}(x, \omega) dx = \ln \left(\frac{\hat{q}(\omega)}{\hat{q}_I(\omega)} \right). \quad (2.13)$$

It describes the exponential growth of the disturbance \hat{q} with a frequency ω from the indifference point on downstream. The envelope of $n(x, \omega)$ for all ω is the local maximum $N_{\text{max}}(x)$. The solution of the calculation according to (2.13) is shown in Fig. 2.3(a) as a contour plot, whereas N_{max} is indicated with a white dashed line. The TS-waves are attenuated from branch II onwards, therefore n first increases and then decreases. Assuming a low inflow turbulence intensity $Tu < 1\%$, the empirical n -factor method allows to predict the location of transition (van Ingen (2008)). Experiments showed that transition happens, if $N_{\text{max}} \approx 9$ is reached, but lower and higher values are possible, depending on the receptivity process.

The TS-wave disturbances are velocity fluctuations that mainly occur inside the BL, but also have an oscillating part above ($y > \delta$). Figure 2.3(b) exemplarily shows the amplitude of the velocity fluctuations \hat{u} in streamwise direction. Characteristic points are the global maximum at $\frac{y}{\delta_1} \approx 0.5$ and the zero crossing at $\frac{y}{\delta_1} \approx 2$. The wall-normal component of the TS-wave v' is about 60% lower in amplitude compared to u' (Fig. 2.3(b)), but both are coupled. In the discussion of the following chapters only the streamwise component u' is considered as it is more meaningful and mostly used in literature.

TS-wave Properties

The boundary layer is a convectively unstable system, therefore the waves are allowed to grow downstream with a constant spanwise wavenumber k_z and angular frequency ω . The real part of the streamwise wavenumber $k_{x,r}$ allows to compute the phase speed c_ω as well as the wavelength λ_x of the TS-wave in streamwise direction:

$$c_\omega = \frac{k_{x,r}}{\omega} \quad (2.14)$$

$$\lambda_x = \frac{2\pi}{k_{x,r}}. \quad (2.15)$$

Natural TS-wave disturbances always occur as a superposition of waves in a narrow frequency band, cf. Fig 2.3(a). The propagation speed of the superimposed waves is the group speed c_g that is defined as the derivative of ω with respect to the modulus of the wavenumber $|\vec{k}| = k$ (Boiko et al. (2002)):

$$c_g = \frac{\partial \omega}{\partial k} = c_\omega + k \frac{\partial c_\omega}{\partial k}. \quad (2.16)$$

Even for a 2D inflow situation the naturally developing TS-waves occur in wave packets with a 3D character, cf. Fig. 1.1. Their spatial wavelength in spanwise direction λ_z can be calculated accordingly to λ_x (2.15). The propagation angle Θ of a 3D disturbance is defined as

$$\Theta = \arctan \left(\frac{k_z}{k_{x,r}} \right), \quad (2.17)$$

where k_z is the spanwise wavenumber. The spatial resolution of sensors determine the resolvable wavenumbers in streamwise as well as in spanwise direction, as indicated in (2.18) for the spanwise case. K is the number of sensors in spanwise direction and Δz the distance between two sensors.

$$k_{z,\min} = \frac{2\pi}{\Delta z(K-1)} \quad \text{or} \quad \lambda_{z,\min} = \Delta z(K-1) \quad (2.18)$$

The largest wavenumber, which can be detected by two sensors is

$$k_{z,\max} = \frac{\pi}{\Delta z} \quad \text{or} \quad \lambda_z = 2\Delta z, \quad (2.19)$$

according to the Nyquist-Shannon theorem.

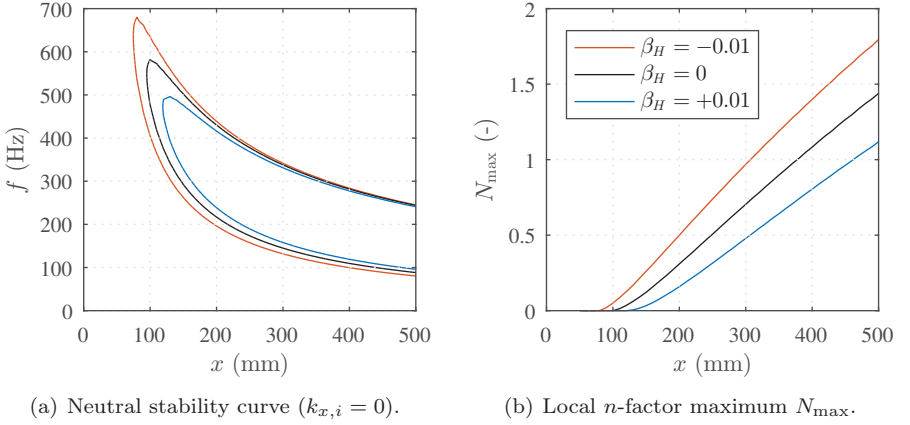


Figure 2.4.: Neutral stability curve and N_{\max} for a Falkner-Skan BL solution with pressure gradient for $U_e = 15$ m/s, a kinematic viscosity of $\nu = 14.29 \cdot 10^{-6}$ m²/s and three different Hartree parameters β_H .

Pressure Gradient and Boundary-Layer Stability

The n -factor method is valid for low disturbance inflow conditions and a transition dominated by TS-wave instabilities. The moderate pressure gradients on the flat plate (section 3.2) and also on the NLF airfoil (section 3.5) fulfill this assumption. The effect of a pressure gradient on the BL stability is shown for a Falkner-Skan BL with three different Hartree parameters β_H (Schlichting and Gersten (2000)). The Falkner-Skan solution for $\beta_H = 0$ corresponds to the Blasius solution, whereas $\beta_H < 0$ stands for an adverse (positive) pressure gradient and $\beta_H > 0$ represents a favourable (negative) pressure gradient. The term favourable already indicates that it is preferred because transition is delayed and the risk of BL separation is lower. The neutral stability curves for three different Hartree parameters are shown in Fig. 2.4(a). Compared to Fig. 2.3(a), the axis labels are changed to f (Hz) and x (mm), which is a common format for comparison with experimental results. The favourable pressure gradient ($\beta_H = 0.01$) moves the neutral stability curve further downstream, which indicates a more stable BL. An adverse pressure gradient ($\beta_H = -0.01$) moves it upstream and increases the local n -factor maximum N_{\max} as shown in Fig. 2.4(b).

2.2. Control Theory

In the following, the control theory is introduced, starting with parameters, which describe the behaviour of a transmission path. Adaptive digital filters and the basic least means squares (LMS) algorithm are defined, followed by the introduction of the adaptive fxLMS and dxLMS algorithms. At the end of this section, multichannel control algorithms are described. Detailed information about the model-based optimal linear-quadratic-gaussian (LQG) algorithm, which is popular for numerical investigations and has been used for the experiments presented in Chapter 5, can be found in review article by Fabbiane et al. (2014) or Schmid and Sipp (2016).

2.2.1. Spectral Density and Coherence

The spectral transmission behaviour that relates a control signal $x(t)$ and a system response $y(t)$ can be expressed with the spectral density of the time signals. The power-spectral density (PSD) S_{xx} and the cross-spectral density (CSD) S_{xy} are defined as follows:

$$S_{xx}(\omega) = \lim_{T \rightarrow \infty} \frac{1}{\sqrt{2T}} (X_T^*(\omega) X_T(\omega)), \quad (2.20)$$

$$S_{xy}(\omega) = \lim_{T \rightarrow \infty} \frac{1}{\sqrt{2T}} (X_T^*(\omega) Y_T(\omega)). \quad (2.21)$$

Where $X_T(\omega)$ is the Fourier transform of the time signal $x(t)$ in an time interval T and $X_T^*(\omega) = X_T(-\omega)$. The power-spectral density S_{xx} is a measure for the power of a signal and has the unit energy per frequency (width), whereas the cross-spectral density S_{xy} is the Fourier transform of the cross-correlation function. Power- and cross-spectral density are often given in the logarithmic decibel (dB) scale, while the conversion from volt (V) is defined as:

$$S_{xx}(\text{dB}) = 10 \log_{10}(S_{xx}(\text{V})). \quad (2.22)$$

Based on these two quantities, the coherence $\gamma_{xy}^2(\omega)$ of two signals $x(t)$ and $y(t)$ can be calculated according to (2.23). It describes the linear dependency of the two signals and reaches from $\gamma_{xy}^2 = 0$ (no linear dependence) to $\gamma_{xy}^2 = 1$ (linear dependence). The control laws described later are based on the linear dependency assumption, therefore γ_{xy}^2 is an important measure for the

controllability of a system.

$$\gamma_{xy}^2(\omega) = \frac{|S_{xy}(\omega)|^2}{S_{xx}(\omega)S_{yy}(\omega)} \quad (2.23)$$

The transmission behavior in the frequency domain $\hat{H}_{xy}(\omega)$ between x and y can be calculated according to (2.24). It is also called unconstrained or two-sided Wiener filter (Elliott (2000)). $\hat{H}_{xy}(\omega)$ fully describes the behaviour between control signal and system response but is not constrained and therefore it might be impossible to use it in a real-time application.

$$\hat{H}_{xy}(\omega) = \frac{S_{xy}}{S_{xx}} \quad (2.24)$$

2.2.2. Digital Filters and the Least-Mean-Squares Algorithm

Digital filters describe the discrete output signal $y(n)$ as a function of a discrete input signal $x(n)$ sampled with a sample rate f_S at discrete time steps t_n :

$$y(n) = \underbrace{\sum_{g=1}^G a_g y(n-g)}_{\text{recursive part}} + \underbrace{\sum_{i=0}^{I-1} b_i x(n-i)}_{\text{transversal part}}, \quad (2.25)$$

with G feedback coefficients a_g and I feedforward coefficients b_i . Digital filters with a recursive part are often referred to as infinite impulse response (IIR) filters while the filters with only a transversal part are called finite impulse response (FIR) filters (2.26). The filter coefficients of such FIR filters are denoted as w_i . FIR filters are always stable because of the missing recursive part, which implies no negative poles of the transfer functions.

$$c(n) = \sum_{i=0}^{I-1} w_i r(n-i) = \mathbf{w}^T \mathbf{r}(n) \quad (2.26)$$

In the block diagram exemplarily drawn in Fig. 2.5, the filter coefficients w_i are adapted based on a cost function, which is the LMS algorithm (Elliott (2000)). It shows the application of the LMS for a common goal: the

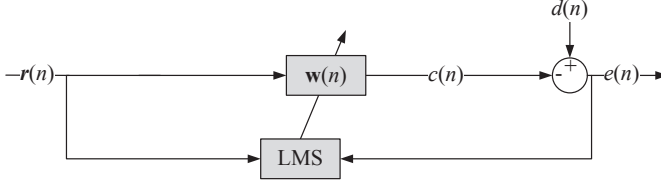


Figure 2.5.: FIR filter with coefficients \mathbf{w} , adapted using the LMS algorithm.

reduction of an error e that is the difference between the filter output c and the (desired) signal d . The vector

$$\mathbf{w} = [w_0 \ w_1 \ \dots \ w_{I-1}]^T \quad (2.27)$$

with a number of I filter coefficients w_i is also called compensator kernel and

$$\mathbf{r}(n) = [r(n), r(n-1) \ \dots \ r(n-I+1)]^T \quad (2.28)$$

is a vector of the last I values of the reference sensor signal.

As discussed above, the unconstrained Wiener filter (2.24) is not suitable for real-time applications due to the required computation power. Therefore, the optimal solution of the filter adaption (Wiener filter) is replaced by the LMS algorithm in many applications. The LMS algorithm adapts the FIR coefficients in the opposite direction to the instantaneous gradient of the mean-square error with respect to the coefficients $\frac{\partial e^2(n)}{\partial \mathbf{w}}$. The resulting update law of the LMS (Elliott (2000)) is written as

$$\mathbf{w}(n+1) = \mathbf{w}(n) + \alpha \mathbf{r}(n)e(n), \quad (2.29)$$

where α is the step size and $\mathbf{w}(n+1)$ the compensator kernel with I filter coefficients that is valid for the next discrete time step. The LMS is an adaptive feed-forward control algorithm because the filter \mathbf{w} is only fed with the upstream sensor signal $r(n)$ but it also uses the feedback path indirectly by using the error sensor signal $e(n)$ for the filter adaption process.

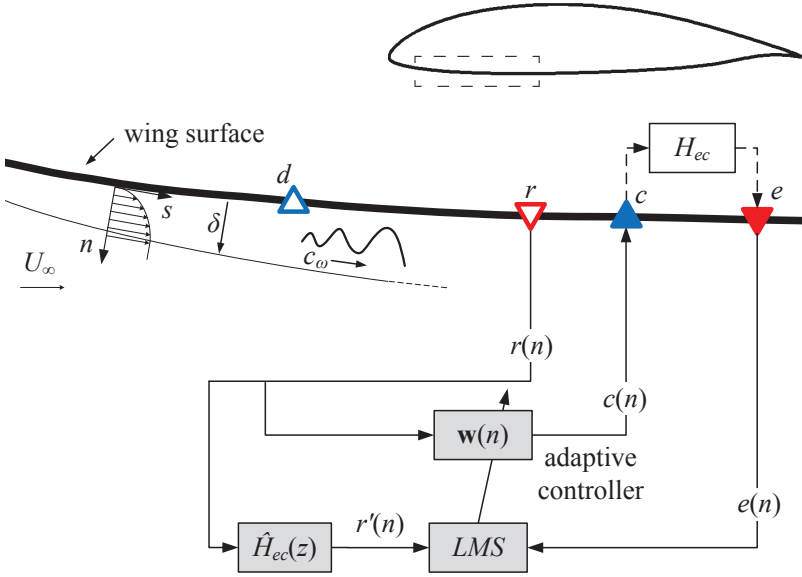


Figure 2.6.: 2D wing setup and extended fxLMS control algorithm sketched below. The red triangles represent reference sensor r and error sensor e . Disturbance source d and plasma actuator c are indicated as blue triangles.

2.2.3. Filtered-x-LMS Algorithm

The flow control system sketched in Fig. 2.6 is a single-input-single-output (SISO) system as it consists of one reference sensor r , an error sensor e and the actuator c .

The transfer function from x to y is defined as H_{yx} (to actuator/sensor y , from actuator/sensor x); therefore H_{er} denotes the primary path (to e , from r) while H_{ec} is the secondary path (to e , from c). Thus, the secondary path describes the transfer function between the plasma actuator c and the error sensor e , while the primary path describes the transmission behavior between reference sensor r and error sensor e . The feedback path H_{rc} (to r , from c) is negligible in the presented flow control system as the measured Tollmien-Schlichting disturbances in the laminar boundary layer only propagate downstream. In order to minimize the error sensor signal $e(n)$, the LMS control algorithm (2.29) adapts the filter \mathbf{w} that describes the behavior of the control

path H_{cr} . The LMS algorithm requires the same position for the actuator c and the error sensor e , otherwise the phase-angle shift due to the secondary path H_{ec} would lead to an unstable controller behavior (Elliott (2000)). The experimental setup does not allow one to place the sensors very close to the plasma actuator due to the high voltage and geometrical concerns. This is often the case also for acoustic or structural vibration problems. Therefore, the physical secondary path H_{ec} is modelled with another FIR filter \hat{H}_{ec} to filter the reference signal $r(n)$ and compensate the phase shift. Note: the hat above \hat{H}_{ec} indicates that it is a model of the physical path H_{ec} , which describes the behavior of the flow. An example for a filter \hat{H}_{ec} is presented in Fig. 2.7(b), which shows the convective behavior of the transmission path for TS-wave disturbances travelling downstream. The graphs on the left in Fig. 2.7 show the corresponding Bode diagram of the FIR filter.

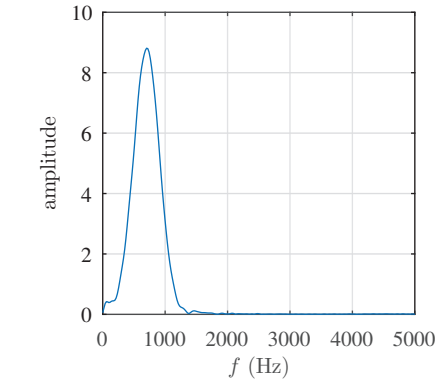
The filtered sensor signal $r'(n)$ is fed into the LMS algorithm as shown in Fig. 2.6 and the algorithm is now called filtered-x-LMS or fxLMS. Its update law is defined as follows:

$$\mathbf{w}(n+1) = \mathbf{w}(n) + \alpha \mathbf{r}'(n) e(n). \quad (2.30)$$

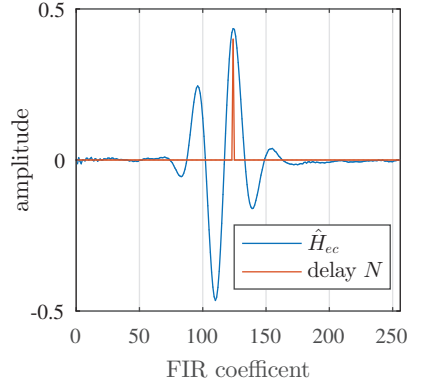
The fxLMS algorithm shows a robust controller behavior as long as the phase-angle error between the physical secondary path H_{ec} and the secondary path model \hat{H}_{ec} is in-between $\pm 90^\circ$. This is a well-known boundary for the controller stability (Hansen and Snyder (2012)).

2.2.4. Delayed-x-LMS Algorithm

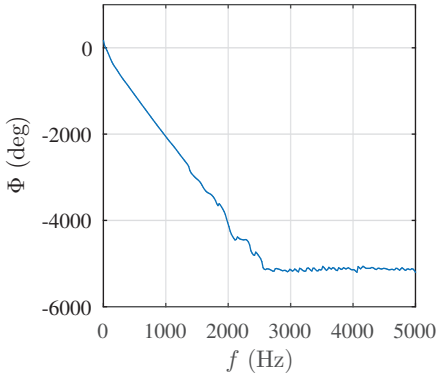
For a narrowband disturbance problem, such as TS-waves in a laminar boundary layer, a delay z^{-N} with N samples might be good enough to approximate a model for the convective behavior of the secondary path. Figure 2.7(b) shows such a model for the secondary path \hat{H}_{ec} as well as the approximation of \hat{H}_{ec} with a delay of $N_P = 124$ samples. The index P indicates a delay corresponding to the global maximum (peak) of \hat{H}_{ec} . Li and Gaster (2006) proposed a related approach for the simplification of a transfer function for active flow control by simplifying the already calculated compensator kernel with a delay. With the delay z^{-N} the LMS algorithm (2.29) can be written



(a) Amplitude response.



(b) FIR filter, for $f_S = 10$ kHz.



(c) Phase response.

Figure 2.7.: Bode diagram and digital FIR filter of a secondary path model \hat{H}_{ec} .

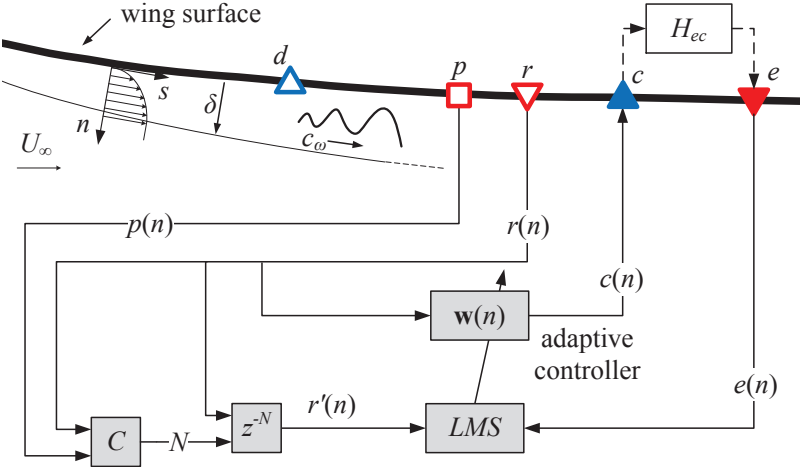


Figure 2.8.: 2D wing setup and dxLMS control algorithm sketched below. The red square represent the upstream sensor p , reference sensor r and error sensor e are shown as red triangles. The disturbance source d and the plasma actuator c are indicated as blue triangles.

as follows and is now called delayed-x-LMS (dxLMS):

$$\begin{aligned}\mathbf{w}(n+1) &= \mathbf{w}(n) + \alpha \mathbf{r}(n) z^{-N} e(n) \\ &= \mathbf{w}(n) + \alpha \mathbf{r}(n-N) e(n).\end{aligned}\tag{2.31}$$

Snyder and Hansen (1990) as well as Kim and Park (1998) applied the dxLMS algorithm for acoustic problems with narrowband noise. The experiments presented in this thesis show its application for laminar BL flow control for the first time.

Figure 2.8 shows the dxLMS controller sketched below the 2D wing setup. Besides the dxLMS algorithm, a second upstream sensor p is introduced that serves as an input signal $p(n)$ for the block C together with the reference sensor signal $r(n)$. Block C is responsible for the identification of the delay N in (2.31). The delay N can be set manually or calculated in real time by online measurements. In the following, the procedure for calculating the delay N is described.

Delay Identification

A TS-wave is travelling downstream and the growth in amplitude is neglected, since it is not relevant for the following analysis. Assuming a group speed c_g (2.16), the cross-correlation of two sensor signals at location x_p and x_r gives the time shift between both sensor signals τ .

$$\tau(\omega) = \int_{x=x_p}^{x_r} \frac{1}{c_g(\omega)} dx. \quad (2.32)$$

A parallel flow and a slowly varying BL properties are considered, therefore the group-speed can be assumed to be constant between the two locations ($x_r - x_p = \Delta x_{pr}$). Equation (2.32) then reduces to

$$\tau(\omega) \approx \tau = \frac{x_r - x_p}{c_g} = \frac{\Delta x_{pr}}{c_g}. \quad (2.33)$$

This translates in a time-discrete delay or lag L between the sensors p and r

$$L = \tau f_S = \frac{\Delta x_{pr}}{c_g} f_S, \quad (2.34)$$

where f_S is the sampling frequency.

Because the digital signal processor executes the algorithm at a rather low frequency $f_S \approx 10$ kHz, the phase-angle resolution $\delta\Phi(f) = \frac{f}{f_S} 360^\circ$ has to be taken into account for the accuracy of the signal lag measurement L . If the assumption of an almost constant average group speed is correct, the signal lag L in samples can be normalized by the distance between the sensors p and r (Δx_{pr}) and a normalized time delay γ is introduced as follows:

$$\gamma = \frac{L}{\Delta x_{pr}} = \frac{N}{\Delta x_{ce}} = \frac{f_S}{c_g}. \quad (2.35)$$

Equation (2.35) indicates that the required delay N for the dxLMS operation can then directly be calculated from a measurement of the signal lag L by

$$N = \gamma \cdot \Delta x_{ce}, \quad (2.36)$$

where N is rounded to the closest integer. This relation leads to a “black box” system that could operate the controller without any knowledge of the laminar BL flow around the wing glove. Chapter 6 discusses the application

of the dxLMS in flight and the advantages in comparison with the well-known fxLMS approach.

The key to this reduction in the complexity of the secondary path is the similarity between the phase response given by the time delay and the actual phase response of the secondary path H_{ec} . The phase-angle shift associated with a time delay reads:

$$\Delta\Phi(f) = - \left(360^\circ \frac{N}{f_S} \right) f, \quad (2.37)$$

where $f = 2\pi\omega$ is an arbitrary frequency. As mentioned before, a similar expression can be derived for the disturbances in the TS-wave band. A downstream propagating wave causes a phase-angle shift $\Delta\Phi$ of the sensor signals between the two different streamwise positions. It can be shown that the derivative of the phase-angle shift $\Delta\Phi$ with respect to the angular frequency ω is equal to minus the previously computed time delay τ :

$$\begin{aligned} \frac{\partial}{\partial\omega}(\Delta\Phi) &= \frac{\partial}{\partial\omega}(-k \Delta x) \\ &= -\frac{\partial k}{\partial\omega} \Delta x = -\frac{\Delta x}{c_g} = -\tau. \end{aligned} \quad (2.38)$$

Hence, by integrating $\frac{\partial}{\partial\omega}(\Delta\Phi)$ in this region, the phase-angle shift (in deg) can be obtained:

$$\Delta\Phi(f) = - \left(360^\circ \frac{\Delta x}{c_g} \right) f_{\text{TS}} + \Delta\Phi_0, \quad (2.39)$$

where $f_{\text{TS}} = 2\pi\omega$ is the frequency of the TS-wave and $\Delta\Phi_0 \in [0^\circ, 360^\circ)$ is the zero-cross phase. By comparing equations (2.37) and (2.39), the possible values of $\Delta\Phi_0$ reduce to 0° , if a positive gain is used in front of the time delay, or 180° , if a negative gain is considered. Hence, once the time delay τ is identified via a measurement of the group speed c_g , the only free parameter for the dxLMS design is the positive/negative gain associated with the time delay.

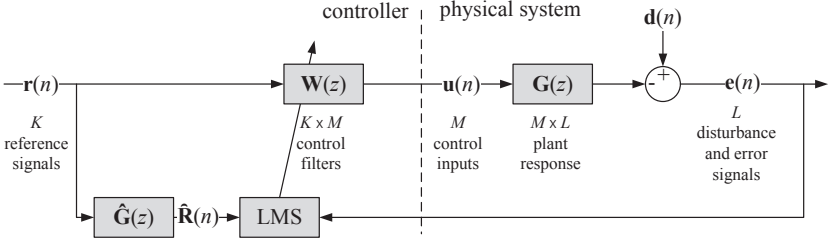


Figure 2.9.: Block diagram of a fxLMS multichannel control system.

2.2.5. Multichannel Adaptive Control Algorithms

In a multiple-input-multiple-output (MIMO) system, a set of K (Table 2.1) reference sensor signals \mathbf{r} is available:

$$\mathbf{r} = [r_1(n) \ \dots \ r_K(n)]^T. \quad (2.40)$$

With a number of L error sensors the vector of error signals is defined as

$$\mathbf{e}(n) = [e_1(n) \ \dots \ e_L(n)]^T. \quad (2.41)$$

A block diagram of a general multichannel feedforward control system with M actuators is shown in Fig. 2.9. The l -th error signal in explicit form is

$$e_l(n) = d_l(n) - \sum_{m=1}^M \sum_{j=0}^{J-1} g_{lmj} u_m(n-j), \quad (2.42)$$

where $d_l(n)$ is the l -th desired signal.

variable	description (number of ...)
I	FIR coefficients, compensator \mathbf{W}
J	FIR coefficients, plant \mathbf{G}
K	reference sensors
L	error sensors
M	actuators
S	disturbance sources

Table 2.1.: Description of MIMO parameters.

The FIR filter g_{lmj} or \mathbf{G}_j describes the response of the plant on the M actuator signals $\mathbf{u}(n) = [u_1(n) \dots u_M(n)]^T$. In matrix form (2.42) can be written as

$$\mathbf{e}(n) = \mathbf{d}(n) - \sum_{j=0}^{J-1} \mathbf{G}_j \mathbf{u}(n-j), \quad (2.43)$$

The control signal $\mathbf{u}(n)$ is calculated with the compensator kernel \mathbf{W} and the reference sensor signals \mathbf{r} :

$$\mathbf{u}(n) = \sum_{i=0}^{I-1} \mathbf{W}_i \mathbf{r}(n-i), \quad (2.44)$$

while the i -th matrix \mathbf{W}_i of $M \times K$ filter coefficients is defined as

$$\mathbf{W}_i = \begin{bmatrix} w_{11i} & w_{12i} & \dots & w_{1Ki} \\ w_{21i} & w_{22i} & & \\ \vdots & & \ddots & \\ w_{M1i} & & & w_{MKi} \end{bmatrix}. \quad (2.45)$$

For a SISO system the Matrix \mathbf{W}_i has only one entry $w_{11i} = w_i$, cf. (2.27). The operation in (2.44) can also be written for each individual control output:

$$u_m(n) = \sum_{k=1}^K \sum_{i=0}^{I-1} w_{mki}(n) x_k(n-i). \quad (2.46)$$

Combining (2.43) and (2.46) finally leads to

$$\mathbf{e}(n) = \mathbf{d}(n) - \sum_{j=0}^{J-1} \sum_{i=0}^{I-1} \mathbf{G}_j \mathbf{W}_i \mathbf{r}(n-i-j). \quad (2.47)$$

The MIMO fxLMS controller also requires a secondary path model $\hat{\mathbf{G}}$ (\hat{H}_{ec} for the SISO system), which describes the transfer path between the M actuators and the L error sensors. Each of the J filter coefficients $\hat{\mathbf{G}}_j$ is a $M \times L$ matrix:

$$\hat{\mathbf{G}}_j = \begin{bmatrix} \hat{g}_{11j} & \hat{g}_{12j} & \dots & \hat{g}_{1Mj} \\ \hat{g}_{21j} & \hat{g}_{22j} & & \\ \vdots & & \ddots & \\ \hat{g}_{L1j} & & & \hat{g}_{LMj} \end{bmatrix}. \quad (2.48)$$

The filtered reference sensor signal $\hat{r}_{lmk}(n)$ is calculated with secondary path model \hat{g}_{lmj}

$$\hat{r}_{lmk}(n) = \sum_{j=0}^{J-1} \hat{g}_{lmj} r_k(n-j). \quad (2.49)$$

Equation (2.49) can also be written in matrix format

$$\hat{\mathbf{R}} = \sum_{j=0}^{J-1} \hat{\mathbf{G}}_j \mathbf{r}(n-j), \quad (2.50)$$

while the result is the following matrix:

$$\hat{\mathbf{R}}(n) = \begin{bmatrix} \hat{\mathbf{r}}_1^T(n) & \hat{\mathbf{r}}_1^T(n-1) & \dots & \hat{\mathbf{r}}_1^T(n-I+1) \\ \hat{\mathbf{r}}_2^T(n) & \hat{\mathbf{r}}_2^T(n-1) & & \\ \vdots & & \ddots & \\ \hat{\mathbf{r}}_L^T(n) & & & \hat{\mathbf{r}}_L^T(n-I+1) \end{bmatrix}. \quad (2.51)$$

With the filtered reference signals $\hat{\mathbf{R}}(n)$ the MIMO update law for the fxLMS is

$$\mathbf{w}(n+1) = \mathbf{w}(n) - \alpha \hat{\mathbf{R}}^T(n) \mathbf{e}(n). \quad (2.52)$$

In explicit form the operation is written as follows

$$w_{mki}(n+1) = w_{mki}(n) - \alpha \sum_{l=1}^L e_l(n) \hat{r}_{lmk}(n-i). \quad (2.53)$$

The computational power required for the compensator update law (2.53) can be reduced by adapting the filter only every N samples, as proposed by Snyder and Tanaka (1997). Additional approaches for controller optimization and further simplifications can be found in Elliott (2000).

3. Methods and Facilities

In this chapter, the working principle and the properties of the plasma actuator are introduced in section 3.1. The flat plate setup used for conducting the experiments with artificially generated 2D TS-wave disturbances and a single PA is described in section 3.2. Section 3.3 describes the optical setup and timing settings used for the PIV experiments. Natural transition scenarios are modeled in a wind-tunnel experiment with a multi-channel disturbance source and with a spanwise array of plasma actuators. The required 3D flat plate setup is presented in section 3.4. Experiments in a realistic flight environment were conducted on a wing glove, mounted on a manned motorized glider. The measurement equipment used for the in-flight experiments is presented in section 3.5. Finally, in section 3.6 the implementation of the flow control algorithms on the digital signal processor and offline simulation of the controller are explained.

3.1. Dielectric Barrier Discharge Plasma Actuator

The implemented dielectric barrier discharge (DBD) plasma actuator (PA) has been used in numerous experiments (e.g. Duchmann et al. (2014); Kurz et al. (2014)) and its electrical and fluid-dynamic properties have been investigated extensively over the years by Kriegseis et al. (2011, 2013b). The lower part of Fig. 3.1(a) shows the construction principle of the actuator: It consists of a 10 mm wide grounded lower copper electrode of $35\text{ }\mu\text{m}$ thickness and a 5 mm wide upper electrode divided by five layers of polyimide tape with a total thickness of 0.3 mm. The upper electrode is connected to a sinusoidal ($f_{\text{PA}} \approx 10\text{ kHz}$) high voltage V with a peak-peak amplitude of $V_{\text{pp}} \approx 10\text{ kV}$, causing the generation of a cold plasma discharge downstream of the upper electrode on the surface of the dielectric. The ionized air molecules are accelerated in the electric field, collide with other molecules and the resulting

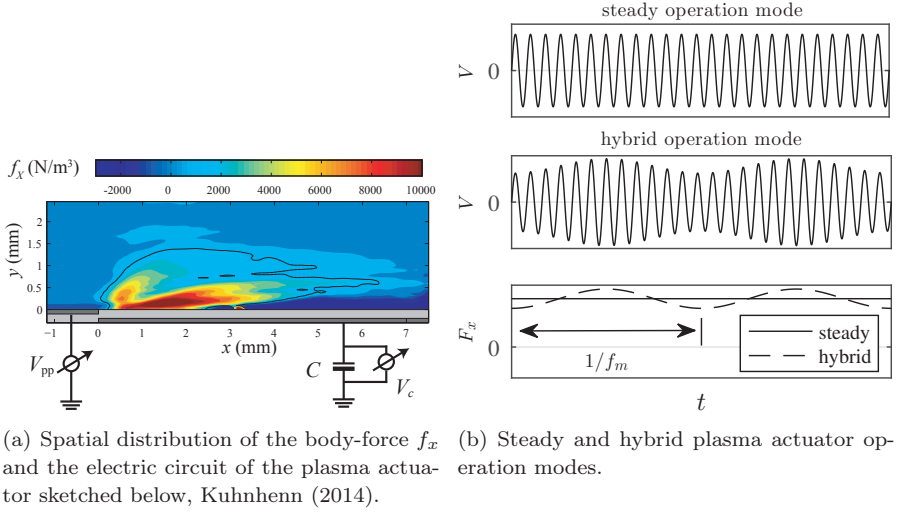


Figure 3.1.: Plasma actuator force and operation modes.

body force can be used for flow control. In the positive half-cycle of the operating voltage, the integral body force F_x is negative while in the negative half-cycle, F_x is positive (Boeuf et al. (2009); Kuhnhehn et al. (2016)). The positive force is slightly higher on the time scales of the BL ($f_{TS} < 1$ kHz) and the mean force is directed towards the covered electrode. The unsteady force production leads to a low fluid-dynamic efficiency $\eta_{FM} \approx 1\%$. Figure 3.1(a) exemplarily shows a contour plot of the spatial body-force distribution f_x of this actuator operated at 12 kV.

By modulating the amplitude of the driving AC voltage V_{pp} with a frequency of f_m (Fig. 3.1(b)), the resulting body-force can be altered in time (hybrid operation mode). Nevertheless, a mean force in downstream direction will always be present because of the unidirectional PA force. This mean body-force can improve the stability properties of the flow (boundary-layer stabilisation) whereas the modulated PA force is able to attenuate velocity fluctuations in the boundary layer (active wave cancellation). Accordingly, a hybrid operation mode is applied, if the steady part changes the stability properties of the mean flow significantly and the PA is additionally modulated in time for AWC (Kurz et al. (2013)).

The PA exhibits some drawbacks. Apart from the poor fluid-dynamic efficiency, one major problem is also the durability of the PA. At high operating voltages the dielectric, which is often a polyimide tape, degrades due to the generation of aggressive ozone. The high voltage and the exposed electrodes are problematic for some applications. In addition, the actuator can only work in air and is sensitive to humidity. However, the simple construction principle and the lack of moving parts avoid problems with eigenfrequencies/resonances as they occur with moving wall actuators (Pätzold (2013)) and the PA is easy to integrate into the surface, which is important for many aerodynamic applications. The PA is a zero-net mass-flux actuator; no tubes for the working fluid are required, only a high voltage cable for power supply.

High Voltage Generators Minipuls

Two different high voltage (HV) generators developed by GBS Elektronik, Minipuls 2.1 and Minipuls 0.2-5, are used for the experiments described in the following chapters. The construction principle of both devices is similar, but the number of individually controllable channels differs. One board, called bridge, consists of a switching power supply operated with a DC input voltage. The bridge creates an oscillating circuit together with the transformer cascade and the connected load, in this setup the PA. The amplitude of the sinusoidal HV output is controlled by an input signal ζ that translates a constant DC voltage to a sinusoidal HV with a certain amplitude V_{pp} . A control voltage of $\zeta = 1\text{ V} + 0.2\text{ V} \sin(2\pi f_m t)$ would then generate a HV signal with a modulation frequency f_m , as indicated in Fig. 3.1(b). In the following, the notation for the control voltage is $\zeta = 1 \pm 0.2$ in order to simplify the expression above. The operating frequency of the PA, f_{PA} , is set externally with a TTL signal.

The Minipuls 2.1 has one channel that generates HV signals up to a peak-to-peak amplitude of $V_{pp} = 20\text{ kV}$ at a frequency of $5\text{ kHz} < f_{PA} < 20\text{ kHz}$ and with a maximum output power of $P_{PA} = 120\text{ W}$. This device is used for all experiments that require only one actuator to generate a 2D even wavefront.

Experimental investigations on MIMO systems require the multi-channel HV generator Minipuls 0.2-5 in order to control the force of each actuator of a spanwise PA array individually. Figure 3.2 shows the five bridge boards with the transformer cascades, the small signal generation/synchronization board and a board for analog PA power monitoring on the left. In a spanwise

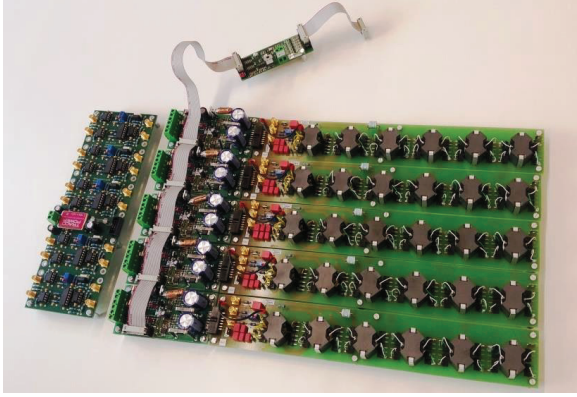


Figure 3.2.: High voltage generator Minipuls 0.2-5.

array of PAs, a high potential difference between the upper electrodes has to be avoided because arcing can damage the electrodes/dielectric and disturb the flow. Therefore, the Minipuls 0.2-5 is designed such that the HV signal at operating frequency f_{PA} is in phase for all actuators and only the modulation of the amplitude (cf. Fig. 3.1(b)) leads to a minor potential difference.

The Minipuls 0.2-5 has five channels that can generate high voltage signals up to $V_{pp} = 12\text{ kV}$ with a frequency of $5\text{ kHz} < f_{PA} < 20\text{ kHz}$ and with a maximum output power of $P_{PA} = 15\text{ W}$ per channel. This device is used for the 3D experiments with a MIMO system in Chapter 7.

The average PA power P_{PA} is important to monitor force amplitude and the health of the PA. PC based monitoring methods (Kriegseis et al. (2013a)) require high sampling rates ($f_S = 1\text{ MHz}$) and high computational power for data processing. Besides the Lissajous-figure method (Kriegseis et al. (2011)), the average PA power can be determined by the following simple procedure. The charge $Q(t)$ at the probe capacitor with the capacity C (Fig. 3.1(a)) is proportional to the measured voltage V_c :

$$Q(t) = C V_c(t). \quad (3.1)$$

The plasma actuator power $P_{PA}(t)$ can then be calculated by

$$P_{PA}(t) = V(t)I(t), \quad \text{with } I(t) = \frac{dQ}{dt}. \quad (3.2)$$

Based on previously conducted studies, GBS Elektronik developed an analog circuit that generates an analog signal according to (3.2). The output is a signal that is proportional to the average PA power (low pass at 1 kHz). The board enables a very efficient monitoring of multiple PA channels with a rather low sampling frequency of $f_S < f_{PA}$.

3.2. Flat Plate Setup for 2D Investigations

This section describes all components of the flat plate setup, used for the wind-tunnel experiments presented in Chapters 4 and 5. First, the wind tunnel itself and its features are introduced, followed by the flat plate with sensors/actuators. (The extended setup for the investigations on 3D wave cancellation with a MIMO system is introduced later in section 3.4).

Eiffel Wind Tunnel

The experiments are conducted in an open-circuit Eiffel type wind tunnel at Technische Universität Darmstadt, which provides a $450\text{ mm} \times 450\text{ mm}$ closed test section. The tunnel sucks the air from outside through the test section in order to avoid disturbances caused by the rotor. However, the open construction principle makes it susceptible for wind gusts and environmental parameters like temperature, humidity and density, which cannot be controlled. Within the scope of this project, a new wind-tunnel software has been successfully developed and tested. It enables control of the tunnel, control of a traverse system and synchronized data acquisition, as well as several online monitoring tools for the acquired signals and environmental conditions. New pressure sensors were implemented for a wind-tunnel speed measurement by a nozzle differential pressure method (Markus (2016a)).

The wind-tunnel speed can be set up to $U_{WT} = 60\text{ m/s}$, although experiments in this thesis were conducted only in the range of $7\text{ m/s} < U_{WT} < 17\text{ m/s}$. An average turbulence intensity of $Tu = 0.1\%$ has been measured at the end of the 1:24 contraction nozzle at a wind-tunnel speed of $U_{WT} = 12\text{ m/s}$.

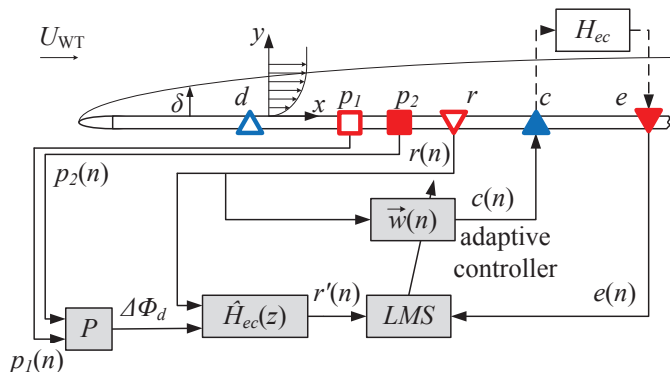


Figure 3.3.: Flat plate setup, equipped with a disturbance source d , three upstream sensors p_1 , p_2 and r , the plasma actuator c and a downstream error sensor e . The phase shift detection algorithm P extends the fxLMS controller sketched below the flat plate.

Overview of the Flat Plate Components

A 1.6 m long flat plate, equipped with an 1:6 elliptical leading edge and an adjustable trailing edge, is mounted horizontally at half height of the test section. Figure 3.3 shows a sketch of the flat plate; sensor and actuator positions are marked with symbols. A disturbance source d artificially generates TS-wave disturbances. Four surface hot-wire sensors (p_1 , p_2 , r and e) capture the velocity fluctuations as they propagate downstream. A single DBD plasma actuator c is placed between the reference sensor r and the error sensor e . A GBS Minipuls 2.1 high-voltage supply is driving the 270 mm long plasma actuator, installed flush mounted at $x_c = 363$ mm in a spanwise groove. By modulating the amplitude of the PAs operating voltage, an unsteady body-force is generated to cancel out the artificially generated TS-waves by superposition, cf. section 3.1. The 2D setup consists of only one actuator and one control circuit. Therefore, an artificial 2D transition scenario with an even wavefront is required. Natural transition with spanwise distributed wave packages would not allow 2D investigations. A modified version of the adaptive fxLMS algorithm is sketched in Fig. 3.3.

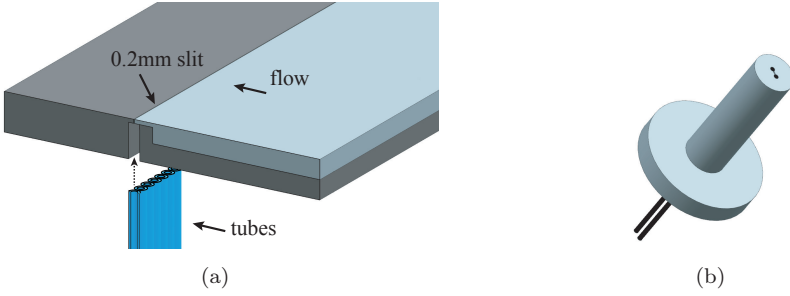


Figure 3.4.: (a) Disturbance source design: tubes are connected to a 0.2 mm wide slit. (b) Surface hot-wire sensor in a plastic case.

Disturbance Source and Sensors

The disturbance source d , positioned at $x_d = 225$ mm downstream of the leading edge, allows the generation of artificial TS-wave disturbances in the BL. It consists of 80 tubes, mounted below a 0.2 mm wide spanwise slit, cf. Fig. 3.4(a). The tubes are connected to 16 Visaton BF45 speakers, amplified by Kemo M031N audio amplifiers. Each of the 16 speakers is connected to five 1.2 m long tubes with an outer tube diameter of 3 mm. This construction principle is documented in literature (Borodulin et al. (2002)). A measurement system, based on a National Instruments NI9024 real time system equipped with a NI9264 16Ch analog output module, is used for signal generation. LabVIEW FPGA programming is used for deterministic and synchronized signal output with a rate of $f_S = 25$ kHz. A spanwise row of 30 Sennheiser KE 4-211-2 microphones is mounted at $x = 318$ mm with a spanwise spacing of $\Delta z = 9$ mm. Phase averaging of the microphone signals, acquired with a NI9205 A/D converter at $f_S = 4$ kHz, allows online monitoring of the disturbances in order to confirm the generation of two-dimensional disturbances.

Four surface hot-wires (p_1, p_2, r and e) are flush mounted at $x_{p_1} = 287$ mm, $x_{p_2} = 301$ mm, $x_r = 335$ mm, $x_e = 408$ mm and amplified by Dantec Streamline and DISA 55M0 CTAs. The surface hot-wires (Sturzebecher et al. (2001)) consist of two needles molded into a plastic case and a $5 \mu\text{m}$ thin and 1.25 mm long gilded-tungsten wire welded on top of the needles, cf. Fig. 3.4(b). All wires are operated at an overheat ratio of 1.7. The signals are bandpass

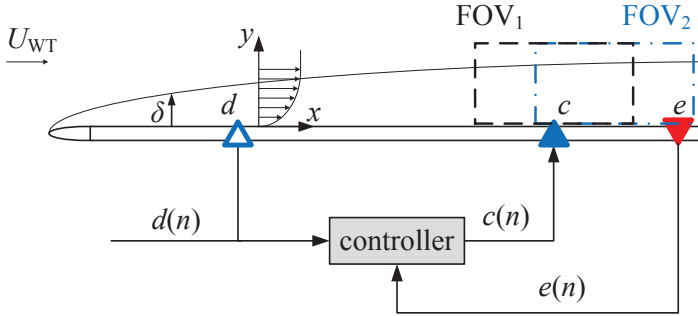


Figure 3.5.: Sketch of the flat plate setup used for PIV boundary layer measurements. The dashed boxes indicate the field of view (FOV); FOV₁ is centered at the PA c , while FOV₂ covers the PA and the error sensor e .

filtered (10 Hz to 1 kHz) and amplified by a factor of 32. The high signal-to-noise ratio favours this kind of sensor for this flow control application over hot-film sensors. A traversable hot-wire probe (Dantec 55P15) is mounted on a traversing system for conducting boundary-layer measurements, while a NI PCI6254 A/D converter acquires the low-pass filtered (3 kHz) signals at $f_S = 10$ kHz, synchronized with the disturbance generation.

3.3. Particle Image Velocimetry for Boundary-Layer Measurements

Particle Image Velocimetry (PIV) measurements were conducted on the flat plate in order to investigate the cancellation process of the TS-waves in direct vicinity of the PA. The results are shown in Chapter 4, while the required measurement setup and postprocessing methods are presented in the following. More detailed information can be found in Markus (2016b).

General PIV Setup

The 2D-2C (two dimensions, two velocity components) boundary layer PIV measurements are conducted with a high speed PIV System, consisting of a dual cavity Litron LDY303-PIV laser and two Phantom v12.1 cameras with

a resolution of $1280 \text{ px} \times 800 \text{ px}$. The cameras are aligned in streamwise direction in order to increase the measurement area in streamwise direction.

An 1.5 mm thick and approx. 80 mm wide laser sheet is guided through a window in the upper wall of the test section to the flat plate surface. The laser sheet is aligned in streamwise direction and in 150 mm distance from the left test section wall, where a window enables optical access for the cameras. The cameras and the laser can be operated at frequencies up to 6242 Hz in dual-frame mode but the flat plate surface material in the measurement region consists of 10 mm thick transparent acrylic glass, which can easily be damaged by the intense laser light. Therefore, the laser is only operated at 800 Hz in dual frame mode and at an output energy of 9.5 mJ per pulse.

Each camera is mounted on a Scheimpflug adapter, equipped with a Tamron 180 mm F/3.5 MACRO 1:1 lens and operated in dual-frame mode. The camera sensor width of 25.4 mm and the macro lens lead to an image width of $\approx 30 \text{ mm}$ and an average resolution of 45 px/mm . The images of both cameras are overlapped $\approx 5 \text{ mm}$ and the calculated velocity fields cross-faded afterwards. This leads to a total length of the field of view (FOV) of $\approx 55 \text{ mm}$. During the experiments the cameras were moved to two streamwise positions, while FOV_1 is centered at the PA position and FOV_2 is moved 20 mm downstream, cf. Fig. 3.5.

Vaporized DEHS seeding particles with an average size of $1 \mu\text{m}$ are introduced into the settling chamber of the wind tunnel via a vertical perforated tube. Investigations by Boucinha et al. (2008) showed no significant influence of the DEHS seeding particles on the discharge process.

Timing and Synchronization

The PIV equipment is timed with in-house Labview software using a NI6602 PCI digital timer card with a base clock of $f_b = 40 \text{ MHz}$. The phase-locked measurements only allow integer divisors of f_b for the disturbance generation frequency f_{TS} and the acquisition frequency of the PIV system f_{acq} , otherwise a phase shift will occur over time. The time between the frames is set to $\Delta t = 16 \mu\text{s}$ for a free-stream velocity of $U_e = 15 \text{ m/s}$. The chosen disturbance frequency of $f_{\text{TS}} = 250 \text{ Hz}$ and an acquisition rate of $f_{\text{acq}} = 800 \text{ Hz}$ lead to a resolution of 16 phase angles, acquired over five disturbance cycles with a phase resolution of $\Delta\Phi_{\text{TS}} = \pi/8 \text{ rad}$, cf. Fig. 3.6. A total number of 8216

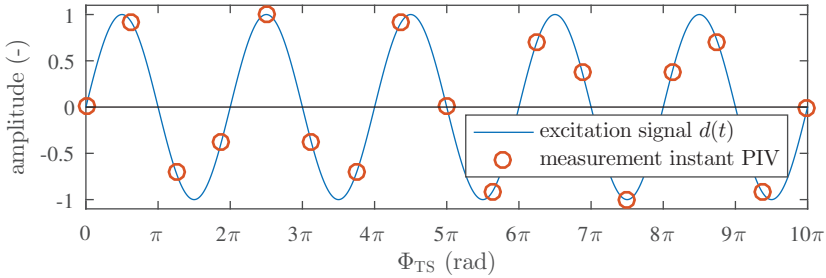


Figure 3.6.: Timing of the PIV image acquisition. The red dots show the 16 measurement points during five cycles of the disturbance excitation signal $d(t)$.

images are recorded for each measurement, limited by the camera memory. The available number of image pairs for each phase is then 256. A photodiode is placed close to the laser sheet and the voltage signal, induced by the laser pulses, is simultaneously recorded with the disturbance source driving signal. Postprocessing of both signals allows one to locate the relative phase angle of the first recorded image pair.

Image Pre-processing, Correlation and Velocity Field Dewarping

The average grey value of all image pairs is subtracted for each camera, reducing the wall reflections significantly. PIVview2C v3.5 is used for the image correlation. An adaptive correlation with a start interrogation area (IA) size of $256 \text{ px} \times 256 \text{ px}$ and a final size of $16 \text{ px} \times 16 \text{ px}$ with 50% overlap is used to obtain the velocity fields of the image pairs for each camera. The seeding density was not constant during the experiments. Therefore, a median test is applied in order to detect images with no or less seeding. Image pairs with less than 95% valid data points are removed from the data set.

The velocity fields are dewarped after image correlation for each camera separately. A dewarping of the raw images leads to a wave-like artifact-pattern in the correlated velocity fields, caused by a limited accuracy of the dewarping procedure. The amplitude of the pattern is of the order of the TS-wave amplitude and not acceptable. The dewarping/mapping is based on images of a calibration target, which consists of a dot pattern with a dot diameter of 1.5 mm and 2.375 mm dot spacing. The calibration target was machined with

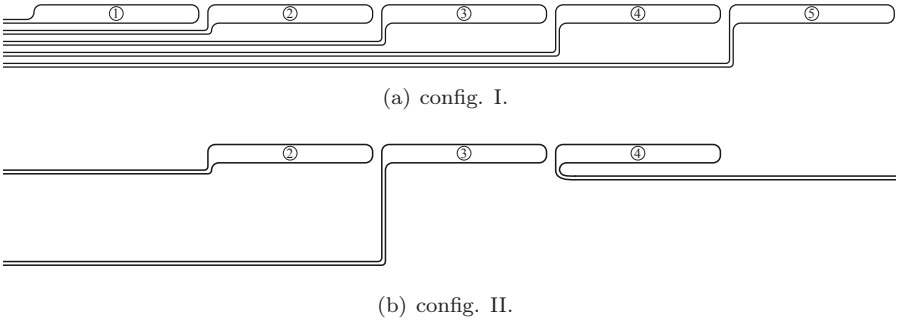


Figure 3.7.: Design of the upper electrodes of two different PA array configurations.

a milling cutter from a white coated black HDPE plate. Compared to printed targets, the edges of the dots are sharper and the dot spacing is more accurate. After the calibration pictures are taken, a MATLAB routine automatically detects the centers of the dots and a 3rd order polynomial approach is applied for the coordinate transformation (Markus (2016a)). The dewarped velocity fields are mapped onto a common grid with twice the resolution of the IAs and linearly cross-faded in the overlap region of both cameras.

3.4. Flat Plate Setup for 3D Investigations

The 2D setup (section 3.2) is modified in order to investigate the spanwise plasma actuator array and the MIMO control circuit in Chapter 7. The streamwise position of the DS, sensors and PA is not changed but additional sensors/actuators in spanwise direction are mounted on the flat plate.

In total, five plasma actuators can be operated simultaneously with the Minipuls 0.2-5 HV generator but only three actuators are operated for the investigations presented in Chapter 7. The electromagnetic and fluid dynamic effects at centered PA and the outer PAs can be observed well with this simplified setup. The upper PA electrodes have a length of 42.5 mm, a spacing of $\Delta z_{PA} = 45$ mm and a 2.5 mm wide gap in between, cf. Fig. 3.7. A cutting plotter is used to cut the electrodes from a $35\ \mu\text{m}$ thin adhesive copper foil. The lower electrodes are also separately cut out of the copper foil to allow for a measurement of P_{PA} for each actuator individually, which is not possible

with one common electrode. The width of all electrodes is 5 mm and the connectors are also a part of the cutout. Hence, soldering is not required in the centered region on the flat plate and a rather smooth surface is provided for laminar flow.

Two configurations of the connector lines are tested to investigate the influence of electromagnetic interference between the PAs, cf. Fig. 3.7. Capacitive coupling is likely to induce a current in a neighboured high-voltage cable, which is depicted in Fig. 3.8. The parasitic current I_{pc} is induced due to the capacitance C_{pc} , which is caused by parallel wiring of the HV cables 1 and 2. The term dV/dt in equation (3.3) indicates the impact of the operating frequency f_{PA} on the parasitic current. If f_{PA} is fixed, the capacitive coupling can be minimized by a reduction of C_{pc} , which is done for config. II (Fig. 3.7(b)) by guiding the cables with a maximum distance. Shielded HV cables are not an option because the shielding capacitance is an additional load for the HV generator and the dielectric of the cable is heated up.

The sketch in Fig. 3.9 shows the sensors/actuators that are used for the 3D investigations. Nine slots with a spanwise spacing of $\Delta z = 15$ mm are available for the reference and error sensors. The slots allow for a flexible positioning of the eight available surface hot-wires, amplified by a 2Ch DISA 55M0 and a 6Ch Dantec Streamline CTA. All signals are bandpass filtered (10 to 1000 Hz) and amplified by a factor of 64. The sensors are not calibrated but normalized with the RMS of each individual sensor for the fully turbulent BL case that is provoked by a zig-zag tape just in front of the disturbance source. The disturbance source consists of 15 channels d_0 to d_{14} , while only the spanwise extend of d_3 to d_{11} is shown in Fig. 3.9. All measurements presented in Chapter 7 have been conducted with only 3 PAs connected to the HV generator Minipuls 0.2-5.

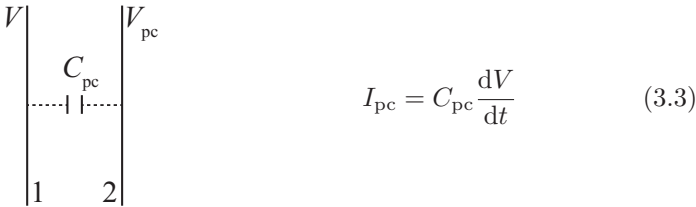


Figure 3.8.: Capacitive coupling.

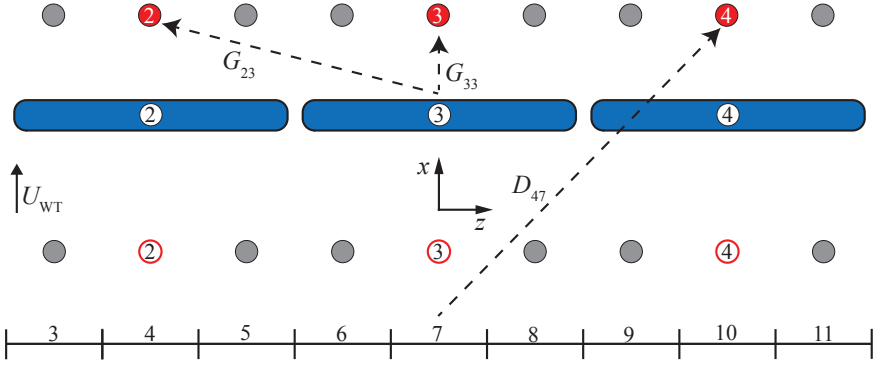


Figure 3.9.: Sketch of the flat plate setup for 3D investigations, equipped with an array of three PAs (blue rectangles). Surface hot-wires are mounted as reference (red circle) and error sensors (red dots), while grey dots indicate free slots for sensors. The spanwise extend of the disturbance source channels (d_3 to d_{11}) is indicated below. Transfer paths G_{23} , G_{33} and D_{47} are exemplarily shown.

Infrared (IR) thermography is used to measure laminar-turbulent transition and vortices on the flat plate surface. The higher friction coefficient c_f is directly related to a higher heat transfer coefficient h via the Reynold's analogy. A FLIR Tau 2 640 IR camera is installed in the wind tunnel and measures the temperature on the heated insert that consists of an insulating foam with a low thermal diffusivity α and is covered with a black foil that extends from $x = 454\text{ mm}$ downstream, cf. Fig. 3.10. Detailed information on the measurement principle and the IR heater can be found in Simon et al. (2016b).

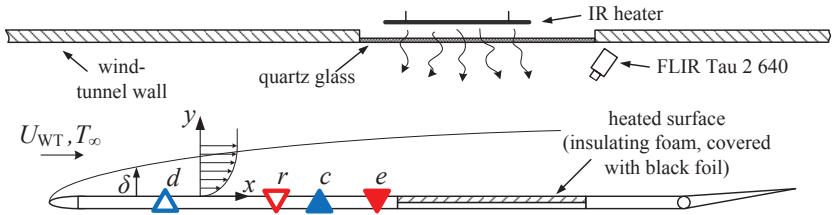


Figure 3.10.: Flat plate setup with IR measurement system installed.

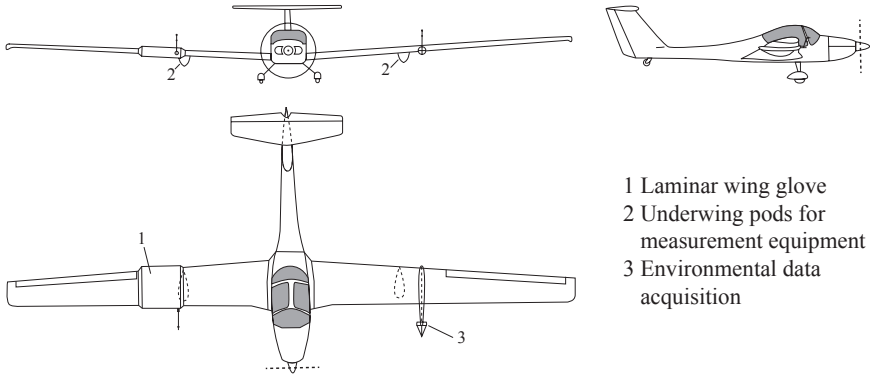


Figure 3.11.: Grob G109b research aircraft.

3.5. Experimental Flight Setup

The unique opportunity to combine in-flight and wind-tunnel experiments is possible because TU Darmstadt owns its own airfield in direct proximity to the wind-tunnel facilities. A motorized glider serves as a flying platform with a wing glove mounted on the right wing. The instrumentation of the glove is described in section 3.5.1 and the in-flight testing procedure discussed in section 3.5.2.

Research Aircraft Grob G109b

The in-flight experiments are conducted with a manned Grob G109b motorized glider, which combines the advantages of vibrationless gliding flight with a 96 kW engine for take off and altitude gain. The three-view drawing in Fig. 3.11 shows the glider with a wing span of $b = 17.4$ m and a wing aspect ratio of 15.9. The sweep angle is close to zero, leading to a negligible span-wise pressure gradient and an almost two-dimensional flow along the chord. A temporary 'permit to fly' allows an additional payload for the measurement equipment and leads to a maximum take-off weight of 950 kg. Due to flight speed limitations, the angle of attack exploitable for the experiments ranges between $\alpha = -3^\circ$ and $\alpha = 13^\circ$. The flight speed is $U_\infty \approx 41$ m/s for $\alpha = 2.5^\circ$, but the actual value depends on the environmental conditions and altitude.

The environmental data acquisition equipment is mounted on the left wing

of the glider, cf. Fig. 3.11. The angle of attack α and the sideslip angle β are measured with a *Dornier Flight Log*, which is a windvane mounted on a second boom. The atmospheric pressure p_∞ (Setra 270), dynamic pressure p_{dyn} (Setra 239HP), humidity (Hygrosens CON-HYTEMODI2C) and temperature T_∞ (Typ K thermocouple) are measured upstream of the left wing.

3.5.1. Laminar Wing Glove

The right wing of the glider can be equipped with a NLF airfoil wing glove. The airfoil (Fig. 3.12) was developed by Weismüller (2012) to quantify the influence of atmospheric turbulence on NLF airfoils. Reeh and Tropea (2015) intensively investigated the flow around the airfoil in flight. The flat airfoil shape on the pressure side creates an almost linear pressure gradient that is adjustable between moderate positive and negative values by changing α . The flow was shown to be 2D in the inner region of the wing glove by Reeh (2014). All base flow considerations and resulting pressure distributions are discussed later in section 6.1.

The hydrodynamic stability of the boundary layer has consequences for the design of natural laminar flow airfoils. The flow is accelerated over a long percentage of chord on the pressure and suction side due to a maximum thickness of the airfoil at around mid-chord, cf. Fig. 3.12. This acceleration causes a stable BL and attenuated TS-wave disturbances. The airfoil shape on the suction side changes rather quickly downstream of the maximum thickness and leads to a high amplification of the TS-waves and a breakdown to turbulence. As shown by Reeh (2014), the transition location on the suction side of the considered airfoil moves only a few percent chord while the transition on the pressure side moves from $\frac{x_{\text{crit}}}{l} \approx 0.3$ to $\frac{x_{\text{crit}}}{l} \approx 0.6$ for a change of the angle of attack α of 2° . The wide range of x_{crit} is caused by the flat shape of NLF airfoils on the pressure side. The rather low amplification of the TS-waves over a long distance makes the pressure side beneficial for active wave cancellation. The waves have to be sensed, which requires a certain amplitude, and the counter wave has to interact with the incoming wave further downstream.

The wing glove itself (Fig. 3.13) forms a square shape with a chord length of $l = 1.35$ m and is slipped over the wing. The pressure distribution is measured with 64 pressure taps distributed over the suction and pressure sides of the wing glove. Signals are acquired with 10 Hz by a Pressure Systems ESP-64HD

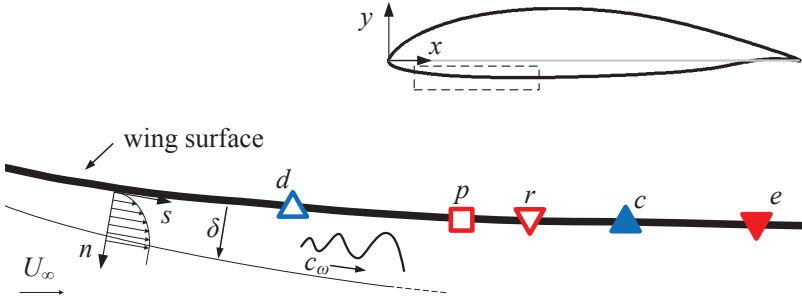


Figure 3.12.: Shape of the MW-166-39-44-43 airfoil and sensor placement on the pressure side of the wing glove.

pressure transducer with a range of ± 2490.82 Pa. The reference atmospheric pressure p_∞ is obtained using a boom protruding upstream into the flow. The chord-based Reynolds number of the wing glove is $Re_l \approx 3.75 \cdot 10^6$.

An exchangeable plexiglass insert is arranged flush mounted to the surface (Fig. 3.13) and accommodates the sensors and actuators. The disturbance source d is located at $x_d/l = 0.18$ and consists of 12 miniature loudspeakers installed underneath the plexiglass insert in spanwise direction with a spacing of 20 mm. A circular array of six 0.2 mm holes connects each speaker to the aerodynamic surface (Duchmann et al. (2014)). Three surface hot-wires probes p , r and e are located at $x_p/l = 0.26$, $x_r/l = 0.29$ and $x_e/l = 0.38$. The in-house manufactured hot-wire sensors are flush mounted to the surface and consist of two needles molded in a plastic case with a 1.25 mm long and $5 \mu\text{m}$ thin gold-plated tungsten wire welded on top, cf. Fig. 3.4(b). All hot-wires are operated by Dantec MiniCTA constant temperature anemometers. A signal conditioner filters the analog signals (first-order bandpass 50 Hz to 3.8 kHz) and amplifies the signal fluctuations by a factor of 400.

The PA c is positioned flush mounted in a groove at $x_c/l = 0.33$. The driving high voltage signal is generated at a fixed frequency of $f_{\text{PA}} = 9.8$ kHz by a GBS Minipuls 2.1. In spanwise direction, the PA is 230 mm long and a 2D behavior is assumed. The following geometrical distances between sensors and actuator have been measured at the wing glove:

$$\Delta x_{pr} = 35 \text{ mm}, \quad \Delta x_{rc} = 47 \text{ mm}, \quad \Delta x_{ce} = 76 \text{ mm}.$$

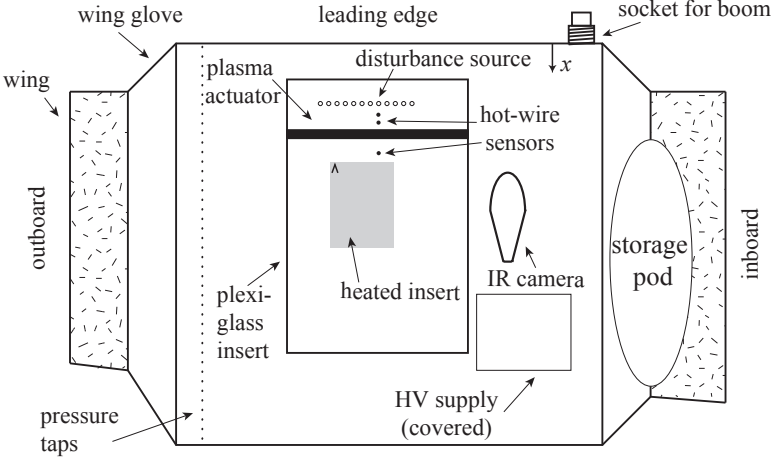


Figure 3.13.: Sketch of the wing glove pressure side.

IR Camera and Heated Insert

An infrared (IR) camera is mounted on the wing glove in order to monitor the laminar-turbulent transition on the wing glove and identify turbulent spots caused by a contaminated leading edge or surface roughness (sensors, tape).

IR thermography requires a temperature difference between the flow and surface temperatures. A flush-mounted heated insert consisting of an electrically heated foil allows variable heat transfer up to 2000 W/m^2 . The insert extends from $x/c = 0.4$ to $x/c = 0.62$ and has a width of 200 mm. More information about the design of the setup, postprocessing techniques and the IR measurement technique itself can be found in Simon et al. (2016c). The mid-wave ($7.5\text{--}13 \mu\text{m}$) IR camera Flir Tau 2 640 (13 mm lens) is equipped with a Automation Technology GigE Vision Adapter and provides an uncalibrated 14bit data stream at 8.3 Hz. The GigE Vision standard supports cable lengths up to 100 m and comfortable implementation in Labview. The camera itself is an uncooled thermal imager based on microbolometer technology. This leads to a slightly worse signal-to-noise ratio as compared to cooled IR cameras but it is significantly smaller and economically more attractive. As all measurements are taken on the pressure side of the wing glove, the

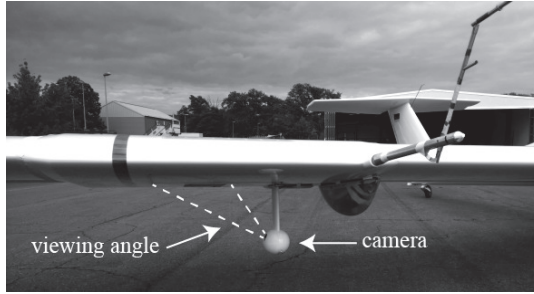


Figure 3.14.: Wing glove, mounted on the glider wing and IR camera with fairing.

space for the IR camera is limited. Due to the small dimensions of the camera ($45\text{ mm} \times 45\text{ mm} \times 60\text{ mm}$) it is possible to mount the camera directly on the wing glove. A stand of 280 mm height ensures a reasonable viewing angle of about 45° , resulting in 90% IR radiation intensity as compared to a normal viewing angle (Vollmer and Möllmann (2010)). With a resolution of $640\text{ px} \times 512\text{ px}$, the minimum spatial resolution for the heated insert is 0.75 mm/px in spanwise and 0.73 mm/px in streamwise direction. The viewing angle and the slightly curved surface of the wing glove make dewarping necessary. Camera and stand are covered with a fairing in order to reduce drag and vibrations, cf. Fig. 3.14.

An onboard 24 V DC lead acid battery with a capacity of 16 Ah allows a measurement system operation time of about 1 h . More details about the measurement procedure is given in the following.

3.5.2. In-Flight Testing Procedure

The in-flight experiments presented in this thesis enable boundary-layer measurements in a realistic flight environment. It does not, however, determine the performance parameters of the aircraft as flight testing is usually understood. Nevertheless, the measurements are related to flight mechanics, environmental conditions and flight planning – challenges that only exist for measurements under flight conditions (Joslin (1998)). Despite the difficulties of in-flight measurements compared to wind-tunnel tests, there are reasons for experiments on an airplane wing in flight. The investigations of

Weismüller (2012) on the atmospheric turbulence indicate the need for in-flight experiments, as the turbulence intensity is very low. More importantly, isentropic turbulence is achievable for high Reynolds numbers. Acoustic disturbances make the investigation on natural transition in the wind tunnel difficult as the ambient noise can influence the receptivity. Last but not least, a flow control technology in flight is very close to its intended application.

The measurement time, preparation, maintenance and costs exceed the effort for wind-tunnel experiments by far. For the current setup, one test flight of 1.5 h includes only 20 min of measurement time, the rest of the time is spent on cruise flight and altitude gain. During a measurement flight, the glider climbs up to an altitude of 10,000 ft and the pilot switches off the engine. As soon as the propeller is turned away from the wind, the pilot starts to adjust the angle of attack α according to the flight display in front of him; an online visualization of the low-pass-filtered values for α and the sideslip angle β assists the pilot in setting and maintaining the desired flight state. Flight mechanics couple flight speed U_∞ and α depending on the weight, required lift, density of the air and other parameters and therefore do not enable the same boundary conditions for each flight, even during one single gliding flight. Numerical studies based on linear stability analysis concerning these issues have been conducted by Duchmann (2012). They revealed a stronger sensitivity of the streamwise position of the naturally occurring transition to changes of the angle of attack than to a slowly drifting Reynolds number. This is also confirmed by the experimental and DNS results in Chapter 6. Therefore, the active flow control experiments in gliding flight are conducted for a constant angle of attack instead of at constant Reynolds number. After the engine is switched off, the first measurement run can be recorded in gliding flight at an altitude of 9,000 ft; the measurements have to be stopped at an altitude of about 3,000 ft to turn back on the engine. The measurement time of one gliding flight is about 10 min, while typically 15 measurement runs of 20 to 40 s are recorded. All experiments are conducted early in the morning under calm conditions to avoid fluctuations in α . Unavoidable limitations to in-flight experiments are given by traffic, inversion layers and the battery power supply for measurement equipment.

3.6. Implementation and Execution of the Control Algorithms

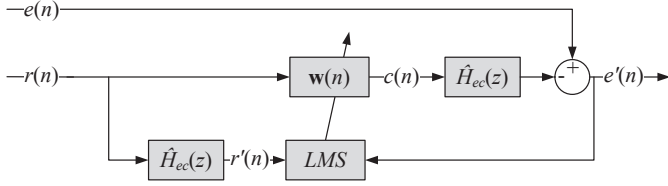
The control algorithms described in section 2.2 have to be executed in real time for the active wave cancellation experiment. The company dSPACE offers development platforms for real-time control applications consisting of a digital signal processor and corresponding software described in the following. Furthermore, the offline-controller simulation in MATLAB/Simulink is described in this section.

dSPACE Digital Signal Processor

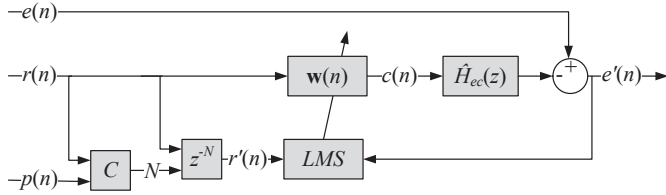
A dSPACE digital signal processor, consisting of a DS1007 processor board, a DS2004 A/D board and a DS2102 D/A board mounted in a dSPACE Auto-Box acquires the hot-wire signals and generates the signals for the the high-voltage generator. The system is operated by a DC power supply and fits to the measurement platform of the experimental flight setup, cf. section 3.5. The algorithms are implemented in MATLAB/Simulink, compiled and transferred to the dSPACE processor board with the required dSPACE toolbox. After this process, the dSPACE system is controlled with a software called dSPACE ControlDesk. It allows to start the control algorithms, monitoring and recording sensor signals. The system enables of operating the fxLMS algorithm at a sampling frequency of $f_S = 20 \text{ kHz}$ (SISO), and the multi-processor board (dual core) also allows an optimized program structure for more complex MIMO systems.

Offline Controller Simulation

The knowledge of all transmission paths of the flow control problem makes an offline investigation of the fxLMS and dxLMS controller behavior possible. Either the sensor signals of an experiment or the DNS solution of a flow field can describe the required paths between sensors and actuators. This offline controller simulation in MATLAB/Simulink saves measurement time and also allows detailed preparation for the flight tests, where time is valuable. In the following, the controller simulations based on experimental data and DNS are discussed.



(a) fxLMS.



(b) dxLMS.

Figure 3.15.: Block diagram for controller simulation with experimental data.

For the identification of the secondary path model \hat{H}_{ec} during an experiment, the Minipuls high voltage generator is operated with a pseudo-random binary signal (PRBS). This results in a modulated high voltage signal at the PA and broadband TS-waves are generated. The transmission behavior of H_{ec} can either be estimated online with a LMS algorithm or calculated offline, cf. (2.24). The magnitude and phase information contained in $\hat{H}_{ec}(\omega)$ can then be converted to a digital FIR filter $\hat{H}_{ec}(z)$, e.g., with the *invfreqz* command in MATLAB. For offline controller simulation, a record of an experimental case with only the disturbance source in operation is required (uncontrolled case). The discrete reference and error sensor signals $r(n)$ and $e(n)$ are the input signals for the fxLMS offline controller simulation as indicated in Fig. 3.15(a). The incoming reference sensor signal $r(n)$ is therefore the same as if the controller would be operated during the experiment and the filtering of $r(n)$ with \hat{H}_{ec} is exactly the same as in the experiment. Because

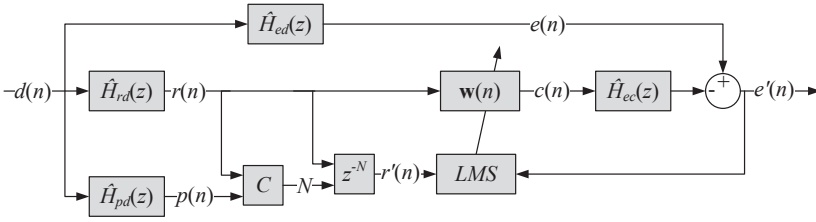


Figure 3.16.: Block diagram for offline controller simulation with transfer paths obtained with DNS.

the controller actuation is only performed offline, the physical transmission path H_{ec} has to be modelled and $c(n)$ is filtered by \hat{H}_{ec} . The result is then subtracted from the measured “desired” signal $e(n)$, and the simulated error sensor signal $e'(n)$ is the second input for the LMS adaptation algorithm. It is obvious that this procedure can not completely describe the conditions in flight, because the estimated paths \hat{H}_{ec} in the upper and lower row in Fig. 3.15 are exactly the same. In a real case the physical transmission path H_{ec} changes due to varying inflow conditions and can even cause an unstable controller behavior as discussed later in Chapter 5 and Chapter 6.

Figure 3.15(b) shows the block diagram for the dxLMS offline controller simulation with recorded experimental data. The only difference to the fxLMS approach in Fig. 3.15(a) is the filtering of $r(n)$ and the online adaptation of the delay N , cf. section 2.2.4.

Direct numerical simulations (DNS) allows one to extract detailed information of the boundary-layer transmission behavior. For the given problem, the FIR filter coefficients of the transfer path models \hat{H}_{pd} , \hat{H}_{rd} , \hat{H}_{ed} and \hat{H}_{ec} are available and implemented in the controller simulation as shown in Fig. 3.16. Analogous to the experimental data controller simulation, the reference sensor filtering can be changed for fxLMS controller simulation, cf. Fig. 3.15. The incoming disturbances are not in-flight sensor data, but a white noise signal $d(n)$ is the only input signal required for the DNS data controller simulation.

4. Phase-Locked Particle Image Velocimetry Measurements

The active wave cancellation of the Tollmien-Schlichting waves in the laminar boundary layer has been conducted with different kinds of actuators, but is not yet fully understood. Broad-band waves do not allow the investigation of the cancellation process, but only phase-locked measurements of artificially generated single-frequency TS-waves can yield insight into the process. Moving wall actuators and especially plasma actuators do not allow the application of intrusive measurement techniques like hot-wire anemometry. Therefore, optical measurement techniques like particle image velocimetry (PIV) are the only option to measure the velocity field in direct vicinity of the actuator.

Measurements by Widmann et al. (2012) demonstrated the possibility to measure artificially generated single-frequency TS-waves by phase-locked PIV for the first time. The technique was then implemented to investigate the interaction between TS-waves and a PA, operated in boundary-layer stabilisation mode (Widmann et al. (2013)). Inspired by the measurements of Widmann, Amitay et al. (2016) measured the effect of the active cancellation of TS-waves downstream of a point-wise moving wall actuator by means of PIV.

In this thesis, the TS-waves are artificially generated with a disturbance source (DS) at a frequency of $f_{\text{TS}} = 250 \text{ Hz}$, which is in the amplified frequency band for the 2D zero pressure flat-plate boundary layer at a free-stream velocity of $U_e = 15 \text{ m/s}$. The TS-wave disturbances travel downstream and are attenuated with AWC by an unsteady PA force. Phase-locked PIV measurements with a high-speed PIV system allow for fast measurements at an acquisition rate of $f_{\text{acq}} = 800 \text{ Hz}$ in double frame mode, resolving 16 phase angles of the wave cycle, cf. section 3.3.

The investigations in this chapter are based on six measurement configu-

rations, summarized in table 4.1. The measurements, corresponding to the settings in the table, were conducted in order to answer the following questions:

1. Is the undisturbed (natural) base flow a 2D laminar Blasius boundary layer? (section 4.1)
2. How does the steady PA force offset alter the boundary layer? (section 4.2)
3. Do the disturbances generated by the disturbance source have TS-wave character? (section 4.3)
4. How does the steady PA force influence the shape and the amplification of the incoming TS-waves? (section 4.4)
5. Do the counter-waves generated by the PA have TS-wave character? (section 4.5)
6. How do the incoming TS-waves interfere with the counter-waves, generated by the PA in AWC mode? (section 4.6)

Table 4.1.: Measurement configurations of the plasma actuator and disturbance source for the phase-locked PIV measurements.

#	disturbance source	plasma actuator
1	off	off
2	off	steady forcing
3	on, 250 Hz	off
4	on, 250 Hz	steady forcing
5	off	unsteady forcing, 250 Hz
6	on, 250 Hz	unsteady forcing, 250 Hz

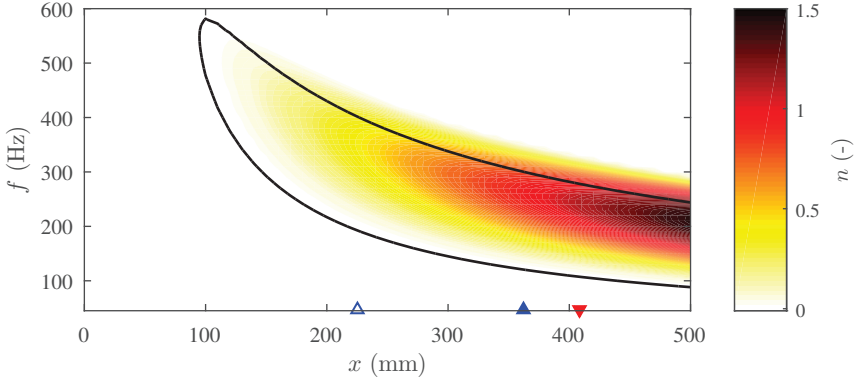


Figure 4.1.: Neutral stability curve (black line, $k_{x,i} = 0$) and n -factor contours for a zero pressure gradient BL and $U_e = 15 \text{ m/s}$, spanwise wavenumber $k_z = 0$. The symbols indicate the positions of actuators and sensors, cf. Fig. 3.5.

4.1. Base Flow on the Flat Plate

The phase-locked PIV measurements were conducted on a flat plate at a free-stream velocity of $U_e = 15 \text{ m/s}$. This is a low disturbance amplification scenario, as shown in the corresponding stability diagram for a Blasius boundary layer in Fig. 4.1. All linear stability theory (LST) computations presented in this chapter have been conducted with a code provided by Reeh (2014) and modified by Turkac (2016). A Blasius BL with a freestream velocity of $U_e = 15 \text{ m/s}$ and a kinematic viscosity of $\nu = 14.29 \cdot 10^{-6} \text{ m}^2/\text{s}$ is assumed. The disturbance source d , placed at $x_d = 225 \text{ mm}$ (\triangle), generates single-frequency 2D disturbances with an even wavefront at a frequency of $f_{\text{TS}} = 250 \text{ Hz}$. The disturbance frequency is in-between the neutral stability curve ($k_{x,i} < 0$) and is therefore amplified for the considered region between the disturbance source and the error sensor e , mounted at $x_e = 408 \text{ mm}$ (\blacktriangledown). The low amplification scenario is chosen in order to ensure a dominant role of the artificial 2D waves in the considered measurement region around the PA c , placed at $x_c = 363 \text{ mm}$ (\blacktriangle).

The base flow measurements presented in the following are only valid for one specific case. The open return wind-tunnel design does not provide constant environmental conditions, cf. section 3.2. Reynolds number and stability

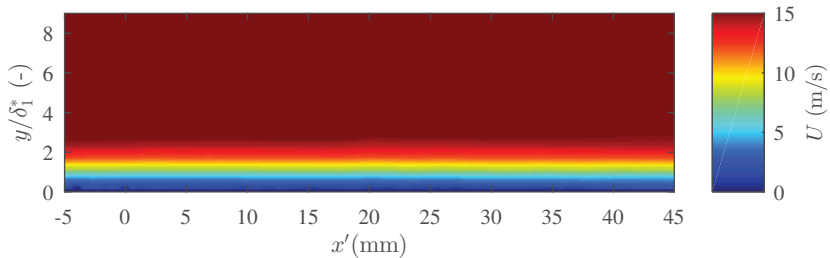
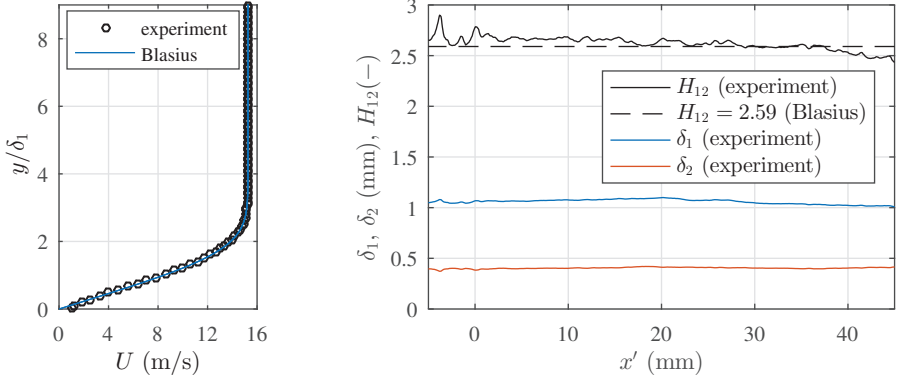


Figure 4.2.: Mean flow field of FOV₂, the plasma actuator is located at $x' = 0$ mm. The wall normal coordinate is normalized with the displacement thickness at the beginning of the domain δ_1^* , at $x' = -5$ mm.

properties of the boundary layer change slightly from day to day. Measurements that are compared directly in the following discussion were recorded within a short time frame of about one hour. It is assumed that the flow parameters are constant during that time frame.

The mean flow field, obtained by correlation of both camera images, is shown in Fig. 4.2. A new streamwise coordinate x' is introduced, where $x' = 0$ is located at the edge of the upper PA electrode ($x_c = 363$ mm). The wall normal coordinate y is normalized with the displacement thickness at the beginning of the domain δ_1^* , at $x' = -5$ mm. As described in section 3.3, the velocity fields are first computed for each camera individually, dewarped afterwards and interpolated on a common grid. The velocity field of two different FOVs have been measured. In FOV₁ the PA is centered and the incoming TS-waves upstream of the PA can be investigated. FOV₂ resolves the velocity field mainly downstream of the PA, including the error sensor position at $x' = 45$ mm, cf. Fig. 3.5. In the following, both FOVs are presented, dependent on the discussed phenomena.

The velocity profile in Fig. 4.3(a), extracted from Fig. 4.2 at $x' = 24.9$ mm, shows good agreement with the zero-pressure gradient Blasius boundary layer. More significant is the comparison of the BL parameters $\delta_1(x')$, $\delta_2(x')$ and $H_{12}(x') = \frac{\delta_1(x')}{\delta_2(x')}$ in Fig. 4.3(b). The displacement thickness δ_1 and the momentum thickness δ_2 are almost constant for the entire velocity field and the measured shape factor H_{12} is close to the Blasius solution ($H_{12} = 2.59$). The upper electrode of the PA extends from $x' = -5$ mm to $x' = 0$ mm and has a thickness of $35 \mu\text{m}$. It passively influences the boundary-layer development



(a) Measured velocity profile at $x' = 24.9$ mm and corresponding Blasius solution. Every second data point is shown for clarity.

(b) Measured boundary-layer parameters δ_1 , δ_2 , H_{12} and $H_{12} = 2.59$ (Blasius solution).

Figure 4.3.: Measured boundary-layer profile and parameters as well as the corresponding Blasius solution for the base flow of FOV₂.

due to its presence, but also reflections at the copper electrode falsify the PIV measurements. Both issues cause noisy data of the BL parameters for $x' < 2$ mm but the data downstream of the actuator verifies the laminar Blasius BL. The Blasius character of the undisturbed flow is the basis for further investigations on artificially generated TS-waves and comparison with linear stability theory in section 4.3.

4.2. The Effect of Steady Plasma Actuator Forcing on the Base Flow

The PA generates an unsteady volume force on the time scale of the PA driving frequency ($f_{PA} \approx 10$ kHz), but the characteristic frequencies of the BL are more than an order of magnitude lower. Hence, the volume force can be considered steady. The steady downstream directed integral PA force F_x is present from the moment the plasma ignites and is proportional to the

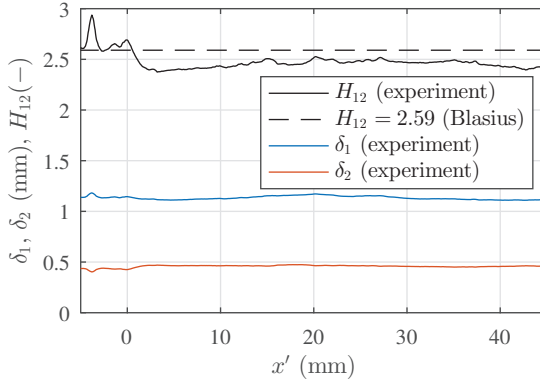


Figure 4.4.: Measured boundary-layer parameters δ_1 , δ_2 , H_{12} and $H_{12} = 2.59$ (Blasius solution) for FOV_2 . The PA is operated at $V_{\text{pp}} = 7 \text{ kV}$.

consumed electrical power $P_{\text{PA}} \propto F_x$ over the range employed in this study, cf. section 3.1. Because the PA can only generate a downstream directed force, a steady force offset is always present in AWC mode. The steady force offset has a stabilising effect on the laminar BL, as shown before (Duchmann et al. (2014); Simon et al. (2016c)). In this thesis the active wave cancellation is the investigated mechanism. Therefore, the mean amplitude of the driving high-voltage signal is set to $V_{\text{pp}} = 7 \text{ kV}$, equivalent to an integral steady force offset of $F_x \approx 1 \text{ mN/m}$. Studies on BL stabilisation were conducted with $F_x > 10 \text{ mN/m}$, the expected stabilising effect on the BL is therefore comparably weak.

Figure 4.4 shows the effect of the steady PA force on the base flow. The BL parameters δ_1 , δ_2 and H_{12} are presented for FOV_2 , which mainly shows the development of the BL downstream of the PA. The displacement thickness δ_1 is almost constant, whereas δ_2 increases slightly downstream of the PA and results in a lower H_{12} compared to Fig. 4.3(b). The relatively low steady force offset leads to a more stable BL and an attenuation of the TS-wave amplitude, as confirmed later in section 4.4. These findings agree well with previous studies by Grundmann and Tropea (2009) and Duchmann et al. (2013), who also showed decreased values of H_{12} downstream of the PA for a steady PA force.

4.3. Artificially Generated Tollmien-Schlichting Waves

In the following, the Tollmien-Schlichting character of disturbances, generated artificially by the disturbance source, is verified. The disturbance source enables 2D and 3D disturbance scenarios, but for this experiment an even 2D wavefront is generated because 2D2C PIV measurements are conducted with a single PA. The amplification of the TS-waves can be described by LST. The receptivity of the BL for (natural) TS-waves does not only depend on the surface roughness but also on noise and the inflow quality. The sensitivity of the receptivity on the inflow quality is discussed in section 4.3.1, followed by the characterisation of the artificially generated TS-waves in section 4.3.2.

4.3.1. Influences on the Tollmien-Schlichting Wave Generation

The influence of the inflow quality on the receptivity process is important for the development of (natural) TS-waves. Two factors have been identified and are investigated further: first, the influence of a slit for the seeding traverse in the settling chamber wall and second, the influence of the seeding generation in the settling chamber.

Slit in the Settling Chamber Wall

The seeding is introduced into the test section via a perforated tube, mounted vertically in the settling chamber of the wind tunnel. A traverse can move the tube in spanwise direction and therefore requires a slit in the settling-chamber wall. An improper sealing of the slit can significantly lower the inflow quality in the test section. A free-stream velocity of $U_e = 12 \text{ m/s}$ was set for the first experiments on the disturbance generation, where the setup has been optimized. All other measurements in this chapter were conducted at $U_e = 15 \text{ m/s}$. However, the effects that are discussed in the following can be observed for both velocities. Artificial TS-waves are generated by the disturbance source at $f_{\text{TS}} = 200 \text{ Hz}$, which is in the amplified frequency band for the free-stream velocity of $U_e = 12 \text{ m/s}$.

Figure 4.5(a) presents the power-spectral density (PSD) of the error-sensor

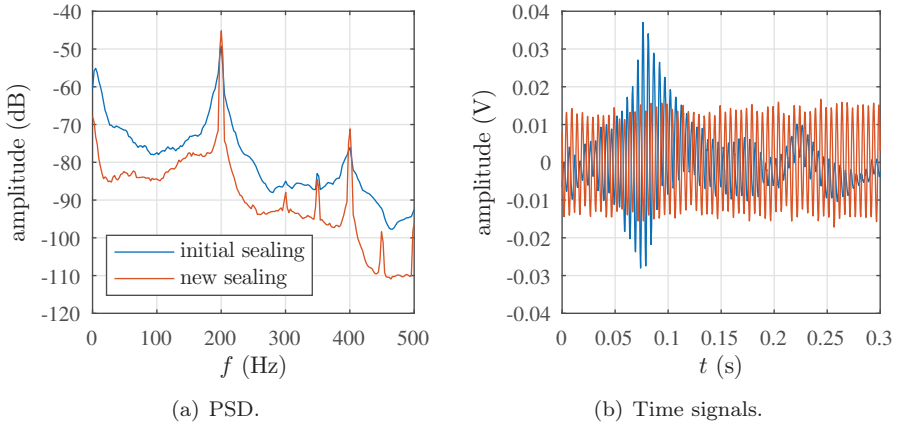


Figure 4.5.: Influence of the settling chamber sealing on the generation of artificial TS-waves ($f_{TS} = 200$ Hz). The error sensor signal $e(t)$ is acquired at $U_e = 12$ m/s.

signal $e(t)$ for the initial and the new sealing, which has been installed during pre-tests. The surface hot-wire sensor is not calibrated and only voltage fluctuations are shown. The new sealing improves the inflow quality, leading to a significantly reduced amplitude of the natural TS-waves, occurring besides the peak of the artificially generated TS-waves at 200 Hz. Natural TS-waves interfere with the artificial waves and lower the amplitude at 200 Hz. The spectrum of $e(t)$ with the initial sealing also shows a high amplitude for low frequency disturbances at $f \approx 10$ Hz, causing an amplitude modulation of the artificially generated TS-waves, cf. Fig. 4.5(b). The goal of the artificial TS-wave generation is an almost constant amplitude to increase the SNR for the phase-locked PIV measurements. The new sealing can reduce the low frequency fluctuations by 10 to 15 dB. The time signal of the error sensor presented in Fig. 4.5(b) exhibits significantly lower fluctuations of the amplitude after the new sealing has been installed.

Disturbance Production by Seeding Generation

The seeding generation in the settling chamber produces additional disturbances that influence the inflow quality and therefore also the receptivity process on the flat plate. This effect can be used in order to intentionally

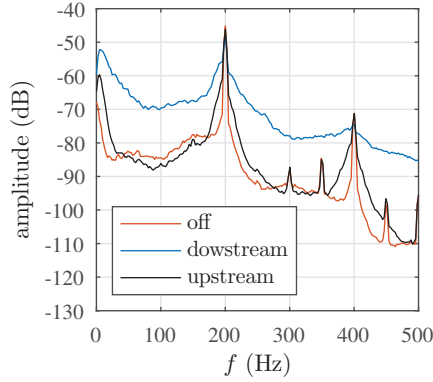
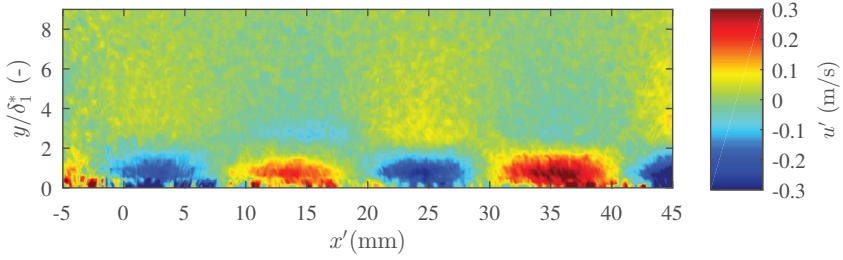


Figure 4.6.: Disturbance production by seeding, blown out in downstream or upstream direction. Spectra and time signals of the error-sensor signals $e(t)$ at $U_e = 12 \text{ m/s}$ with artificially generated TS-waves at $f_{\text{TS}} = 200 \text{ Hz}$.

modify the inflow turbulence spectra (Kendall (1990)). Here, the lower inflow quality causes an increased amplitude of the natural TS-waves, similar to the previously described improper sealing of the settling chamber wall. Figure 4.6 shows the PSD of the error-sensor signal for different configurations. The reference case (seeding off) shows a TS-wave “hump” in the band $150 \text{ Hz} < f < 220 \text{ Hz}$, which is $\approx 30 \text{ dB}$ lower in amplitude than the artificial TS-waves at 200 Hz . If the seeding is blown out in the downstream direction, the amplitude grows significantly and the natural waves are only $\approx 15 \text{ dB}$ smaller in amplitude, compared to the artificial TS-waves. If the seeding is blown out in the upstream direction, the amplitude of the natural TS-waves is lowered about 10 dB and the low frequency disturbances are also reduced significantly.

Two potential reasons for disturbance production in the settling chamber were identified and the inflow quality has been improved. A 2D even wavefront and TS-waves with a constant amplitude, generated at the time base of the PIV trigger system, are important for a fast convergence of the phase-locked measurements. The amplitude of the artificial TS-waves should be as high as possible for a high SNR, but the amplitude should only be of the order of 1% to $2\% U_e$ to assure linear behavior of the waves and to allow comparison with LST.



(a) Phase-averaged velocity field.

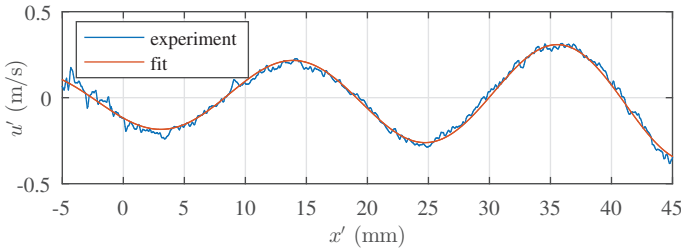
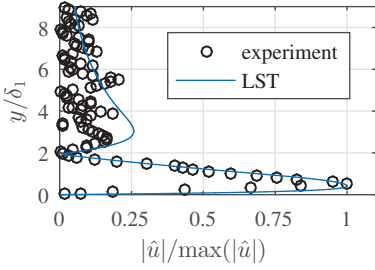

 (b) Experimental data, extracted from the velocity field (a) at $y/\delta_1^* = 0.67$ and data fit, according to equation (4.1).

Figure 4.7.: Phase-averaged velocity field and data fit of TS-waves with $f_{\text{TS}} = 250$ Hz at $U_e = 15$ m/s for FOV_2 at one (relative) phase angle.

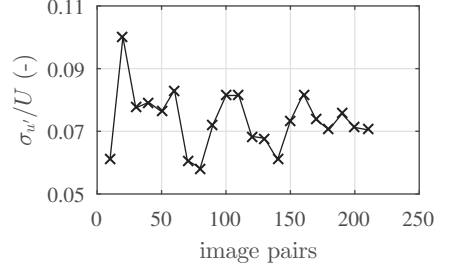
4.3.2. Characterisation of the Tollmien-Schlichting Waves

The disturbance source is capable of introducing single-frequency pressure fluctuations into the BL that cause velocity fluctuations, which travel downstream. In the following, these artificially generated disturbances are investigated by PIV and checked whether they have TS-wave character.

The phase-averaged measurements of the streamwise component u' of the artificial TS-wave with a frequency of 250 Hz is presented in Fig. 4.7(a) for one (relative) phase angle at $U_e = 15$ m/s. Two full wavelengths are covered by the PIV setup with two cameras. The wave-like pattern inside the boundary layer with an increasing amplitude in streamwise direction can be observed well. In addition, the counter-oscillating part of the wave above the BL is



(a) TS-wave profile at $x' = 24.9$ mm, extracted from Fig. 4.7(a). Every second data point is shown for clarity.



(b) Convergence of the normalized standard deviation of $u'(x' = 24.9$ mm, $y/\delta_1 = 0.9$).

Figure 4.8.: TS-wave profile and convergence diagram at one phase angle.

visible. An extract of the data at $y/\delta_1^* = 0.67$ is shown in Fig. 4.7(b) and equation (4.1) is fitted to it.

$$u'(x') = a \sin\left(\frac{2\pi}{\lambda_x} x' + b\right) e^{-k_{x,i} x'} + c \quad (4.1)$$

Equation (4.1) describes the spatial growth of the wave. The fitting parameters are the wavelength λ_x , the spatial growth rate $k_{x,i}$, the initial amplitude a , the phase offset b and the amplitude offset c . The determined parameters are $\lambda_x = 21.66$ mm and $k_{x,i} = -16.2 \cdot 10^{-3} \text{ 1/m}$, yielding a phase speed of $c_\omega = \lambda_x f_{\text{TS}} = 5.415 \text{ m/s}$. The measured values match well with the theoretical values calculated by LST at this position ($c_{\omega, \text{LST}} = 5.48 \text{ m/s}$).

Besides the spatial development of the TS-waves, the shape in wall-normal direction is important. Figure 4.8(a) shows the normalized amplitude (absolute value) of a TS-wave profile, extracted from Fig. 4.7(a) at $x' = 24.9$ mm. The measured and theoretically (LST) predicted profiles show a good agreement for $y/\delta_1 < 2$. Above, the data is noisier because the amplitude of the wave relative to the local velocity $u(y)$ is lower than inside the boundary layer.

In conclusion, the disturbance source generates pressure fluctuations that develop into velocity fluctuations with TS-wave character.

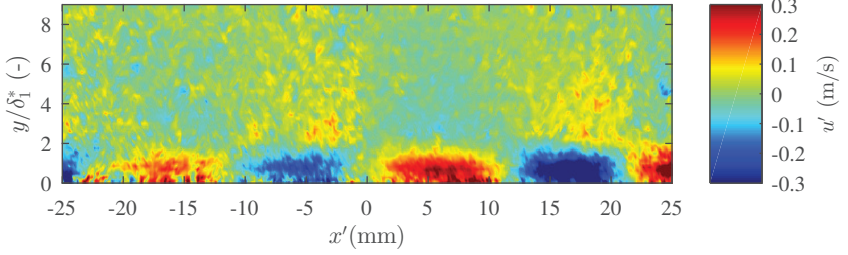
Statistical Convergence of the Phase-Locked PIV Measurements

Phase-averaging is necessary to measure TS-waves with PIV, since statistical velocity fluctuations and measurement noise overlay the artificially generated TS-waves that have an amplitude of $\approx 1\% U_e$. The number of required image pairs for convergence of the velocity fields can be estimated with a convergence diagram, cf. Fig. 4.8(b). The standard deviation of the streamwise velocity for one phase $\sigma_{u'}$ is averaged over 3×3 IAs at a position inside the boundary layer ($x' = 24.9$ mm, $y/\delta_1 = 0.8$). The result is normalized with the local mean velocity at this point. The normalized standard deviation $\sigma_{u'}/U$ converges for ≈ 200 image pairs. Compared to the measurements of Widmann et al. (2012) (1700 image pairs) and Amitay et al. (2016) (3000 image pairs), a significant lower number of image pairs is required. This is probably caused by the application of a high-speed PIV system. In addition, the improved inflow quality, causing a constant TS-wave amplitude over time, has a major impact on the SNR.

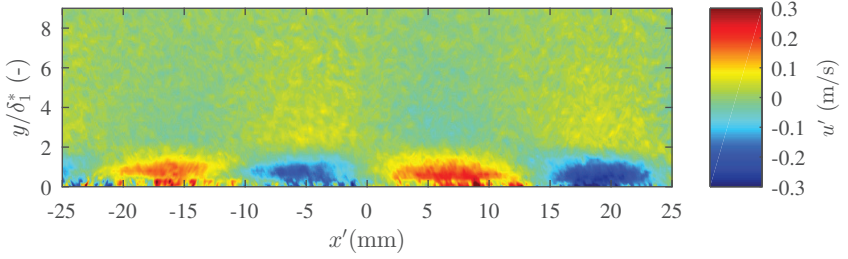
4.4. The Effect of Steady Plasma Actuator Forcing on Tollmien-Schlichting Waves

In this section the interaction between the incoming artificial TS-waves and steady PA forcing is investigated. The results of section 4.2 already showed that the PA has an impact on the mean velocity field. Figure 4.9(a) shows the artificial TS-waves ($f_{\text{TS}} = 250$ Hz) at $U_e = 15$ m/s as a reference case for FOV_1 . Figure 4.9(b) shows the case with steady PA forcing ($V_{\text{pp}} = 7$ kV) for the same relative phase angle. A slight damping of the amplitude downstream of the PA is visible, while the incoming wave upstream of the PA has a similar amplitude in both cases. More distinct is the increased wavelength downstream of the PA. This effect has already been measured by Widmann et al. (2013) with PIV and has been predicted by Duchmann et al. (2010) with LST computations. The measurements with different steady PA force amplitudes by Simon et al. (2015) also showed an increased phase speed c_ω for an increasing steady PA force, which corresponds to an increased wavelength.

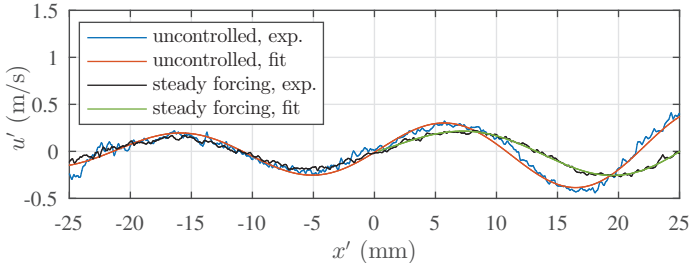
The qualitative observations can be confirmed with Fig. 4.9(c). It shows a horizontal extract of the data of the velocity fields in Fig. 4.9(a) and



(a) Phase-averaged velocity field, uncontrolled.



(b) Phase-averaged velocity field, controlled with steady PA force at $V_{pp} = 7$ kV.



(c) Experimental data, extracted from the velocity fields of (a) and (b) at $y/\delta_1^* = 0.52$ and data fit, according to equation (4.1).

Figure 4.9.: Impact of the steady PA force on the TS-waves ($f_{TS} = 250$ Hz) at $U_e = 15$ m/s, acquired for FOV_1 at one (relative) phase angle.

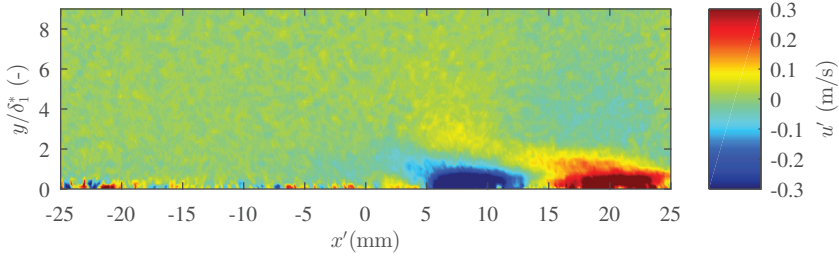


Figure 4.10.: Phase-averaged velocity field of u' at $U_e = 15$ m/s at one (relative) phase angle $\Phi_{TS} = 0$, acquired for FOV_1 . The PA force is modulated at $f_{TS} = 250$ Hz and generates counter-waves.

Fig. 4.9(b) at $y/\delta_1^* = 0.52$. Upstream of the PA both measured curves match well but downstream the wave is stretched. The approximation of the spatial wave development with equation (4.1) is presented in Fig. 4.9(c), too. The computed wavelength of the fit is $\lambda_x = 20.56$ mm for the uncontrolled case and $\lambda_x = 24.56$ mm for the controlled case with steady PA forcing. Because the TS-wave is only influenced downstream of the PA the curve is only fitted to the wavelength downstream of the PA.

4.5. Counter-waves Generated by the Plasma Actuator

In section 4.3 the TS-wave character of the velocity fluctuations generated by the disturbance source has been investigated and confirmed. The measurements presented in this section investigate the development of the counter-waves, generated by the PA. The actuator is operated with a driving signal frequency of $f_{PA} = 10$ kHz with an amplitude offset of $V_{pp} = 7$ kV. The modulation of the driving signal with $f_{TS} = 250$ Hz generates an unsteady PA force, cf. section 3.1. Figure 4.10 shows the phase-averaged velocity field of u' with unsteady PA forcing for one phase angle. The counter-waves are generated directly at the actuator, as also shown in Fig. A.1 for additional phase angles. The part of the wave pattern with a negative amplitude appears directly downstream of the PA. The PA force distribution (Fig. 3.1(a)) has a similar shape as the TS-wave profile (Fig. 4.8(a)). Hence, the generated

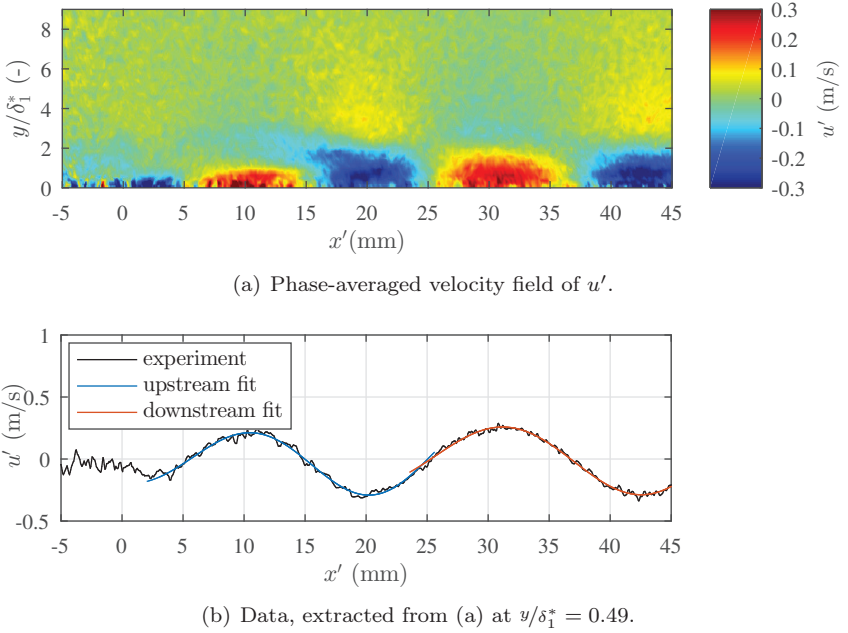


Figure 4.11.: Development of the counter-waves generated by the PA at $f_{TS} = 250$ Hz and $U_e = 15$ m/s for FOV_2 .

wave looks similar to a TS-wave but the tail of the wave pattern in Fig. 4.10 already indicates that the forced generation of the wave does not directly lead to a velocity fluctuation with TS-wave character. The tail of the wave-pattern has already been observed by Widmann (2010). He concluded that a higher steady PA force leads to a more pronounced tail.

Analyzing the TS-wave development with FOV_2 (Fig. 4.11(a)) gives better insight into the mechanisms of the counter-wave generation process. The waves grow in amplitude while traveling downstream, but also the wavelength changes. Figure 4.11(b) shows the extracted data from the phase-averaged velocity field at $y/\delta_1^* = 0.49$. Both cycles are approximated with a fit of equation (4.1). The initial wavelength of $\lambda_x = 19.52$ mm just behind the actuator increases to $\lambda_x = 22.69$ mm, which is slightly higher than in the uncontrolled case of $\lambda_x = 21.66$ mm, cf. Fig. 4.7(b). Only one wavelength (upstream fit) or even less (downstream fit) is available for the data fit and the

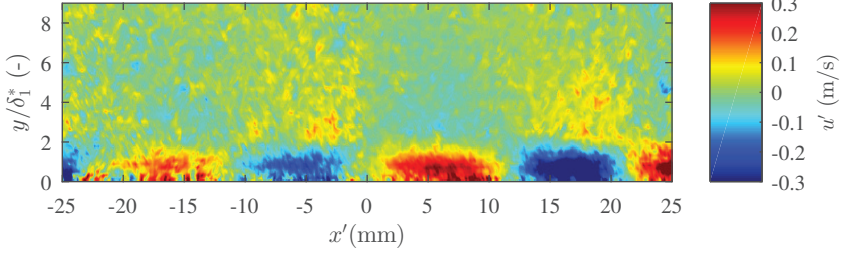
generated wave is not necessarily sinusoidal. Hence, the calculated wavelength λ_x is only an indicator rather than a reliable measurement.

It can be concluded that the PA does not generate TS-waves directly, but the disturbances develop while traveling downstream and change the wavelength. The impact of the changing wave properties for the AWC of TS-waves is discussed in the following section.

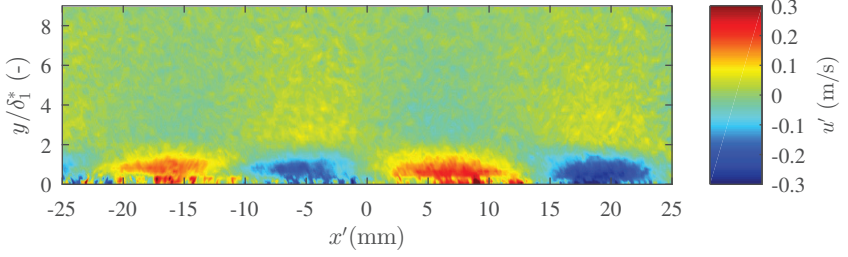
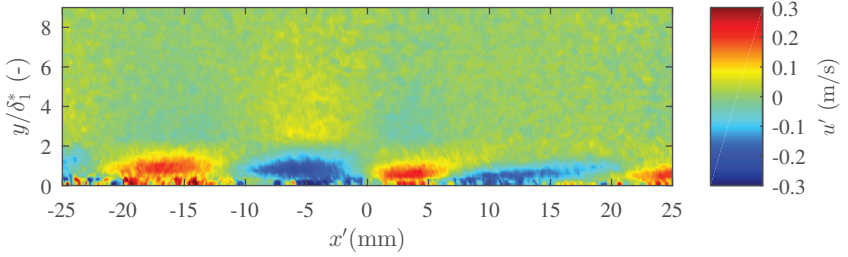
4.6. Active Cancellation of Tollmien-Schlichting Waves

The sections above deal with the characterisation of the base flow, the incoming waves and the velocity fluctuations generated by the PA itself. In the following, the DS and the PA are operated simultaneously to investigate the active wave cancellation. In contrast to the broad-band cancellation of TS-waves, presented in the following chapters, no real-time controller is necessary to compute the optimal counter-waves. Therefore, the amplitude and phase of the PA modulation (Fig. 3.1(b)) are adjusted manually to minimize the amplitude at the error sensor, mounted at $x' = 45$ mm. Both, PA control signal and DS signal are on the same time base and no phase lag occurs over time. As described in section 4.3, the artificially generated TS-waves do not have a constant amplitude over time due to disturbances of the inflow. A feed-forward fxLMS controller would lead to a better performance in terms of error-sensor signal reduction, but a continuous adaption of the phase and amplitude by the controller can lead to changes in the phase speed of the waves downstream of the PA. Therefore, manual setting is chosen.

Figure 4.12 shows the phase-averaged PIV measurements of the velocity fluctuations u' for three cases: uncontrolled TS-waves, steady PA forcing and AWC. Figure 4.12(c) denotes that the incoming TS-waves interfere with the counter-waves, generated by the PA. Nevertheless, the cancellation process does not happen directly at the actuator but further downstream. Only a part of the wave is attenuated because the generated counter-wave does not exactly match the incoming TS-wave. The counter-oscillating part of the wave above the BL is damped and the wave-like structure is not visible anymore. A more detailed explanation about the cancellation process can be obtained with the velocity fields measured downstream of the PA in FOV₂.

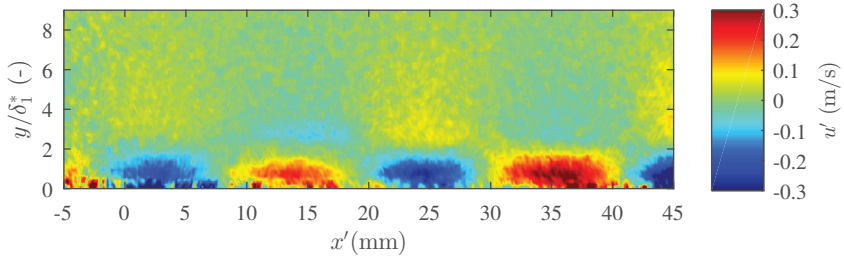


(a) Uncontrolled TS-waves.

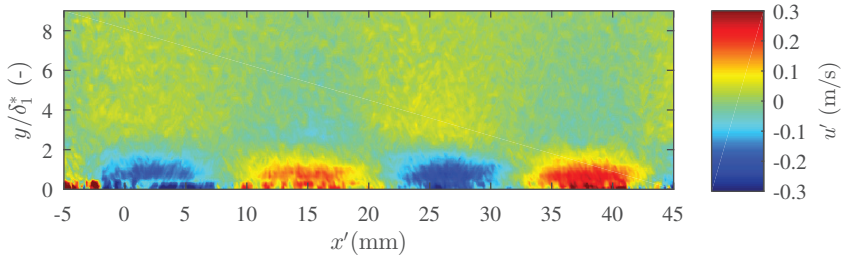

 (b) TS-waves, controlled by steady PA forcing at $V_{pp} = 7$ kV.


(c) Active wave cancellation.

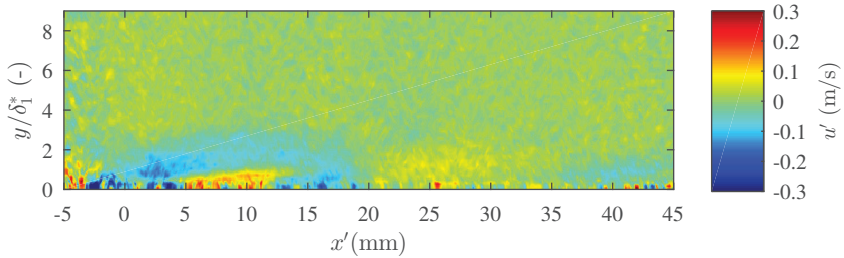
Figure 4.12.: Control of artificially generated TS-waves ($f_{TS} = 250$ Hz). Phase-averaged velocity fields at $U_e = 15$ m/s for FOV_1 .



(a) Uncontrolled TS-waves.



(b) TS-waves, controlled by steady PA forcing at $V_{pp} = 7$ kV.



(c) Active wave cancellation.

Figure 4.13.: Control of artificially generated TS-waves ($f_{TS} = 250$ Hz). Phase-averaged velocity fields at $U_e = 15$ m/s for FOV_2 .

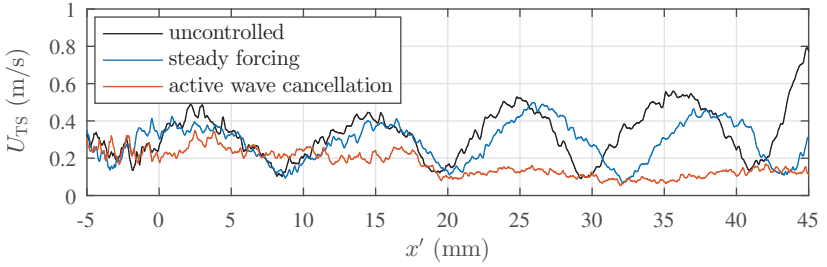


Figure 4.14.: Integral TS-wave amplitude U_{TS} for one phase angle, extracted from the velocity fields presented in Fig. 4.13.

The phase-averaged velocity fields presented in Fig. 4.13 allows the AWC between PA ($x' = 0$ mm) and the error sensor ($x' = 45$ mm) to be investigated. The contour plot in Fig. 4.13(c) shows successful attenuation of the TS-waves, but the amplitude starts to decrease further one wavelength downstream of the PA.

The distorted structure of the TS-waves downstream of the PA does not allow an evaluation of the control success by extracting data at a certain wall-normal position. The integral TS-wave amplitude

$$U_{TS}(x) = \frac{1}{\delta_1} \int_{y=0}^{\infty} |u'(x, y)| dy \quad (4.2)$$

integrates the velocity fluctuations in the wall-normal direction at one phase angle and is a robust measure for the development of the disturbances in the BL. Figure 4.14 shows U_{TS} for the three cases, already presented in Fig. 4.13. The steady forcing causes a stabilisation of the BL and avoids an exponential growth of the disturbances in the considered FOV₂. If the PA is operated in AWC mode, U_{TS} decreases for $0 \text{ mm} < x' < 20 \text{ mm}$ and stays at a rather constant level downstream. This finding confirms the hypothesis that the complete cancellation of the TS-waves does not occur directly at the PA, but some distance downstream. The PA generates counter-waves that do not match the wavelength of the incoming wave at first, but the cancellation happens one wavelength downstream. It should be noted that amplitude and phase of the counter-waves have been optimized based on the signal of the error sensor that is placed at $x' = 45$ mm - about two wavelengths downstream of the PA.

4.7. Conclusions

Phase-locked PIV measurements were conducted to obtain detailed insight into the active cancellation of TS-waves by superposition. The measured velocity fields show the interaction between the TS-waves and the PA force in AWC operation mode for the first time. It has been shown that a Blasius BL is a valid assumption for the mean flow field, measured by PIV on the flat plate. In addition, the artificially generated disturbances have TS-wave character and match well the prediction with LST. Great care was taken to improve the inflow quality, which results in a rather constant amplitude of the artificially generated TS-waves over time. In combination with the high-speed PIV measurement system this is the key for a fast convergence of the phase-averaged velocity fields. In comparison with previous experiments, the number of required image pairs was reduced by up to 80 %.

An important finding is that the modulated PA force ($f_{\text{TS}} = 250 \text{ Hz}$) does not generate counter-waves with TS-wave character immediately. The counter-waves travel downstream and change their shape and wavelength. This is also the reason why the wave cancellation of the incoming TS-waves does not occur directly at the actuator, but one wavelength downstream. The TS-wave amplitude is successfully attenuated directly upstream of the error sensor, which has been used to optimize phase and amplitude of the counter-wave.

The processes in the boundary layer during AWC have been thoroughly studied by means of PIV with artificially generated single-frequency TS-waves. Natural TS-waves occur over an entire frequency band and feed-forward control algorithms are introduced in the next chapter to perform AWC in a more realistic case with broad-band disturbances.

5. Stability Impacts on Static and Adaptive Control Algorithms

This chapter discusses the robustness of a static LQG control algorithm compared to an adaptive fxLMS algorithm in a wind-tunnel experiment on a flat plate. Because the LQG controller is based on DNS computations, the base flow properties and the DNS model of the flow are discussed first in section 5.1. In addition, the sensor calibration as well as the plasma actuator model required for the DNS are discussed. The digital FIR filter \mathbf{w} used to compute the control signal of the actuator, based on the upstream reference sensor (feedforward), is also called a compensator. A comparison of the previously computed static compensator of the LQG controller and the online adapted fxLMS controller is drawn in section 5.2. It is conducted by introducing a performance indicator that allows comparing the influence of varying inflow conditions on the controller performance with static and adaptive compensators. Section 5.3 investigates the controller stability of the adaptive fxLMS controller in more detail and presents a general method to predict the robustness of the control algorithm. Finally, methods to adapt the secondary path model for the fxLMS controller online are proposed and experimentally confirmed in section 5.4. This enables stable controller operation over a wide range of wind-tunnel speeds, based on a previously recorded calibration of the system. Conclusions for this chapter are given in section 5.5.

5.1. Base Flow on the Flat Plate

The experimental setup used for the investigations described in the following has been introduced in section 3.2. Hot-wire boundary-layer measurements have been carried out to characterize the flow for the reference case at a wind-tunnel speed of $U_{WT} = 12 \text{ m/s}$, which corresponds to an outer velocity of the flat-plate boundary layer of $U_e = 14 \text{ m/s}$ due to blockage. The

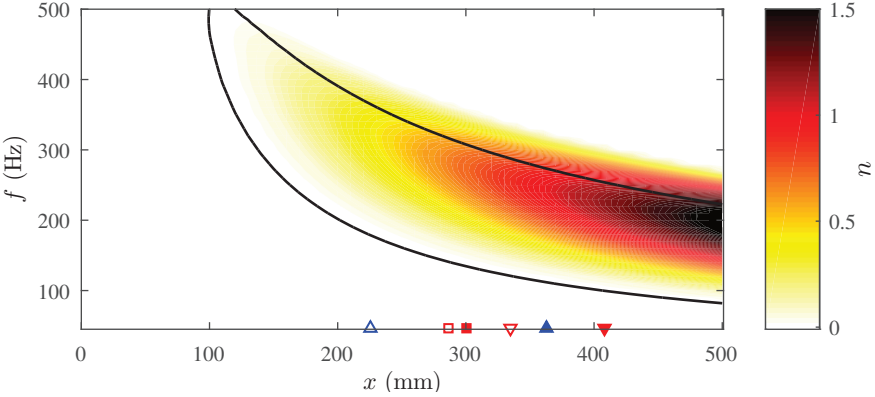


Figure 5.1.: Neutral stability curve ($k_{x,i} = 0$, black solid line) and n -factor contours for zero pressure gradient and $U_{WT} = 12 \text{ m/s}$ ($U_e = 14 \text{ m/s}$), spanwise wavenumber $k_z = 0$. The symbols indicate the actuators and sensors, cf. Fig. 3.3.

linear stability theory (LST) calculations for the reference case $U_e = 14 \text{ m/s}$ ($\nu = 15.96 \cdot 10^{-6} \text{ m}^2/\text{s}$) are shown in Fig. 5.1, assuming a 2D wavefront (spanwise wavenumber $k_z = 0$) and a Blasius boundary layer. All stability calculations in this section have been performed with a code provided by Reeh (2014). The low amplification scenario is well suited for artificial TS-wave generation. A 2D wavefront is generated by the disturbance source, dominating the naturally occurring waves that are present in the boundary layer. This enables a systematic investigation on the controller stability. The zero-pressure gradient laminar boundary-layer flow allows comparison with LST. A measurement of the TS-wave dominated transition is not within the scope of this investigation, as it would not naturally occur on the wind-tunnel model if transition happens for $N_{\max} \approx 9$, cf. section 2.1.

The boundary-layer profiles, measured at the positions $x_{p_1} = 287 \text{ mm}$ (\square), $x_r = 335 \text{ mm}$ (∇) and $x_e = 408 \text{ mm}$ (\blacktriangledown), are shown in Fig. 5.2. Three profiles are measured next to the surface hot-wires p_1 , r and e . The signals at each measurement point have been acquired at 10 kHz sampling rate for 10 s. The good agreement between the theoretical and the experimental results confirms the applicability of linear stability theory. The H_{12} values stated below each profile are close to the theoretical value of a Blasius solution ($H_{12} = 2.59$).

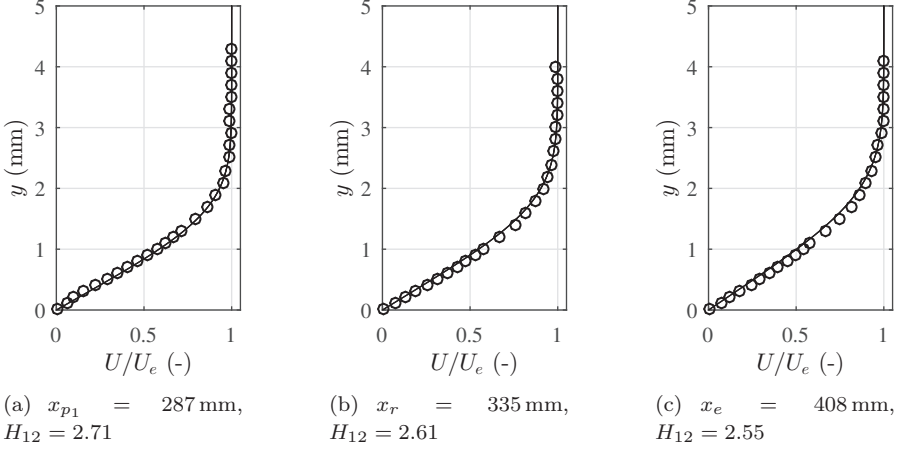
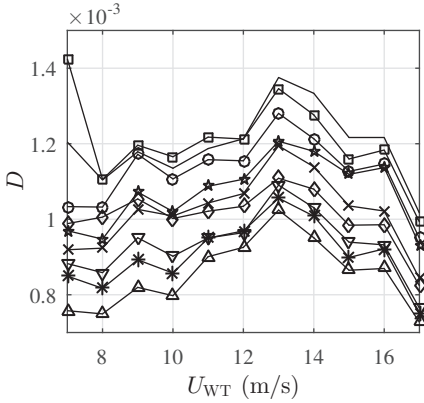


Figure 5.2.: Normalized measured boundary-layer profiles (o) and corresponding Blasius profile (solid line) at x_{p1} , x_r and x_e at reference speed $U_{WT} = 12 \text{ m/s}$ ($U_e = 14 \text{ m/s}$). The shape factor H_{12} is stated below each velocity profile.

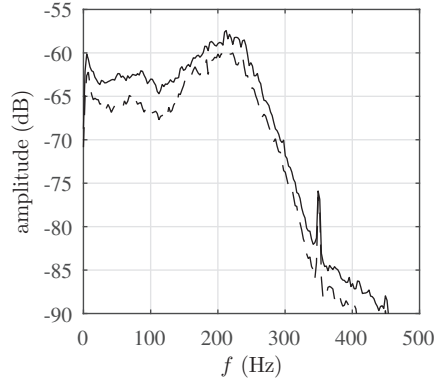
5.1.1. Boundary-Layer Receptivity

Most of the following active wave cancellation experiments are conducted with broad-band disturbances, introduced into the boundary layer by a low-pass filtered white-noise (WN) input signal for the disturbance source loudspeakers. The WN signal is generated with a sample rate of 5 kHz. Phase-averaged measurements allow to monitor the TS-wave amplitude of single-frequency disturbances only. Therefore the RMS value of the (un-calibrated) reference-sensor signal $r(t)$ is used as a measure of the disturbance amplitude. A single-frequency (200 Hz) disturbance with an amplitude of $1\%U_e$ at $U_{WT} = 12 \text{ m/s}$ yields a RMS value of $r(t)$ of $\text{RMS}(r(t)_{200\text{Hz}, 12 \text{ m/s}}) = 0.0174 \text{ V}$. For the white noise excitation the RMS value is lowered to $\text{RMS}(r(t)_{\text{WN}, 12 \text{ m/s}}) = 0.0124 \text{ V}$ in order to avoid non-linear effects. An attempt was made to keep the ratio D (5.1) of the $\text{RMS}(r(t)_{\text{WN}, U_{WT}})$ to the wind-tunnel speed U_{WT} constant for all wind-tunnel speeds.

$$D = \frac{\text{RMS}(r(t)_{\text{WN}, U_{WT}})}{U_{WT}} \quad (5.1)$$



(a) Ratio D between $\text{RMS}(r(t))$ and U_{WT} . Different symbols stand for different test runs.



(b) PSD of $r(t)$ at $U_{WT} = 12 \text{ m/s}$. The graph shows the most amplified and lowest amplified cases for different test runs.

Figure 5.3.: Boundary-layer receptivity with artificially generated broad-band TS-wave disturbances for different test runs.

The special construction of the wind-tunnel does not allow for perfectly repeatable experiments concerning the receptivity of the boundary layer. The open-circuit tunnel sucks air from outside the building and therefore provides varying conditions concerning humidity, temperature and inflow turbulence. The disturbance source amplitude for each wind-tunnel speed U_{WT} has only been calibrated once to achieve an almost constant ratio D for the considered velocity range. The curve for the calibration test run in Fig. 5.3(a) is marked with a diamond symbol (\diamond). It shows the parameter D for different wind-tunnel speeds U_{WT} . The change in receptivity becomes obvious through the vertical displacement of the curves for different runs but the same calibrated disturbance source amplitude. The deviation of the curves varies about $\pm 10\%$ for one test series, if the borderline cases $U_{WT} = 7 \text{ m/s}$ and $U_{WT} = 17 \text{ m/s}$ are not taken into account. Each curve is recorded in a short time frame of several minutes while the RMS is calculated for a data set of 20 s at each wind-tunnel speed.

The power-spectral density of the reference-sensor signal $r(t)$ at a wind-tunnel speed of $U_{WT} = 12 \text{ m/s}$ with a constant disturbance source amplitude

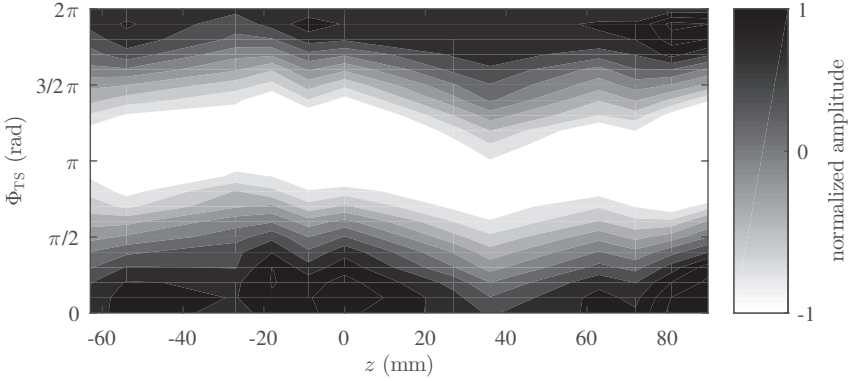


Figure 5.4.: Phase-averaged and normalized microphone signals for an 2D even wavefront TS-wave with $f_{TS} = 200$ Hz.

is shown in Fig. 5.3(b) for two measurements. The narrow peak 350 Hz in Fig. 5.3(b) occurs because of electromagnetic interference caused by the wind-tunnel motor power supply. The curves of the different test runs show a rise of the amplitude for all frequencies and confirms the assumption of a change in boundary-layer receptivity.

As mentioned earlier, an even 2D wavefront of the TS-wave disturbances is required for the investigations presented in this chapter because a SISO system with only one actuator (2D assumption in spanwise direction) is applied. For the following investigations the disturbance source generated TS-waves with a frequency of 200 Hz, which is within the most amplified frequencies as indicated in the stability curve (Fig. 5.1) and visible in the TS-wave hump of the measured spectra in Fig. 5.3(b).

Microphones, mounted below the surface of the flat plate and mounted in spanwise direction between reference sensor and PA, deliver reliable information about the phase angle of the artificially generated disturbances, cf. section 3.2. The microphone signals, sampled at $f_S = 4$ kHz and phase averaged over 2000 cycles, are shown in Fig. 5.4. The measurement results indicate that a 2D even wavefront assumption is valid for the single frequency disturbance case. Therefore it is also assumed to be valid for the white noise excitation.

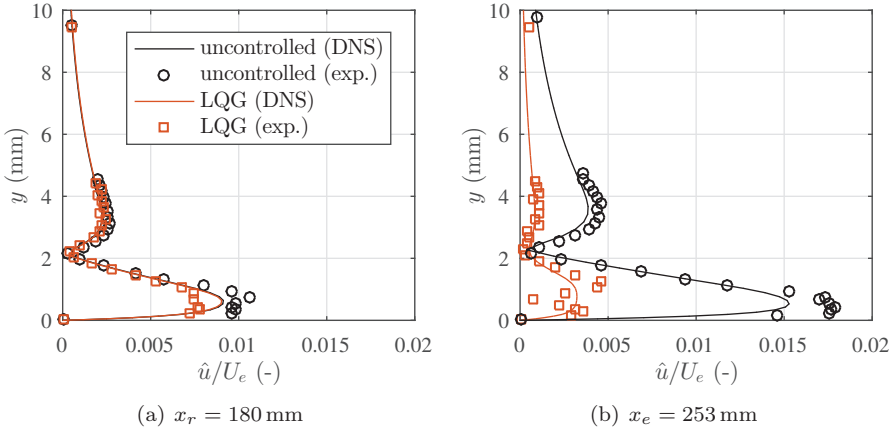


Figure 5.5.: Normalized TS-wave amplitude at two different streamwise positions, upstream and downstream of the PA for the controlled (LQG) and uncontrolled case at $U_{WT} = 12$ m/s. The TS-waves are generated artificially at $f_{TS} = 200$ Hz.

Phase averaging of the boundary-layer hot-wire signals ($f_S = 10$ kHz) allows the measurement of the single-frequency TS-waves. The resulting measured waveforms are averaged over 2000 samples for each of the 50 phase angles. The measured amplitude of the TS-wave is plotted as a black circle in Fig. 5.5. The measured maximum amplitude is $\approx 1\% U_e$ at the reference sensor position for the presented measurement.

5.1.2. A Direct Numerical Simulation Model of the Flow

The DNS calculations have been performed by the cooperation partner Nicolò Fabbiane. Therefore the information about the DNS model of the flow are mainly taken from the joint publication Fabbiane et al. (2015).

The numerical simulations are used to compute the flow over the flat plate and provide a model for the LQG controller design. As shown in the previous paragraph, the generated disturbances are sufficiently small not to trigger nonlinear phenomena. Therefore, the linearized Navier-Stokes (NS) equations in a zero-pressure gradient boundary-layer flow are considered to describe the temporal evolution of the disturbances. A parameter fitting procedure is

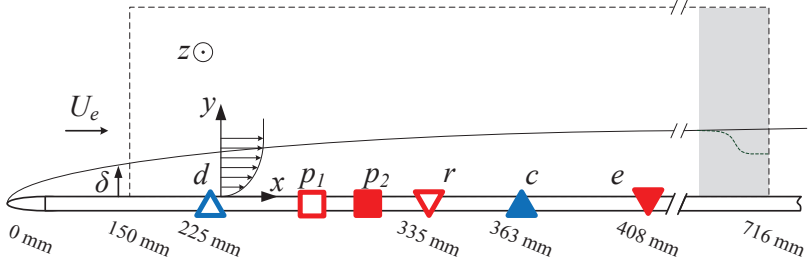


Figure 5.6.: Flat plate setup; the computational domain used for the DNS is marked with a dashed line.

used to match the DNS solution to the measured inflow conditions: a flow velocity of $U_e = 14 \text{ m/s}$ and a displacement thickness of $\delta_1^* = 0.748 \text{ mm}$ is set at the beginning of the computational domain, indicated with a dashed line in Fig. 5.6. The domain starts at $x = 150 \text{ mm}$ and it extends $750 \delta_1$ in the streamwise direction and $30 \delta_1$ in the wall-normal direction. In the last part of the domain (grey area in Fig. 5.6), a fringe region enforces the periodicity along the streamwise direction (Nordström et al. (1999)).

The Reynolds number is $Re_1 = \frac{U_e \delta_1}{\nu} = 656$ at the upstream border of the computational domain. The DNS simulations are performed with a pseudo-spectral DNS code (Chevalier et al. (2007)). Fourier expansion over $N_x = 768$ modes is used to approximate the solution along the streamwise direction, while Chebyshev expansion is used in the wall-normal direction on $N_y = 101$ Gauss-Lobatto collocation points.

The disturbance source d and the PA c are modelled by volume forcings. Each forcing term is decomposed into a constant spatial shape and a time-dependent part (i.e. the input signal). The forcing shape of the disturbance source is a synthetic vortex, localized at x_d (Bagheri et al. (2009)). The plasma actuator is modelled by a distributed streamwise forcing, according to Kriegseis et al. (2013b). Because the forcing shape depends on the actuator state, it is linearized around $V_{pp} = 7 \text{ kV}$. The surface hot-wire sensors are modelled as pointwise measurements of the skin-friction fluctuations.

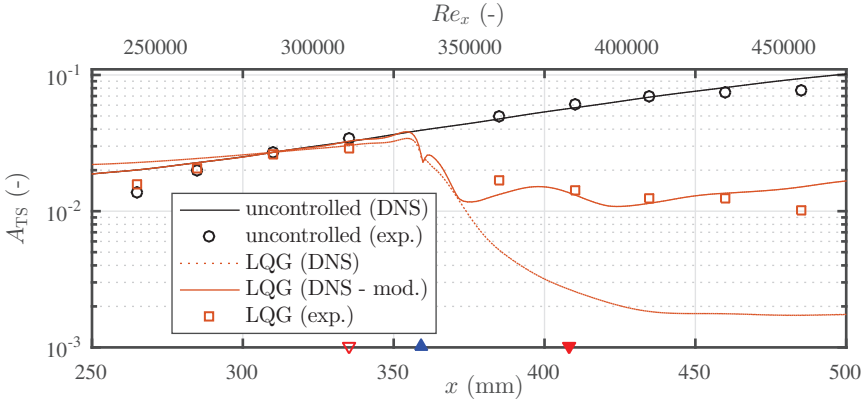


Figure 5.7.: Integral TS-wave amplitude A_{TS} as a function of the streamwise position for the controlled and uncontrolled case, obtained experimentally and with DNS. The TS-waves are generated by the disturbance source at 200 Hz.

TS-wave Disturbance Amplitude Growth

The exemplarily shown TS-wave amplitudes for a 2D disturbance in Fig. 5.5 allow the calculation of an integral value of the TS-wave amplitude that is a robust parameter for experimental data:

$$A_{TS}(x) = \frac{1}{\delta_1} \int_{y=0}^{\infty} \frac{|\hat{u}(x, y, f_{TS})|}{U_e} dy. \quad (5.2)$$

A calibration of surface bounded sensors like wall shear stress balances, hot-films or surface hot-wires is challenging. The measurements of A_{TS} in direct vicinity of the reference and error sensor for different disturbance source amplitudes allow a calibration of the surface hot-wires. A linear relation between sensor signal amplitude and A_{TS} at 200 Hz can be found and temperature correction (Nitsche and Brunn (2006)) is applied to compensate the effect of changing inflow temperature on the thermal measurement principle of the sensors. The development of A_{TS} (uncontrolled case) in streamwise direction is presented in Fig. 5.7. It shows a good agreement between the hot-wire measurements (black circles) and the DNS computations (black solid line) in terms of amplitude growth for the single frequency disturbance at 200 Hz.

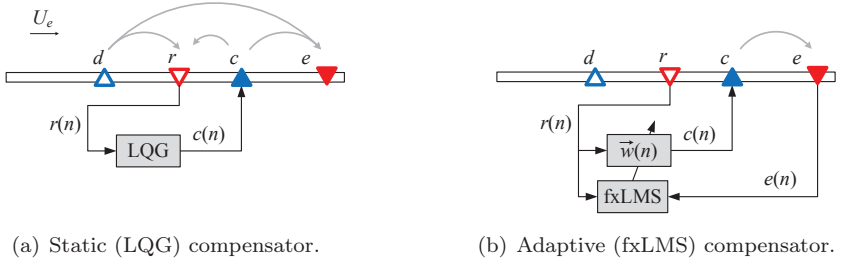


Figure 5.8.: Signal paths for static and adaptive compensator kernels. The black arrows indicate the signal path during controller operation while the grey arrows indicate the paths that have to be modeled/identified before.

5.2. Active Wave Cancellation with Static and Adaptive Control Algorithms

Two different kind of compensators, static and adaptive compensators are compared in the following. The compensator kernel (section 2.2.2) is the part of the controller that is modeled by a FIR filter \mathbf{w} in order to compute the required control signal for the actuator. The adaptive fxLMS algorithm adapts the compensator kernel \mathbf{w} online while the static LQG compensator kernel is previously computed based on DNS computations. Therefore the LQG compensator is optimal and delivers best performance from the moment it is switched on. The adaption of the fxLMS compensator kernel based on the error sensor signals requires some time - about 20s for this case. The compensator is sub-optimal but it can adapt to changes in the control path up to certain limits as it is shown in the following. The control success of the model-based LQG is only dependent on a previously modeled flow behavior computed by DNS. For a better comparison the schemata in Fig. 5.8 show the previously computed/identified transfer paths (grey arrows) and the signals required during controller operation (black arrows). This again shows that more information about the flow is required for the static compensator while the adaptive compensator requires an additional error sensor signal during operation. Both algorithms are feed forward algorithms, which is favourable for controller stability (Belson et al. (2013); Fabbiane et al. (2014)).

The control success of the fxLMS controller depends on a good model \hat{H}_{ec} of the boundary-layers transmission behavior between plasma actuator c and error sensor e . All experiments in this document have been conducted in a boundary layer with almost zero pressure gradient, therefore \hat{H}_{ec} only changes with U_{WT} as the sensor and actuator positions are fixed. Figure 2.7(b) shows the impulse response of the secondary path \hat{H}_{ec} , modeled by a finite impulse response (FIR) filter with $M = 256$ filter coefficients. It is obtained by operating the high voltage generator with an input voltage ζ , consisting of a DC offset voltage and an AC PRBS (pseudo random binary signal), resulting in a broad-band modulation of the plasma-actuator body force (Fig. 3.1(b)). This body-force causes random velocity fluctuations in streamwise direction, filtered by the boundary layer while propagating downstream due to the band-pass character of the boundary-layer flow. In the TS-wave bandpass region, a coherence of $\gamma^2 \approx 0.95$ indicates an almost linear behaviour of the PA as a flow control actuator (Simon et al. (2015)).

AWC of Single-Frequency Disturbances

The ability of the LQG algorithm to attenuate single-frequency 200 Hz TS-wave disturbances is tested in order to compare the development of the disturbance amplitude between simulation and experiment. The orange squares in Fig. 5.7 show that A_{TS} is attenuated successfully during the experiment, if the LQG controller is switched on. The corresponding DNS results (dotted line) show a more significant drop of A_{TS} downstream of the PA (\blacktriangle). The difference in controller performance can be explained by the steady PA force, caused by the PA supply voltage offset of V_{pp} . This is not implemented in the DNS model of the flow, therefore it is not correct anymore due to the local acceleration of the TS-wave (Duchmann et al. (2010)). The solid orange line in Fig. 5.7 shows a modified version of the DNS computation, taking the steady force offset into account. The modified DNS result fits now well to the experimental results. It can be concluded, that the DNS model-based LQG controller works but a relatively high effort is required in order to match the base flow and obtain a good model of the flow.

A closer look at the measured TS-wave profiles for the LQG operation in Fig. 5.5 shows again a good agreement between DNS and experiment. The profiles, measured at the reference and error sensor positions, proof the

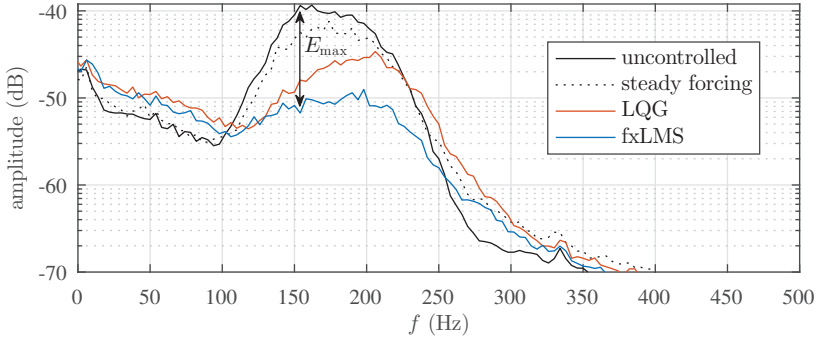


Figure 5.9.: Time-averaged power-spectral density of the measured error sensor signal $e(t)$. The 2D TS-wave disturbances are excited by a white-noise signal at $U_{WT} = 12 \text{ m/s}$. The steady operating voltage offset is $V_{pp} = 7 \text{ kV}$.

successful attenuation of the incoming wave. The profile at x_r with LQG controller operation (orange squares) indicates a slightly lower amplitude of the wave compared to the uncontrolled case. This is due to changes in receptivity and not caused by the actuator itself. The profile measured downstream of the actuator during controller operation shows a successful attenuation of the amplitude but also a double peak structure in the lower part ($y \approx 1 \text{ mm}$) where the maximum forcing of the PA occurs (Kriegseis et al. (2013b)). This double peak structure is less pronounced as the wave travels downstream.

AWC of Broad-Band Disturbances

The AWC experiments presented in the following are conducted with an even wavefront but WN excitation. Figure 5.9 shows the power spectral density of the error sensor signal $e(t)$ for the uncontrolled and controlled cases at $U_{WT} = 12 \text{ m/s}$. The TS-wave hump, which reaches approx. from 100 Hz to 250 Hz, is clearly visible and agrees well with the stability curve (Fig. 5.1). If the PA is operated continuously (steady forcing), the amplitude is lowered up to 3 dB due to boundary-layer stabilisation. The naturally occurring disturbances in the TS-wave band are 15 dB smaller and can therefore be neglected.

The LQG controller has been proven to effectively attenuate single frequency disturbances. In the following both approaches, static LQG and adaptive fxLMS, are tested for more realistic broad-band disturbances with an

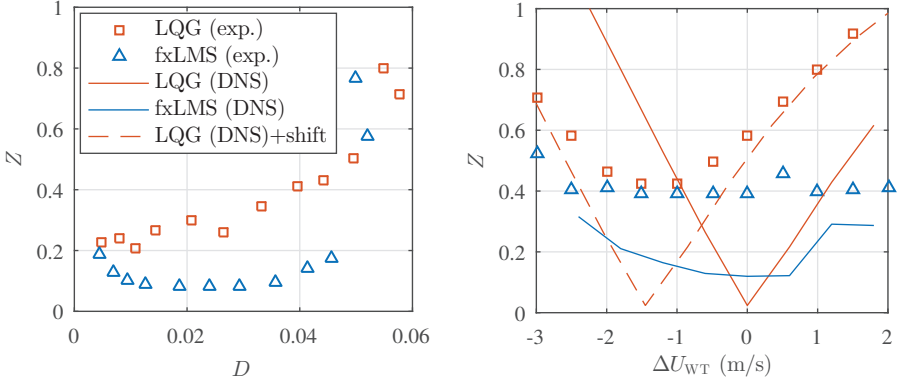
even 2D wavefront at $U_{WT} = 12 \text{ m/s}$. During fxLMS controller operation the TS-wave hump, reaching from 100 Hz to 250 Hz, is almost completely attenuated. In average, an amplitude reduction of $\approx 10 \text{ dB}$ is reached and a maximum reduction of $E_{\max} = 15 \text{ dB}$ is achieved. The static LQG controller also successfully damps the incoming waves but performs slightly worse. It is noticeable that it performs equally well for frequencies of $f \approx 120 \text{ Hz}$ but worse in the range of 150 Hz to 250 Hz. Therefore, a mismatch between the DNS model of the flow and the current state in the experiment can be assumed and is discussed later. In addition to the successful attenuation of the disturbances in the TS-wave frequency range, disturbances below and above are slightly amplified during controller operation. Because these disturbances are naturally attenuated by the stability properties of the BL the slight amplification is not relevant. More relevant is the robustness of the control algorithms against incorrect models of the BL transmission behavior and therefore unintentional amplification of disturbances in the TS-wave band due to an unstable controller behavior, discussed in the following section. The stability of the controller and performance are investigated for the static and adaptive compensator approaches. Two influencing parameters are discussed: The effect of the disturbance amplitude, up to a non-linear behavior and a change of U_{WT} .

5.3. Influences on the Controller Stability

The influences of varying inflow conditions on the controller stability of static LQG and the adaptive fxLMS algorithm are discussed first in section 5.3.1. Based on these findings, the stability of the fxLMS algorithm is investigated in terms of phase-angle dependency of the identified secondary path model and the current flow state in section 5.3.2.

5.3.1. Compensators under Varying Inflow Conditions

In the following, the differences between controller operation at design point and under deviating working conditions are discussed. Both, LQG and fxLMS are based on linear control laws. If the amplitude of disturbances is small, i. e. below $1\%U_e$, they can be treated as linear. The effect of increasing TS-wave amplitude on the controller performance is presented in Fig. 5.10(a). The



(a) Effect of the disturbance amplitude ratio D on the performance indicator Z with disturbances (200 Hz) at $U_{WT} = 12$ m/s.

(b) Effect of a change in wind-tunnel speed on Z ($\Delta U_{WT} = 0$ m/s $\equiv U_{WT} = 12$ m/s) with broad-band disturbances.

Figure 5.10.: Impact factors in the control algorithm performance indicator Z .

ratio D (5.1) is increased continuously until the controller shows an unstable behavior. The performance indicator

$$Z = \frac{\text{RMS}(e_{\text{ctr}}(t))}{\text{RMS}(e_{\text{unctr}}(t))} \quad (5.3)$$

is defined by the ratio of the RMS of the error sensor signal $e(t)$ for the controlled case and the uncontrolled case. Only cases for $Z < 1$, which corresponds to a signal reduction with controller operation, are presented in Fig. 5.10(a). For $Z > 1$ the controller is unstable and the results are not presented. The performance Z of the LQG controller gradually decreases for higher D whereas the fxLMS control performance stays at a rather constant level up to $D = 0.05$, where Z experiences an abrupt breakdown. Both, static (LQG) and adaptive (fxLMS) compensator kernels are unstable at about the same value of D .

The effect of a changing flow speed on the controller stability is shown in Fig. 5.10(b). The reference wind-tunnel speed of $U_{WT} = 12$ m/s is varied by ΔU_{WT} . The experimental (exp.) and numerical (DNS) results show that the LQG algorithm is sensitive to small variations of U_{WT} while the fxLMS controller performance stays at almost the same level for all investigated veloc-

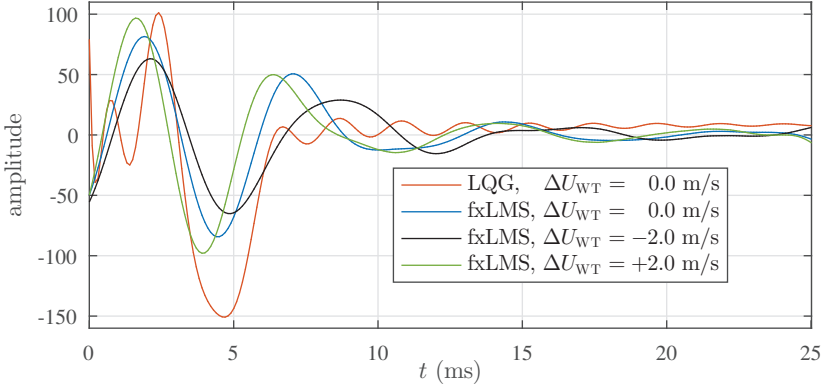


Figure 5.11.: Compensator kernels \mathbf{w} (exp.) for different wind-tunnel speeds but designed for the reference case $U_{WT} = 12 \text{ m/s}$ ($\Delta U_{WT} = 0 \text{ m/s}$).

ities. The change in velocity implies a change in Re and therefore also group speed c_g of the incoming waves. A closer look at the compensator kernels in Fig. 5.11 shows the reason for the observed behavior: The static LQG kernel (solid orange line) stays the same while the fxLMS algorithm adapts to the changed inflow parameters (blue lines). An increased flow velocity implies a higher amplification, therefore the amplitude of the FIR filter maxima is higher ($\Delta U_{WT} = +2 \text{ m/s}$). For the case $\Delta U_{WT} = -2 \text{ m/s}$ the maxima become lower in amplitude and the FIR filter is stretched because of a decreasing group speed c_g .

An interesting fact is that Z increases almost linearly with changing flow speed for the LQG case in Fig. 5.10(b), but the values of the experimental points and the DNS computation do not match. If the design point of the controller is changed to $\Delta U_{WT} = -1.5 \text{ m/s}$, numerical and experimental result match well. To underline the linear behavior, the cancellation process is modeled in (5.4) by a superposition of an incoming disturbance $e_d(t)$ and a counter wave $e_c(t)$ generated by the PA.

$$e(t) = e_d(t) + e_c(t) = \hat{q} \sin(\omega t + \Delta\Phi) - \hat{q} \sin(\omega t) \quad (5.4)$$

The main effect of ΔU_{WT} is the resulting change in group speed c_g that modifies the phase-angle shift $\Delta\Phi$. From (5.4) it can be observed that the performance of the controller is lowered linearly for small values of $\Delta\Phi$, as also

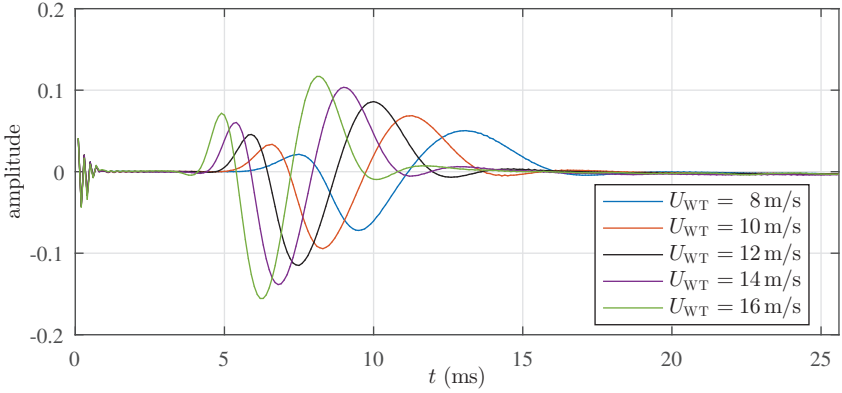


Figure 5.12.: Impulse response (exp.) of the secondary path model \hat{H}_{ec} at different U_{WT} .

observed by Pätzold (2013). In the experiment the performance of the LQG controller is limited to $Z \approx 0.4$, probably due to natural disturbances and sensor noise. The fxLMS controller approaches the same performance limit but the controller performance stays the same for the whole investigated range of U_{WT} . Here, it can also be noted, that the fxLMS algorithm has a static part, which is the secondary path model \hat{H}_{ec} . Even if \hat{H}_{ec} is identified before each set of measurements, the physical path H_{ec} can change between different runs. The changing performance of the fxLMS controller is more distinct for the DNS computations, indicated by a solid blue line in Fig. 5.10(b): The performance decreases slightly, if the wind-tunnel speed deviates from $U_{WT} = 12 \text{ m/s}$.

It can be concluded that the optimal static LQG compensator is theoretically of advantage in comparison to the suboptimal fxLMS. But the fxLMS is able to adapt to non-linearities in disturbance amplitude as well as to slight changes of the wind-tunnel speed while the LQG performance decreases from the first deviation of the previously computed model.

Despite its ability to adapt, the fxLMS cannot compensate larger deviations of the static secondary path model \hat{H}_{ec} . Figure 5.12 shows \hat{H}_{ec} for different U_{WT} . The impulse-response shape changes as the bandpass of the amplified disturbance frequencies shifts to higher frequencies, if U_{WT} is increased. The shape of the impulse-response model mainly relies on the change of the group

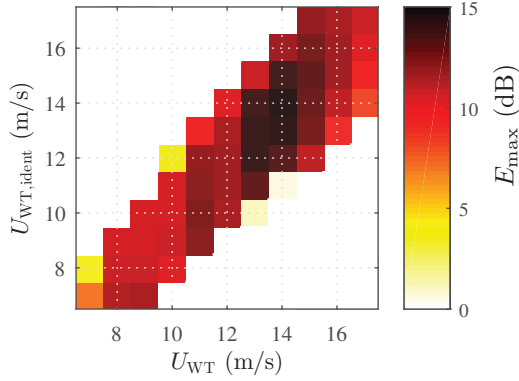


Figure 5.13.: Maximum error sensor signal reduction E_{\max} for fxLMS controller operation (experiment) with constant secondary path model, identified at $U_{\text{WT},\text{ident}}$ and controller performance for different flow speeds U_{WT} .

speed c_g and the amplification of the disturbances in the boundary layer. The impact of this significant changes in H_{ec} is investigated in detail in the following section.

5.3.2. Phase-Angle Dependent Stability of the fxLMS Algorithm

This section discusses the robustness of the control algorithm against changes in U_{WT} based on the investigation on the boundary-layer transmission behavior shown above. An example for TS-wave attenuation at $U_{\text{WT}} = 12 \text{ m/s}$ is shown in Fig. 5.9. The maximum disturbance attenuation $E_{\max} = 15 \text{ dB}$ is achieved in a small band at $f = 150 \text{ Hz}$, representing the most amplified TS-wave frequencies.

If the fxLMS control algorithm is operated off the design point, at which the model of the secondary path \hat{H}_{ec} has been identified, the controller can become unstable due to the change of the transmission behavior of the boundary-layer flow (cf. section 5.3.1). Figure 5.13 shows the maximal achieved reduction of the disturbance E_{\max} as a function of the wind-tunnel speed during the experiment U_{WT} and the speed $U_{\text{WT},\text{ident}}$ where the secondary path model $\hat{H}_{ec,U_{\text{WT}}}$ is identified. The investigation of the stability of the controller is conducted

for different wind-tunnel speeds in steps of $\Delta U_{\text{WT}} = 1 \text{ m/s}$. The white areas represent unstable controller operation (no cancellation or even amplification). Because of the unstable behavior of the controller, the measurement has been stopped to prevent actuator damage and therefore no representative data is available for these operation points. All colored blocks show measured cases and their corresponding reduction of the error sensor signal E_{max} . Red color indicates a stable controller operation and successful TS-wave attenuation whereas yellow blocks indicate a marginally stable controller with almost negligible attenuation. The controller can successfully attenuate TS-waves in the range of $11 \text{ m/s} < U_{\text{WT}} < 15 \text{ m/s}$ with a secondary path model, identified at $U_{\text{WT,ident}} = 12 \text{ m/s}$. The border-line cases $U_{\text{WT}} = 10 \text{ m/s}$ and $U_{\text{WT}} = 16 \text{ m/s}$ show marginal stable behavior while all other wind-tunnel speeds do not allow a stable controller operation with this particular model. Higher U_{WT} allow a wider operation range in terms of wind-tunnel speed deviation off the design point than lower U_{WT} . This observation leads to the following more precise discussion of the operating range of the controller. It depends on the phase-angle error $\Delta\Phi_e(f)$, caused by a secondary path model $\hat{H}_{ec,U_{\text{WT}}}$ recorded at $U_{\text{WT,ident}} \neq U_{\text{WT}}$.

Phase-Angle Dependent Stability

The results in Fig. 5.13 show an unstable behavior of the controller, if the deviation of U_{WT} from the design case exceeds a certain limit of $2 - 3 \text{ m/s}$. A reason for the unstable controller is the change of the transmission behavior (stability properties) of the boundary-layer flow. Therefore, a change of the phase speed and amplification of the disturbances. This effect has been discussed in literature before (Fabbiane et al. (2015); Pätzold (2013)). The following results show a detailed analysis of the controller stability based on the phase-angle error, caused by the changing phase speed of H_{ec} .

The phase-angle error $\Delta\Phi_e(f)$, relative to a reference phase-angle $\Phi_{\text{ref}}(f)$, depends on the traveled distance $\Delta x_{ce} = 0.045 \text{ m}$, the phase speed c_ω and its frequency $f = \frac{1}{T}$:

$$\Delta\Phi_e(f) = \frac{360^\circ \cdot \Delta x_{ce}}{c_\omega \cdot T} - \Phi_{\text{ref}}(f). \quad (5.5)$$

The controller takes this phase-angle error $\Delta\Phi_e(f)$ into account by using the model \hat{H}_{ec} , that is determined for a given situation (here a given U_{WT}). If

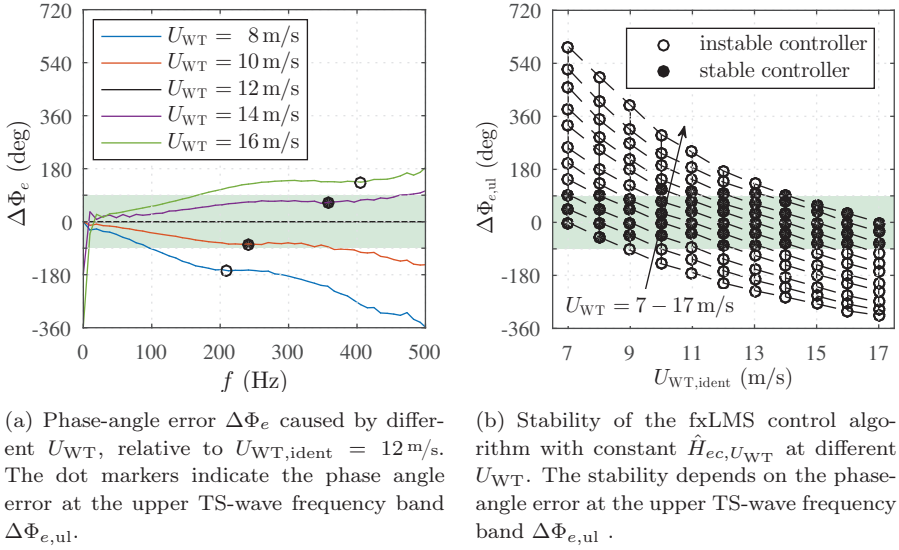


Figure 5.14.: Phase-angle error dependent fxLMS controller stability. The green highlighted area indicates the theoretically stable controller operation range.

the flow situation changes, the controller uses a wrong model that results in a phase-angle error.

The phase-angle error $\Delta\Phi_e(f)$ of \hat{H}_{ec} due to changes in velocity is shown in Fig. 5.14(a), relative to the phase angle of the reference case at $U_{WT} = 12 \text{ m/s}$. After a counter-wave is excited by the plasma actuator c it travels downstream with the flow and is measured by the error sensor e .

The absolute value of the phase-angle error $\Delta\Phi_e(f)$ increases for decreasing flow velocity. The horizontal spacing of the curves in Fig. 5.14(a) decreases for increasing U_{WT} . However, higher frequencies also cause a higher phase-angle error and the most amplified frequency is higher for increasing velocity. The phase-angle based investigations on the controller stability $\Delta\Phi_e(f)$ is now calculated for each design point $U_{WT, \text{ident}} = 7 - 17 \text{ m/s}$ at which a model $\hat{H}_{ec, U_{WT}}$ has been identified. The TS-wave bandpass is shifted to higher frequencies with higher U_{WT} and the phase-angle error $\Delta\Phi_e(f)$ is a function of frequency f . Therefore, $\Delta\Phi_e(f)$ at the upper TS-wave bandpass limit, obtained experimentally (Simon et al. (2015)), is defined as the critical phase-angle error $\Delta\Phi_{e, \text{ul}}$ (black markers). The example for $U_{WT, \text{ident}} = 12 \text{ m/s}$, shown in Fig. 5.14(a), leads to a phase-angle error of $\Delta\Phi_{e, \text{ul}} = 65.3^\circ$ at the upper frequency limit $f_{\text{ul}} = 357 \text{ Hz}$, if the controller is operated off design at $U_{WT} = 14 \text{ m/s}$.

Figure 5.14(b) shows $\Delta\Phi_{e, \text{ul}}$ caused by an off design controller operation. For each secondary path model $\hat{H}_{ec, U_{WT}}$, identified at $U_{WT, \text{ident}}$, the wind-tunnel speed U_{WT} has been varied from $U_{WT} = 7 - 17 \text{ m/s}$. The dashed lines connect the data points that belong to the same U_{WT} , whereas the wind-tunnel speed rises from bottom to top in steps of $\Delta U_{WT} = 1 \text{ m/s}$. All data points marked with filled circles show stable fxLMS controller operation and a successful wave attenuation, all other configurations are unstable (cf. Fig. 5.13). It is commonly known that the fxLMS control algorithm can theoretically compensate a $\pm 90^\circ$ phase-angle error $\Delta\Phi_e(f)$ between the secondary path model \hat{H}_{ec} and the physical path H_{ec} by adapting the filter online (Snyder and Hansen (1994)). This theoretically stable area is highlighted in green in Fig. 5.14. The postprocessing based on the phase-angle error $\Delta\Phi_e$ demonstrates the flexibility of the adaptive control algorithm in the band of $\pm 90^\circ$.

5.4. Adaptive Secondary Path for the fxLMS Algorithm

The fxLMS controller shows a robust behavior in a certain operation range, corresponding to $\pm 90^\circ$ phase-angle error (section 5.3.2). In order to extend the operational range of the controller it is necessary to adapt the secondary path online (Elliott (2000); Kuo and Morgan (1995)). Several methods for the continuous online identification of secondary paths have been investigated within the last decades, e.g. by Zhang et al. (2003). However, these methods are usually very application specific and significantly increase the complexity of the controller. In cases where the changes in the secondary path are dominated by a small number of dominant parameters, an online adaptation can be conducted using look-up tables of secondary path estimates for a parameter range of interest. The secondary path is then adopted online by measuring this dominating parameter and interpolating within the look-up table. For this approach a lot of effort is required for the initial experimental identification of the secondary path look-up table. Alternatively, if there is a functional dependency of the secondary path on the dominant parameters, then the secondary path model may be extrapolated from a single reference secondary path model.

Investigations of the transmission behavior of the boundary-layer with different flow speeds in section 5.3.1 indicate that it is possible to adapt the secondary path model H_{ec} by stretching and scaling the impulse-response model \hat{H}_{ec} with changing U_{WT} (Fig. 5.12). This section discusses the extension of the stable controller operation range by adapting \hat{H}_{ec} online.

5.4.1. Scaling and Stretching of the Secondary Path

The secondary path model \hat{H}_{ec} can be adapted during the experiments by stretching and scaling the reference impulse response $\hat{H}_{ec,ref}$. This approach is depicted in Fig. 5.15 where the solid curves show the measured \hat{H}_{ec} , copied from Fig. 5.12. The zero crossing between the global minimum and maximum is chosen as a measure for the temporal stretching and the value of the global minimum is chosen as a parameter for the amplitude scaling. 4th order polynomials are used for scaling and stretching based on U_{WT} (Simon et al. (2015)). The dashed curves in Fig. 5.15 show stretched and scaled impulse responses

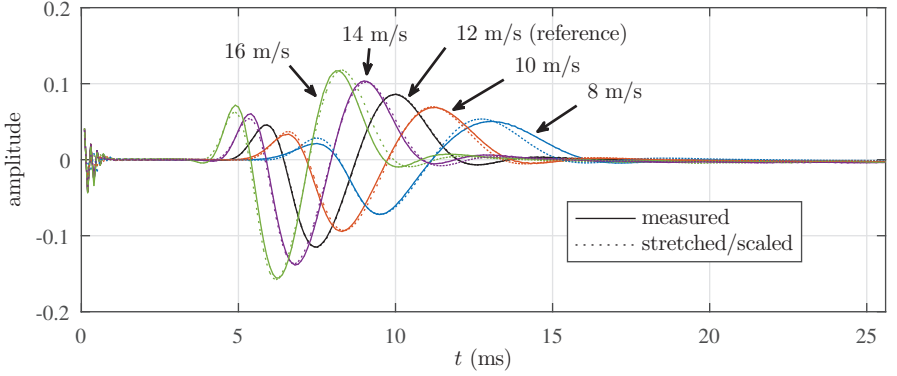
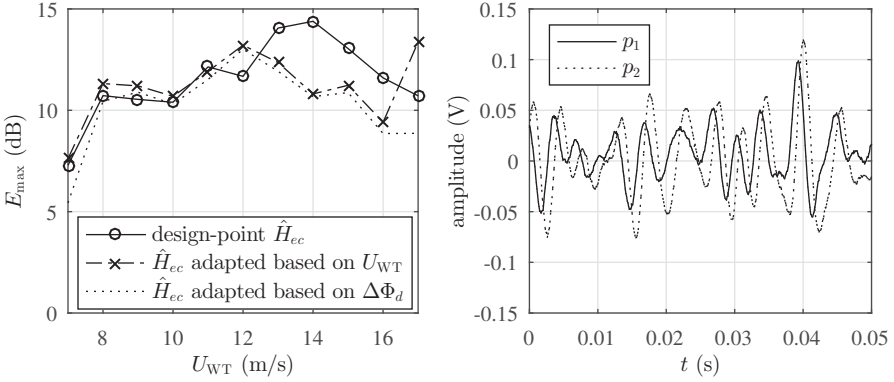


Figure 5.15.: Measured and scaled/stretched secondary path model $\hat{H}_{ec,U_{WT}}$ for different wind-tunnel speeds based on a reference $U_{WT,ref} = 12 \text{ m/s}$.

based on a \hat{H}_{ec} for $U_{WT,ref} = 12 \text{ m/s}$ and compared to the models \hat{H}_{ec} measured at each velocity individually. The presented procedure matches the shape of measured impulse responses quite well. It is updated depending on the wind-tunnel speed during the controller operation in the experiment. This procedure allows a dynamic adaption to changing flow conditions. Nevertheless, a calibration of the secondary path model adaption method is unavoidable and requires a model identification prior to the controller operation.

5.4.2. Controller Stability with Adaptive Secondary Path

The stability of the basic fxLMS control algorithm is based on \hat{H}_{ec} as a model of the boundary-layer transmission behavior. Because of its ability to adapt, the basic control algorithm also works well with slight changes of the flow speed but becomes unstable for larger deviations (Fig. 5.13). The circles in Fig. 5.16(a) show the Controller performance E_{\max} for constant secondary path models \hat{H}_{ec} , determined for each wind-tunnel speed U_{WT} and operated at each design point. The dashed line shows the attenuation obtained with a single secondary path model \hat{H}_{ec} adapted online based on U_{WT} as described above. Deviations in the Controller performance E_{\max} between both cases at the same U_{WT} result from difficulties with repeatable receptivity properties



(a) Controller performance E_{\max} with adaptive secondary path \hat{H}_{ec} . Comparison between adaption based on U_{WT} and based on the phase-angle difference $\Delta\Phi_d$. (b) Time section of the upstream sensor signals $p_1(t)$ and $p_2(t)$. Artificial broad-band TS-waves are generated at $U_{WT} = 12$ m/s.

Figure 5.16.: Secondary path adaption; performance and methods.

(section 5.1.1) and are unlikely caused by a lower control success due to the adapted secondary path. The main benefit of the adaptive secondary path model \hat{H}_{ec} is a broader operation range while the fxLMS controller with constant \hat{H}_{ec} can only adapt phase changes up to 90° . The successful adaption is reflected in the similar shape of the fxLMS kernel for the design case and the off-design case (Simon et al. (2015)).

5.4.3. Embedded Sensors for Flow-state Identification

The previously described approach for the adaption of the secondary path model is based on the knowledge of the wind-tunnel speed. Towards the development of more capable boundary-layer control systems it seems beneficial to conduct the adjustment based on locally obtained information on the flow. Alternatively to the external measure U_{WT} , the secondary path \hat{H}_{ec} can also be adapted based on the estimate of the phase-angle difference $\Delta\Phi_d$ between the signals captured at the two upstream sensors p_1 and p_2 (Fig. 5.16(b)). The phase-angle difference $\Delta\Phi_d$ is directly related to U_{WT} via the phase speed c_ω of the disturbances. This technique allows to adapt \hat{H}_{ec} based on signals

measured locally by wall mounted sensors and does not rely on a remote measure of U_{WT} . Therefore an interesting application for this technique are flight experiments, where not only the flow speed but also the pressure distribution can vary in time. The phase-angle difference $\Delta\Phi_d$ catches the phase speed of the disturbance by implication and therefore adapts the controller based on the phase speed (propagation speed) of the disturbances. This is an important feature because the wave cancellation success mainly depends on the correct phase-angle relation between the disturbance and the counteracting wave. The following paragraph describes the implementation of the phase-angle difference detection algorithm that is indicated with a P in the block diagram of the control algorithm in Fig. 3.3.

Figure 5.16(b) shows the amplified AC signals of the surface hot-wires p_1 and p_2 at $U_{WT} = 12 \text{ m/s}$. The disturbances generated upstream of the sensors travel downstream with the phase speed c_ω and cause a shift $\Delta\Phi_d$ between both sensor signals. The short distance between both sensors only lead to a limited phase-angle difference but it can be extracted as a measure for the phase speed c_ω and U_{WT} . An algorithm for phase-angle difference detection is implemented in order to be run online on the dSPACE system. The data is first filtered with a narrow 8th order IIR bandpass filter at 200 Hz. The resulting signal is then normalized in between one cycle duration $T_{200 \text{ Hz}} = 5 \text{ ms}$. The normalized signals $p_{1,n}$ and $p_{2,n}$ are now approximated as two sinusoidal signals with the same frequency f , as indicated in (5.6) and (5.7).

$$p_{1,n} = \sin(2\pi ft + \Phi_1) \quad (5.6)$$

$$p_{2,n} = \sin(2\pi ft + \Phi_2) \quad (5.7)$$

Multiplication and integration of the time signals over m periods leads to

$$\frac{1}{mT} \int_0^{mT} p_{1,n} \cdot p_{2,n} dt = \frac{1}{2} \cos(\Phi_1 - \Phi_2). \quad (5.8)$$

The phase-angle difference $\Delta\Phi_d = \Phi_1 - \Phi_2$ for both signals with the same frequency can now be calculated:

$$\Delta\Phi_d = \arccos\left(\frac{2}{mT} \int_0^{mT} p_{1,n} \cdot p_{2,n} dt\right) \quad (5.9)$$

This algorithm enables to calculate the phase-angle difference online and to update the secondary path \hat{H}_{ec} every second parallel to the controller oper-

ation. Using the trigonometric cosine function, the algorithm is only able to determine a phase-angle difference of $0^\circ < \Delta\Phi_d < 180^\circ$. The operation range of $7 \text{ m/s} < U_{\text{WT}} < 17 \text{ m/s}$ leads to phase-angle differences of less than 140° for the given sensor distance between p_1 and p_2 . The phase-angle difference method detection algorithm does only work in a limited band and therefore only for special cases. The described method for determining the propagation speed serves well as a first version for testing the usefulness of the phase-speed approach. With the applied phase-angle difference detection algorithm the achieved attenuation rate does not differ significantly from the experiments with an adaption of \hat{H}_{ec} based on U_{WT} . Fig. 5.16(a) shows a comparison between the two approaches of secondary path adaption. The dashed line shows the adaption with the external measure U_{WT} whereas the dotted line indicates the measurement results obtained with the adaption based on $\Delta\Phi_d$. Except the borderline cases $U_{\text{WT}} = 7 \text{ m/s}$ and $U_{\text{WT}} = 17 \text{ m/s}$, both adaption methods perform equally well even if the phase-angle difference based adaption does not adapt the secondary path model \hat{H}_{ec} as exact as the adaption based on the measurement of U_{WT} . Due to the robustness of the fxLMS algorithm the controller can adapt the phase-angle error between the model \hat{H}_{ec} and the current physical secondary path H_{ec} . In Chapter 6 an adaption based on the cross correlation of two sensor signals is presented that is not dependent on a previously defined disturbance frequency band.

In conclusion the application of the adaptive secondary path model \hat{H}_{ec} can be considered successful but not mandatory, if the flow speed changes are in the order of $\pm 2 \text{ m/s}$. However, the adaptive secondary path can show its real benefits when not only changes of the free-stream velocity come into play but also changes of the angle of attack of an aerodynamic airfoil. In addition, an adaptive secondary path could be necessary, if the phase-angle resolution is lowered due to a lower execution speed of the controller. A execution speed of 1 kHz would allow to cancel out disturbances with a frequency of 200 Hz but the resulting phase resolution of $\delta\Phi = \frac{360^\circ 200 \text{ Hz}}{1000 \text{ Hz}} = 72^\circ$ is already a large amount of the $\pm 90^\circ$ phase-angle error that can be adapted by the fxLMS algorithm.

5.5. Conclusions

The stability of control algorithms for active wave cancellation of artificially generated single-frequency as well as broad-band 2D Tollmien-Schlichting has been investigated for changing inflow parameters in a flat plate boundary layer. The comparison between the (optimal) LQG controller with static compensator kernel and fxLMS with adaptive kernel has shown that the role of optimality has been overemphasised in the past, in particular in numerical investigations. The results presented in this chapter show that the adaptivity plays a more important role as the maximum achievable control success in the experiment is similar for both approaches.

The basic fxLMS controller is able to adapt changes in the physical secondary path H_{ec} of $\pm 90^\circ$ compared to the used secondary path model \hat{H}_{ec} . This allows stable controller operation with velocity deviations up to 4 m/s in the considered operation range for wind-tunnel speeds of $7 \text{ m/s} < U_{WT} < 17 \text{ m/s}$.

In order to extend the operation range of the system, an adaptive secondary path model \hat{H}_{ec} is implemented, which allows a stable controller operation for the whole considered velocity range. The adaptive secondary path model \hat{H}_{ec} requires a calibration before running the controller but allows a parameterized adaption based on flow quantities. The adaption can be realized by an external measure like the wind-tunnel speed U_{WT} or by wall bounded phase-speed measurements with two upstream sensors. The extended operation range only works for rather slow varying inflow parameters, not unsteady aerodynamics, because the adaption process takes some seconds. A good example for slowly varying conditions is an aircraft flying through the atmosphere with changing weight and altitude, but this application requires additional modifications on the control algorithm, which are discussed in the next chapter.

6. In-Flight Experiments under Varying Inflow Conditions

The goal of the active wave cancellation research is certainly its application on a real aircraft wing in flight. The wing glove, described in detail in section 3.5, is a unique test bed for the applied technology in flight. In section 6.1 the base flow around the wing glove is characterized, a DNS model of the flow and BL stability properties are extracted. Both, fxLMS and the newly introduced dxLMS control algorithm, are used for active wave cancellation of two-dimensional broadband TS-waves with a SISO system and the results are presented in section 6.2. Similar to Chapter 5 the controller stability for varying inflow conditions is investigated. Finally, a model-free approach for dxLMS operation is introduced to operate the controller as a “black box” system. It automatically adjusts the controller settings based on a group speed measurement of the disturbance wave packets is presented. The modified dxLMS controller is operated without a model and is able to adapt to varying conditions that may occur during flight in atmosphere. Concluding remarks summarize the content of this chapter in section 6.3

6.1. Base Flow around the Wing Glove

All test flights are conducted in gliding flight without a running engine, which requires a special in-flight testing procedure, as explained in section 3.5.2. Based on these experiments, the base flow around the wing is characterized. The DNS is fitted to one in-flight case in section 6.1.1. Based on the flow field obtained by DNS, the stability properties of the BL are investigated by linear theory in section 6.1.2.

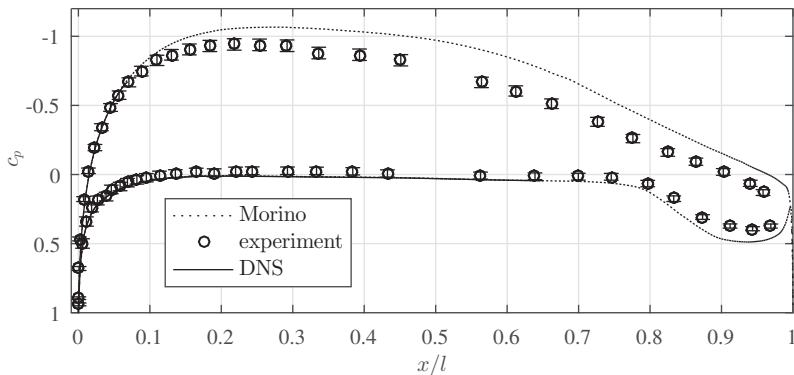


Figure 6.1.: Measured and calculated pressure distribution at $\alpha = 2.5^\circ$. The error bars indicate the standard deviation, calculated over 20 s.

6.1.1. A Direct Numerical Simulation Model of the Flow

As discussed in section 3.5, the angle of attack measurement with the *Dornier Flight Log* gives only a rough estimate of the in-flow conditions, as the systematical error due to positioning of the probe is not taken into account. Therefore, the pressure distribution around the wing glove as well as the dynamic pressure q measured upstream of the wing are the reference values for comparison with numerical investigations. Figure 6.1 shows the averaged pressure distribution for $\alpha = 2.5^\circ$ measured in flight. The error bars indicate the standard deviation of c_p caused by inflow fluctuations. The fluctuations are small because the flights are conducted early in the morning in calm air. The boundary layer is tripped artificially on the suction side of the wing glove by surface roughness, visible in the pressure distribution as a rising pressure at $x/l = 0.3$.

Due to the high Reynolds number, small displacement thickness and moderate α , potential flow theory provides a good estimate of the pressure around the wing glove. The potential flow solution, calculated with a Morino method (Morino and Kuot (1974)), is drawn as a dashed line in Fig. 6.1. All experiments are conducted on the pressure side of the wing glove. Therefore, the angle of attack is iterated for the potential flow solution in order to match the pressure distribution and, more important, the pressure gradient on the lower side. In the following discussions, only the value for α measured during the

experiment in flight is given. The potential flow solution serves as an initial condition for DNS calculations that pursues two goals: First, the comparison between flight experiments and numerical simulations and second, parameter studies under controlled conditions. A comparison between numerical and experimental pressure distribution, presented in Fig. 6.1, shows a good agreement on the pressure side.

The DNS calculations have been performed by the cooperation partner Nicolò Fabbiane. Therefore, the information about the DNS model of the flow are mainly taken from the joint publication (Simon et al. (2016a)).

A spectral-element method (SEM) code – Nek5000 – is used to perform two-dimensional (2D) direct numerical simulations of the incompressible flow close to the wing (Fischer et al. (2008)). The code is based on a discretisation of the computational domain in spectral elements (Patera (1984)). In each element the flow is approximated by 2D Legendre-Gauss-Lobatto polynomials up to degree N . The Reynolds number $Re_l = \frac{U_\infty l}{\nu}$ for the simulations is $3.75 \cdot 10^6$. The computational domain extends along the airfoil from $x/l = 0.1$ on its upper surface to $x/l = 0.65$ on the lower side, cf. Fig. 6.2. The domain is discretized in 20000 2D spectral elements of order $N = 12$ on both directions: Four hundred elements are distributed along the airfoil surface and 50 along the wall-normal direction with cosine distribution to form a curvilinear grid. The wall-normal and wall-wise size of the elements reaches from a minimum of $4 \cdot 10^{-5}$ and $7 \cdot 10^{-4}$ close to the wall to a maximum of $1 \cdot 10^{-2}$ and $7 \cdot 10^{-3}$ in the free stream.

A no-slip boundary condition is enforced on the airfoil surface. On the free-stream boundary, a Dirichlet boundary condition enforces the solution to the potential solution of the flow, corrected for the presence of a boundary layer. The two outflow boundaries are treated according to Brynjell-Rahkola (2015): On the boundary, pressure and velocity are linked by the relation

$$\frac{1}{Re_l} \frac{\partial u_n}{\partial n} - p = -p_a, \quad (6.1)$$

where n is the boundary-normal direction and u_n the component of the velocity normal to the boundary. The pressure is indicated by p and the boundary pressure p_a is computed from the superposition of the potential flow and Falkner-Skan boundary-layer solution.

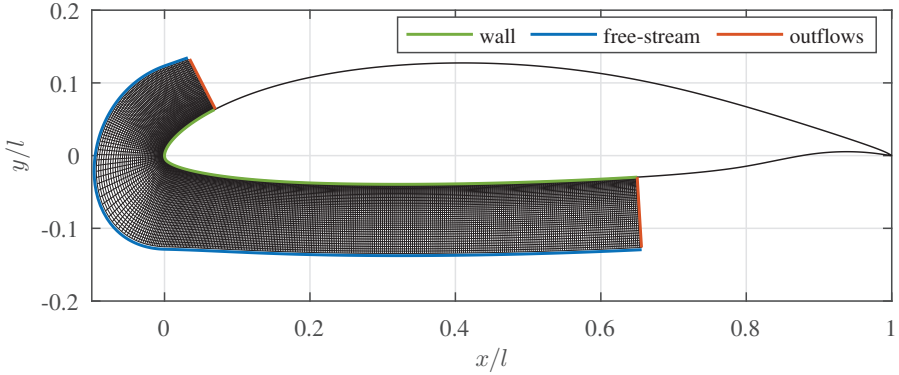


Figure 6.2.: Computational Mesh for the DNS of the flow around the wing glove.

Linear Simulations

Linear simulations are performed with respect to the steady solution. The boundary condition for the perturbation velocity is similar to the baseflow boundary conditions: No-slip on the surface, homogeneous Dirichlet on the free-stream boundary and homogeneous outflows (i.e., $p_a = 0$). In addition, sponges are placed in front of each outflow in order to avoid reflections: Both upper and lower sponges have the thickness $\Delta x/l = 0.05$.

Input and output devices used in the experimental setup are modelled in the numerical simulations. Surface hot-wires are represented by a weighted average of the wall shear stress: A Gaussian function with variance $10^{-3}l$ is used as a weight function. The disturbances generated by the loudspeakers is modelled by a train of synthetic vortices introduced at the same location as the loudspeakers in the experimental setup (Bagheri et al. (2009)). The plasma actuator is represented by a volume forcing based on the results by Kriegseis et al. (2015, 2013b) at the PA's location (Fabbiane et al. (2015)).

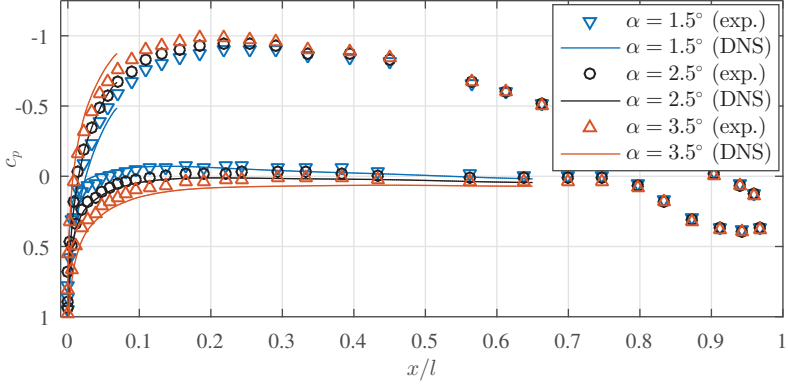


Figure 6.3.: Measured and calculated pressure distribution for different angles of attack α .

Angle of Attack Range for the Experiments

Active wave cancellation in the laminar boundary layer requires a sufficiently low amplitude of the disturbances at the actuator position such that the transition process is in the linear regime, cf. section 5.1.1. For the in-flight experiments, this leads to a range of $1.5^\circ < \alpha < 3.5^\circ$ in which the experiments with artificially generated 2D disturbances are reasonable. Lower values for α would lead to interaction of the artificial 2D waves with natural 3D disturbances. Higher values for α would lead to more stable laminar boundary layer at the disturbance source position and no amplification of the artificially introduced disturbances. The pressure distributions for the considered range are shown in Fig. 6.3. It is obvious that the pressure gradient in the mid-chord region of the pressure side can be altered from slightly negative for $\alpha = 3.5^\circ$ to slightly positive for $\alpha = 1.5^\circ$.

6.1.2. Boundary-layer Stability of the Base Flow

The boundary-layer profiles extracted from DNS calculations enable investigations on the linear stability of the boundary layer in the considered range of flight states. Three neutral stability curves and n -factor contour plots, calculated with PSE (Juniper et al. (2014)), are shown in Fig. 6.4. The sensor positions are indicated as red triangles while the disturbance source d is marked with a \triangle , cf. Fig. 2.8.

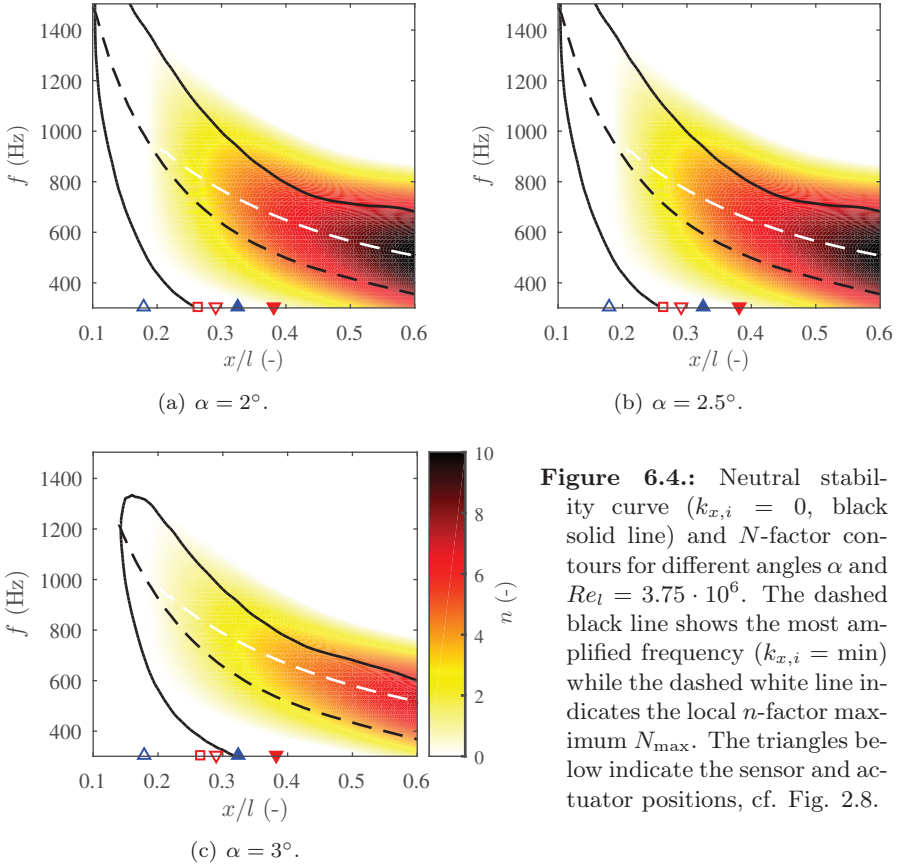


Figure 6.4.: Neutral stability curve ($k_{x,i} = 0$, black solid line) and N -factor contours for different angles α and $Re_l = 3.75 \cdot 10^6$. The dashed black line shows the most amplified frequency ($k_{x,i} = \min$) while the dashed white line indicates the local n -factor maximum N_{\max} . The triangles below indicate the sensor and actuator positions, cf. Fig. 2.8.

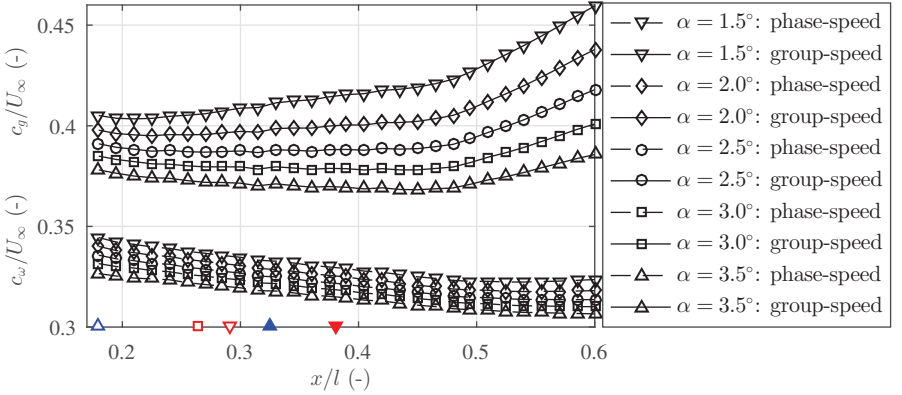


Figure 6.5.: Non-dimensionalized phase speed c_w/U_∞ and group speed c_g/U_∞ of the disturbances at the frequency for N_{\max} , obtained by PSE calculations. The triangles below indicate the sensor and actuator positions, cf. Fig. 2.8.

Because the experiments are conducted on the pressure side of the wing glove, the pressure gradient decreases for higher α , yielding a stabilised laminar boundary layer. This results in a downstream-shifted neutral stability curve ($k_{x,i} = 0$) and a slightly shifted amplified frequency band. The flat shape of the middle region of the airfoil (Fig. 3.12) leads to rather low amplified transition scenarios and a significant movement of the transition region for a change of α , as shown by Reeh (2014) for the same airfoil in flight. For all three presented cases, the actuation with the PA (\blacktriangle) is active in a low amplified region where $n \approx 4$. The low amplification rates are necessary to generate artificial 2D waves that dominate the natural disturbances. Future experiments on wave cancellation of natural disturbances with distributed actuators would not require such a low amplification because no artificially generated 2D wavefront is present.

Based on the PSE results, the propagation behavior of the disturbances can be investigated in more detail. Figure 6.5 shows the non-dimensionalized phase speed c_w and group speed c_g for the local maximum n -factor N_{\max} and $1.5^\circ \leq \alpha \leq 3^\circ$. The phase speed c_w and the group speed c_g slow down about 5% in the region between the sensors p (\square) and e (\blacktriangledown). The consequences of a changing group speed c_g for the normalized time delay γ (2.35) are discussed later in section 6.2.2.

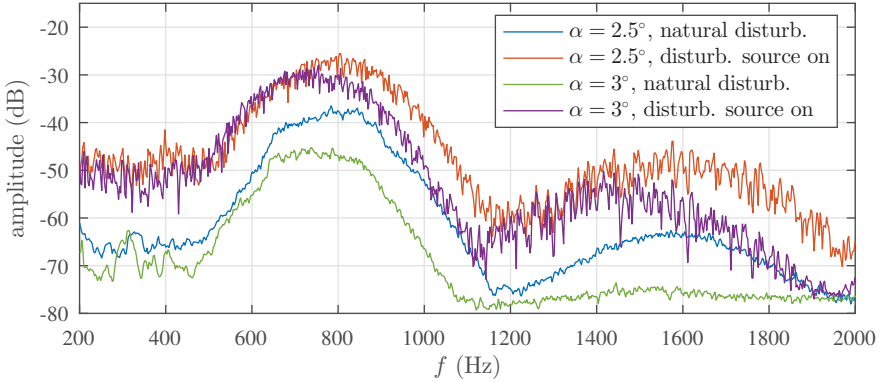


Figure 6.6.: Power-spectral density of the error sensor signal $e(t)$ for natural and artificially generated TS-wave disturbances measured in flight.

The flow control setup is a SISO system as mentioned before. Since only one actuator is mounted in spanwise direction, a 2D wavefront is required for the experiment. Natural TS-waves occur in wave packets with a modulation in spanwise direction (Peltzer et al. (2009); Saric et al. (2002)). Therefore, artificial disturbances with an even wavefront are generated by the disturbance source. Figure 6.6 shows the power spectral density of the reference sensor signal $r(t)$ for the natural and artificial case (disturbance source switched on). The artificially generated 2D waves show amplitudes, which are 12 dB to 15 dB higher compared to the natural case, depending on the angle of attack α . This emphasises that the naturally occurring 3D waves can be neglected and a 2D problem is present during the experiments in the considered region. Limited space for sensors and measurement time causes the lack of measurements to proof the 2D character of the wavefront as it was conducted for the wind-tunnel experiments, cf. Fig. 5.4. The speakers are positioned directly underneath the surface, and the resulting small dead volume leads to the assumption that the speakers generate a 2D wave. The steady part of the PA force alters the boundary-layer profile and therefore also the stability properties of the boundary layer (Duchmann et al. (2014)). For the present case, the high flight speed in combination with the rather low steady forcing of the PA leads to the assumption of a negligible effect of the boundary-layer stabilisation on the AWC experiments described in the following.

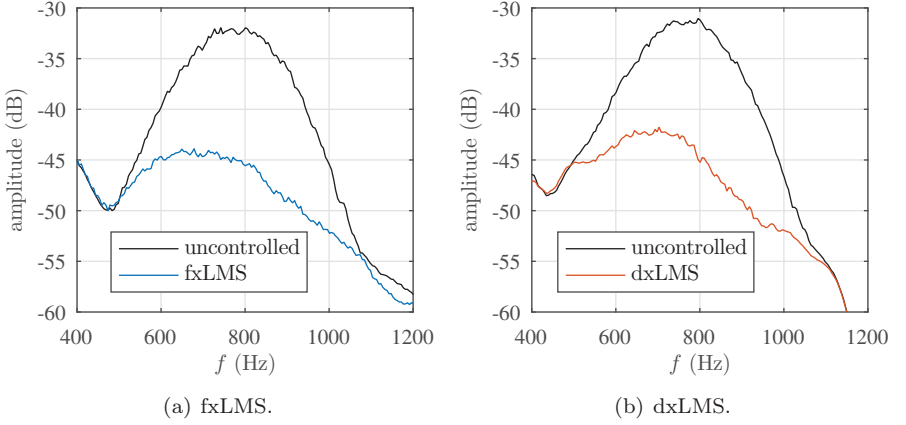


Figure 6.7.: Control success of the active wave cancellation for fxLMS and dxLMS ($N_P = 128$) algorithm at $\alpha = 3^\circ$ in flight. The power-spectral density curves show the signal reduction at the error sensor e .

6.2. Active Wave Cancellation with dxLMS and fxLMS Controller

Several experiments with successful TS-wave cancellation of broadband disturbances with adaptive fxLMS algorithms have been reported in Chapter 5 of this thesis and in the literature (Fabbiane et al. (2015); Simon et al. (2015); Sturzebecher and Nitsche (2003)). The successful application of the fxLMS controller for $U_\infty = 40.3 \text{ m/s}$ and $\alpha = 3^\circ$ with a broadband disturbance is shown in Fig. 6.7(a). The disturbances at the error sensor e , which range from about 500 Hz to 1100 Hz, are almost completely attenuated.

The dxLMS control algorithm works as good as the fxLMS algorithm even with this very simplified model of the transmission behavior of the secondary path H_{ec} . Figure 6.7(b) shows an amplitude reduction of 12 dB to 15 dB, if the controller is operated. For dxLMS controller operation, a digital bandpass filter (400 to 1100 Hz) is implemented in the Simulink model for all sensor signals. The filter is necessary because the dxLMS controller adaptation can become unstable for low-frequency disturbances due to a phase-angle error, discussed later in this section.

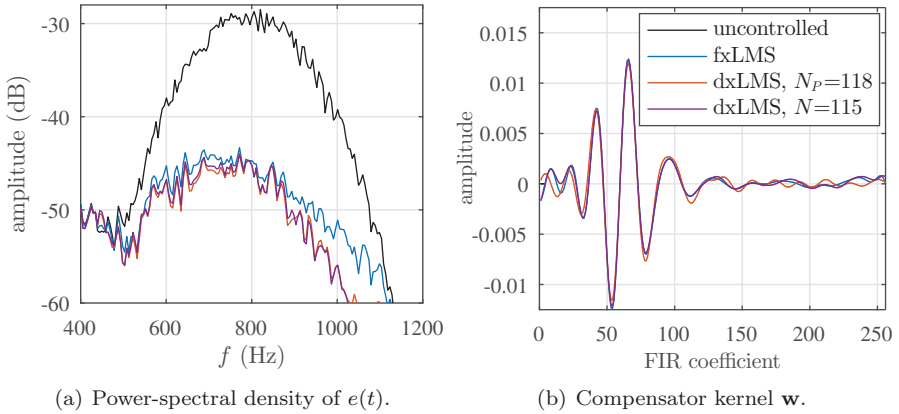


Figure 6.8.: Controller simulation (offline) of fxLMS and dxLMS for the same test case with experimental data input. The transmission path is recorded at $\alpha = 2.5^\circ$ and the dxLMS algorithm is operated with delays of $N_P = 118$ and $N = 115$.

For direct comparison of both controller concepts, the boundary conditions have to be the same. Wind-tunnel experiments can fulfill this requirement but for the flight test case an offline simulation of the controller behavior is necessary, cf. section 3.6. Figure 6.8(a) shows the offline simulated controller behavior for exactly the same boundary conditions. The direct comparison shows that both controllers perform equally well while small deviations are caused by the adaptation process of the LMS algorithm. It should be noted here that the dxLMS controller shows almost exactly the same signal reduction for $N_P = 118$ samples compared to a shorter delay of $N = 115$ samples. The delay $N = 115$ samples is obtained with the normalized time delay approach (2.36) and discussed more in detail later in section 6.2.2.

The LMS adaptation algorithm estimates the control path H_{cr} with a FIR filter \mathbf{w} , which describes the transmission behavior from the reference sensor r to the PA c . The filter \mathbf{w} is also known as compensator kernel and is shown in Fig. 6.8(b) for the offline simulated cases presented in Fig. 6.8(a). The FIR filters differ only significantly for the first twenty coefficients, but the most characteristic peaks, responsible for a successful TS-wave damping (Fabbiane et al. (2015)), match well.

The control success with the dxLMS algorithm can be explained by looking

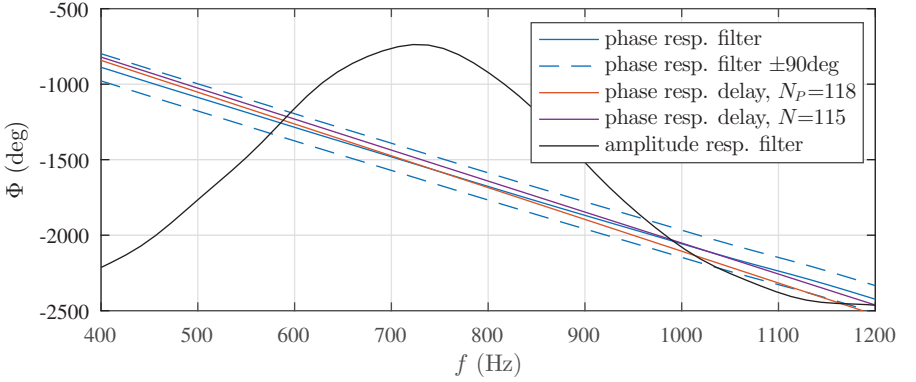


Figure 6.9.: Phase response of the secondary path model filter \hat{H}_{ec} and a delay of $N_P = 118$ for dxLMS operation for the test case shown in Fig. 6.8(a). The amplitude response of \hat{H}_{ec} is qualitatively plotted on top (logarithmic scale).

at the phase response of the transmission paths. As shown in section 5.3, the fxLMS controller performance is almost constant for the stable controller parameters but decreases abruptly if $\pm 90^\circ$ phase-angle error of the secondary path model is exceeded. The solid blue line in Fig. 6.9 shows the phase response of the secondary path model filter \hat{H}_{ec} , while the dashed lines indicate the $\pm 90^\circ$ boundary. The phase response of a delay is a straight line with the slope $\frac{\partial \Phi}{\partial f} = -\frac{360^\circ N}{f_s}$ and for the presented case with $N_P = 118$ the phase response lies in-between the $\pm 90^\circ$ boundary for the amplified region of the boundary layer. The amplitude response of \hat{H}_{ec} is plotted qualitatively as a black solid line and marks the important region below the TS-wave “hump” where the disturbances in the boundary layer are amplified. For the optimal delay of $N_P = 118$ the phase responses of \hat{H}_{ec} and the delay meet at the most amplified frequency $f \approx 720$ Hz, whereas the curve for $N = 115$ intersect above the amplified band at $f \approx 1030$ Hz. Both lie in-between the $\pm 90^\circ$ boundary for the whole band as indicated in Fig. 6.9. The dxLMS controller requires an additional bandpass filter to avoid an unstable controller adaptation caused by disturbances below the TS-wave frequency band, which are not amplified by the boundary layer but can exceed the $\pm 90^\circ$ boundary. The amplitude response of the delay is equal to one for the whole frequency range.

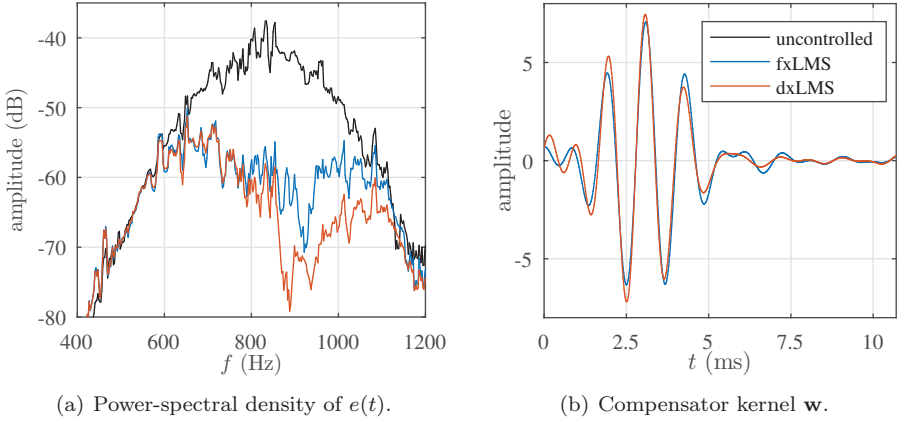


Figure 6.10.: Comparison between fxLMS and dxLMS operation, performed with DNS data for $\alpha = 2.5^\circ$ and $Re_l = 3.75 \cdot 10^6$. Data sets are normalized with respect to the introduced disturbance.

Controller Simulation with DNS Data

The in-flight measurements are limited to un-calibrated measurements with surface hot-wires. A measurement of the control success in terms of disturbance amplitude growth along the streamwise direction is not possible. The DNS results allow the evaluation of the control success from the flow field. Figure 6.10(a) shows the PSD of the error sensor signal for the uncontrolled case as well as for dxLMS and fxLMS operation. The fxLMS controller causes about 15 dB reduction in the amplified region, while the dxLMS controller performs equally well for $f < 900$ Hz but slightly better for $f > 900$ Hz, which is consistent with the experimental results in Fig. 6.8(a). The converged kernels \mathbf{w} for both control approaches (Fig. 6.10(b)) match well but the dxLMS kernel differs slightly, similar to the experimental case shown in Fig. 6.8(b).

An evaluation of the whole flow control approach is not possible only by analyzing the error sensor signals because it only includes the performance at one point. The flow field obtained by DNS is the basis for the prediction of the perturbation energy evolution for both control approaches, dxLMS and fxLMS. An integral value for the perturbation energy at a certain streamwise location is defined as $E_{TS}(x) = \int_{y=0}^{\infty} |(u'(x, y))^2| dy$. Figure 6.11 shows the

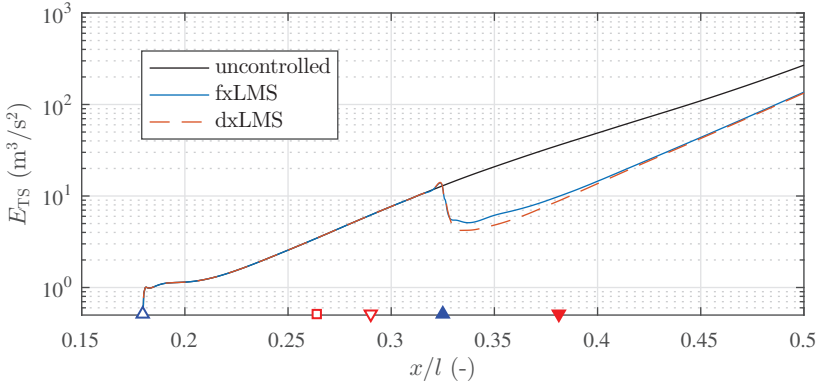


Figure 6.11.: Perturbation energy $E_{TS}(x)$ development on the pressure side, computed with DNS.

streamwise evolution of $E_{TS}(x)$. The amplitude drops down at the actuator position PA (▲) and grows again. The DNS results demonstrate that $e(t)$ is a good measure for the control success and the wave cancellation has a sustained effect on the disturbance amplitude downstream.

6.2.1. Varying Inflow Conditions

The stability and robustness of the fxLMS and dxLMS control algorithms are mainly dependent on the secondary path model \hat{H}_{ec} and the delay N . The corresponding FIR filters of \hat{H}_{ec} are shown in Fig. 6.12 for different angles of attack α and flight speeds U_∞ . It is obvious that the curves of \hat{H}_{ec} are stretched for higher α and the amplitude is higher for lower α . This corresponds well with the observations of the flat-plate experiments in section 5.3.2, where scaling and stretching factors for a model adaptation for the fxLMS controller are introduced. This is done by a system identification and controller calibration for a certain range of wind-tunnel speeds and an online adaptation during the experiment. The black curve in Fig. 6.12 ($\alpha = 2.5^\circ$, $U_\infty = 37.2 \text{ m/s}$) shows that such a pre-calibration of the system is not possible. Because of flight mechanics, the flow around the wing changes during flight. All transfer functions but the black curve are recorded at a flight altitude of about 8000 ft while the black curve is recorded at 3000 ft during the same gliding

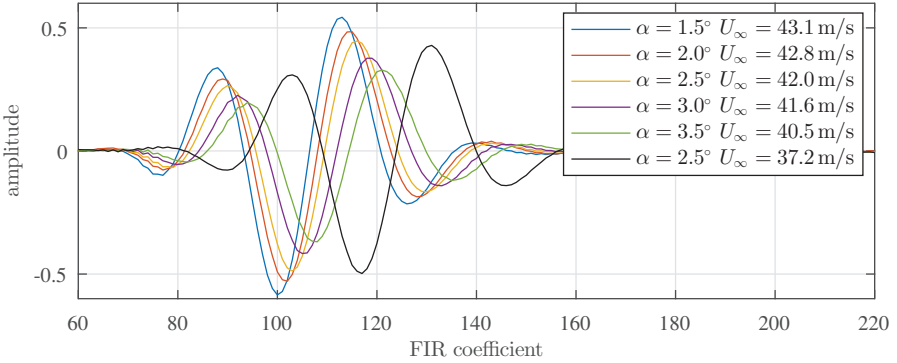


Figure 6.12.: Secondary path model \hat{H}_{ec} for different α and flight altitudes, measured in flight.

flight. Even if the mass of the glider (wing surface area S) and required lift F_L remain the same, the air density ρ changes with altitude, and therefore, the flight speed U_∞ changes for a constant α (or lift coefficient C_L):

$$F_L = C_L \cdot \frac{\rho}{2} U_\infty^2 S. \quad (6.2)$$

The increased density ρ at the lower altitude leads to a lower flight speed U_∞ and therefore to a lower group speed c_g of the Tollmien-Schlichting waves, which is visible in a shift to the right in Fig. 6.12. The amplification of the disturbances is mainly influenced by the pressure gradient or α , respectively. This is why the amplitude of both measurements for $\alpha = 2.5^\circ$ remains constant. However, the shift of the curves leads to a phase-angle error. A pre-calibrated system would lead to an unstable controller behavior, if the phase-angle error caused by the decreased group speed is higher than $\Delta\Phi_e = \pm 90^\circ$.

DNS Simulations of \hat{H}_{ec} with Variable Inflow Conditions

Due to the changing boundary conditions, the flight data are not ideal for a parametric study of α and U_∞ . The DNS calculations shown in Fig. 6.13 enable to investigate the influence of each parameter independently. A variation of α in Fig. 6.13(a) is associated with an increasing amplification for lower α but also the shape of the filter \hat{H}_{ec} is shifted to the left because of

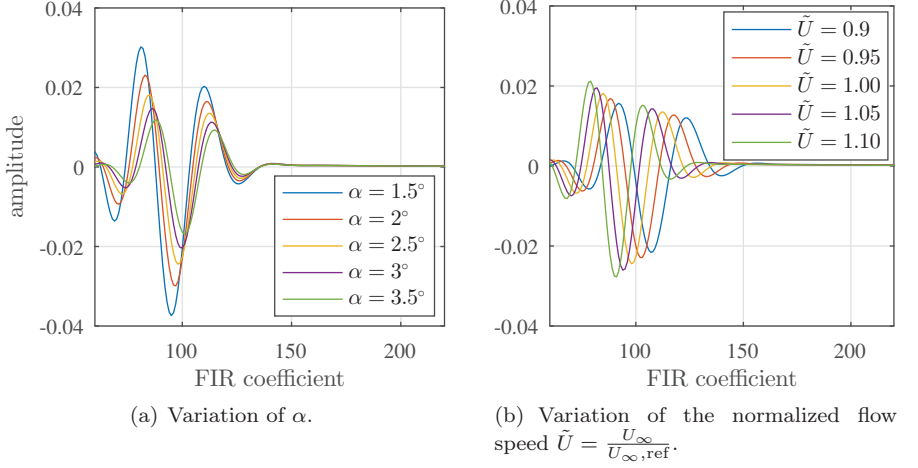
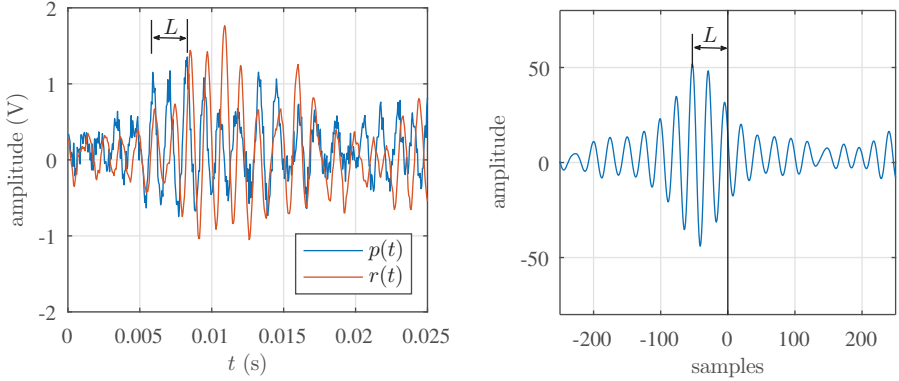


Figure 6.13.: Parameter study of the secondary path model \hat{H}_{ec} for parameters α and U_∞ , computed with DNS data .

the increased group speed c_g , cf. Fig. 6.5. The flow speed U_∞ is varied by $\pm 10\%$ at $\alpha = 2.5^\circ$, and the resulting secondary path model \hat{H}_{ec} is shown in Fig. 6.13(b). The shift of the curves is more significant for the change of U_∞ compared to α but the amplification is almost not influenced by U_∞ . Compared to the experimental values, the DNS results do not match exactly because α and U_∞ are coupled in-flight, but the observations of the parameter study can also be made with the experimental results in Fig. 6.12.

6.2.2. dxLMS Controller Stability and Model Adaptation

The discussion of the varying flow conditions during flight in the last paragraphs shows the need for a model adaptation during operation of the LMS algorithm. In section 2.2.4 the calculation of the required delay N with an online-measured normalized time delay γ has been introduced (2.36). It is applied for the following in-flight investigations.



(a) Upstream sensor signals $p(t)$ and $r(t)$. The lag sensor signal $p(t)$ is amplified by a factor of 2 for clarity.

(b) Cross-correlation of $p(t)$ and $r(t)$.

Figure 6.14.: Calculation of the time lag L between two upstream sensor signals, measured in flight.

Figure 6.14(a) shows two upstream sensor signals $p(t)$ and $r(t)$ extracted from the test case shown in Fig. 6.8(a). The characteristics of the signals are almost the same, while $r(t)$ is slightly shifted to the right due to the sensor distance Δx_{pr} and the group speed c_g of the downstream traveling waves. The shift between the signals L is extracted from the cross-correlation of both signals, presented in Fig. 6.14(b). A number of 2000 samples were found to give reliable results for the online calculation on the dSPACE system that implies an update of L every 0.1 s. The determined value of $L = 53$ samples can now be used to determine γ . For the presented example, this leads to

$$\gamma = \frac{L}{\Delta x_{pr}} = \frac{53 \text{ samples}}{35 \text{ mm}} = 1.514 \text{ samples/mm.} \quad (6.3)$$

The required delay N can now be calculated based on γ :

$$N = \gamma \cdot \Delta x_{ce} = 115 \text{ samples.} \quad (6.4)$$

Compared to the optimal delay $N_P = 118$ samples, the delay determined by cross-correlation is slightly underestimated. The change of the group speed c_g leads to an error of $\Delta N = -3$ samples, but it can be compensated by the adaptive character of the LMS algorithm as shown earlier in Fig. 6.8(a).

Phase-angle Resolution

The phase-angle resolution $\delta\Phi(f)$ of a disturbance with the frequency f is critical for the stability of the controller because a phase-angle error for the secondary path model \hat{H}_{ec} of less than $\pm 90^\circ$ is required as explained in section 2.2. A sample rate of $f_S = 20$ kHz leads to a phase-angle resolution of $\delta\Phi = 14.4^\circ$ for a disturbance with a frequency of $f = 800$ Hz. Flow control at higher flow speeds requires higher sampling rates. The model-free approach can only work, if the phase-angle shift $\Delta\Phi$ can be resolved. The ratio of the sensor distance Δx_{pr} compared to the distance Δx_{ce} influences the resolvable signal lag. For the given example, the required delay N can only be determined with a resolution of

$$\delta N = 1 \text{ sample} \frac{\Delta x_{ce}}{\Delta x_{pr}} = 2.17 \text{ samples.} \quad (6.5)$$

In conclusion, the sample rate and the upstream sensor distance are most important for the success of the presented model-free control approach. The positioning of the lag sensor p between r and c could provide a possibility to minimize the influence of a changing group speed in the streamwise direction.

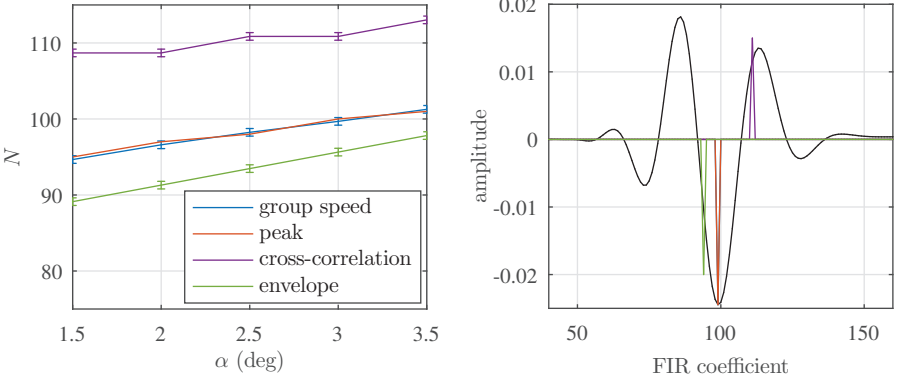
Methods for Delay Identification

The DNS results allow one the computation of the delay N based on different methods:

- group speed c_g , based on the stability properties.
- based on a peak in the secondary path model \hat{H}_{ec} .
- correlation techniques, based on the sensor signals $p(t)$ and $r(t)$.

Figure 6.15(a) shows a comparison between the methods. Based on the stability of the boundary layer, the average group speed c_g between PA (x_c) and x_e can be calculated, cf. Fig. 6.5. Equations (2.33) and (2.34) then translate the time shift τ with the sample rate f_S to a delay N . The resulting N increases with α because c_g slows down due to the decreasing flight speed U_∞ .

Plotting the position of the delay in a secondary path FIR filter curve (Fig. 6.15(b)) shows an interesting fact: The group speed is represented by



(a) Delay N for dxLMS operation, computed using group speed, the (negative) peak of \hat{H}_{ec} and the cross-correlation or the envelope of the cross-correlation from $p(t)$ and $r(t)$.

(b) Secondary paths \hat{H}_{ec} for fxLMS operation and different delays N for the dxLMS approach.

Figure 6.15.: Calculation of the delay N between with different methods. The data are obtained via DNS simulations at $\alpha = 2.5^\circ$.

the global minimum of the impulse response curve. A reason for this behaviour is that the peak (global minimum) of the impulse response is a very good measurement of the center of the wave packet. A model-free dxLMS operation based on the cross-correlation of the upstream sensor signals $p(t)$ or $r(t)$ has been introduced and works well for the data recorded in flight, cf. Fig. 6.14(b). However, for the cases calculated by DNS, the dxLMS controller is unstable because the second positive peak is lower in amplitude, compared to the experimentally obtained curves in Fig. 6.12 and leads to a slightly changed phase response.

Another correlation technique is a time lag measurement based on the envelope of the cross-correlation, cf. Fig. 6.16(a). The maximum of the envelope is the lag L between the sensor signals $p(t)$ and $r(t)$. Due to the envelope technique, the corresponding delay N is now close to the group speed c_g and therefore also the minimum peak in Fig. 6.15(b). As discussed earlier, c_g is decreasing with x and the envelope technique underestimates the delay slightly.

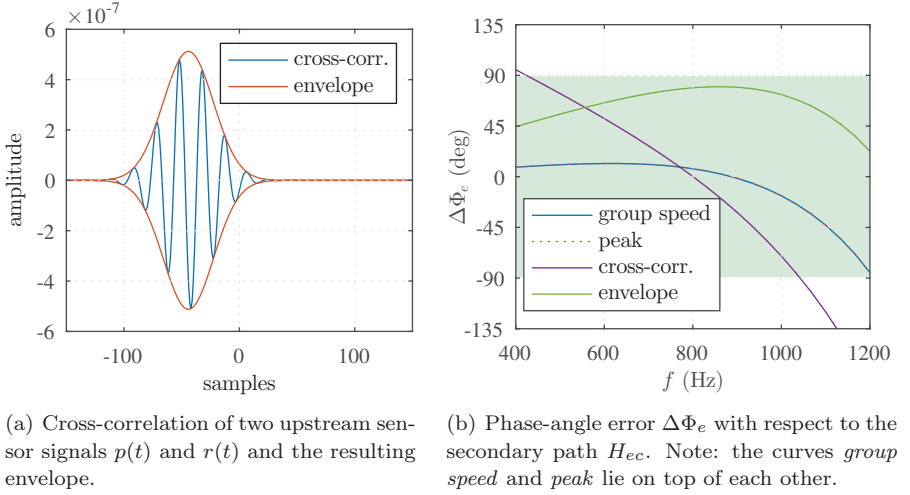


Figure 6.16.: Relation between envelope delay calculation method and phase-angle error $\Delta\Phi_e$. The data are obtained via DNS simulations at $\alpha = 2.5^\circ$.

Phase-angle Error for Different Delay Identification Methods

The most critical part, which can be well investigated with the DNS results, is the phase-angle error $\Delta\Phi_e$ between the secondary path model \hat{H}_{ec} and the actual secondary path H_{ec} . Figure 6.16(b) shows $\Delta\Phi_e$ for all four different delay approaches. The two methods based on the group speed c_g and the (negative) peak lie on top of each other due to the same delay N . The curves are shifted by a zero-cross phase of $\Delta\Phi_0 = 180^\circ$ because of the negative gain, described in (2.39). In comparison with the group speed method, the cross-correlation method fulfills the stability criteria of the LMS ($\pm 90^\circ$ limit, highlighted in green) only in a short band and does not match the slope of H_{ec} well but crosses the phase response ($\Delta\Phi_e = 0$), as already seen in the experimental results in Fig. 6.9. The group speed and peak-based delay match the slope much better and leads to a phase-angle error $\Delta\Phi_e$ close to zero for a wide range of the amplified frequency band, cf. Fig. 6.4(b). A model-free dxLMS operation is more robust in terms of LMS controller stability with the envelope method introduced above; the DNS results presented in Fig. 6.10 are obtained by using this method.

For dxLMS controller operation, the zero-cross phase of $\Delta\Phi_0 = 180^\circ$ can be realized by adjusting the control law (2.31) with a negative gain (-1) as follows:

$$\mathbf{w}(n+1) = \mathbf{w}(n) + (-1)\alpha\mathbf{r}(n)z^{-N}e(n) \quad (6.6)$$

The discussion above illustrates that particular care has to be taken in identifying the center of the wave-packet trace. A cross-correlation method may lead to an error in the time delay or phase angle, respectively. Moreover, the error of the correlation is also caused by a variation in the group speed between the sensor locations: For this setup, the error does not compromise the stability of the control algorithm and the error reduces by increasing the angle of attack, cf. Fig. 6.15(a). However, a small systematic error will always be present.

6.3. Conclusions

The main focus of this chapter is the controller stability for an in-flight scenario paired with a detailed investigation of the boundary-layer transmission behaviour, supported by DNS. The performance of the reliable fxLMS control algorithm and the newly introduced modified dxLMS control algorithm has been investigated for active wave cancellation in flight under realistic atmospheric conditions.

Performance-wise the dxLMS and fxLMS control algorithms work equally well, if the delay N is chosen in such a way that the phase-angle error $\Delta\Phi_e \leq \pm 90^\circ$. In-flight measurements and DNS simulations showed that the group speed of the TS-wave disturbances changes significantly dependent on the environmental conditions, as e.g. on the altitude. The resulting phase-angle error $\Delta\Phi_e$ leads to an unstable controller behaviour, if a previously identified model of the boundary-layer transmission is not valid anymore.

The introduced model-free “black box” system successfully works without any previous information about the environmental conditions and successfully cancels out TS-wave disturbances with the presented SISO system. An advanced method for dxLMS controller operation and the determination of N , based on the group speed measurement, has been introduced and theoretically derived. In addition, the dxLMS algorithm requires less computational

power because a FIR filter is replaced by a simple delay N . With regard to future MIMO systems for active wave cancellation of naturally occurring 3D wave packets, the dxLMS approach is a key development for less complex but robust control algorithms.

7. Potential of Plasma Actuator Arrays for Transition Delay

The need of spanwise PA arrays for cancellation of natural TS-waves has been motivated in the previous chapters. In this chapter, the challenges for the application of PA arrays to control this realistic transition scenario is discussed. For the 3D investigations, the flat plate wind-tunnel model itself is not replaced but a spanwise array of PAs and additional surface hot-wire sensors are mounted, cf. section 3.4. Besides several transmission paths of the MIMO system, the modification of the base flow due to the steady PA forcing is of interest. IR thermography is used to identify BL streaks and vortices caused by the steady force offset of the individual PA electrodes of the array in section 7.1. The capacitive coupling in the electric setup of the PA array and its effect on the transfer paths is described in section 7.2. Although the influencing factors are identified and the setup is optimized, the capacitive coupling still has a non-negligible effect on the secondary transfer path. in the laminar BL as discussed in section 7.3. Concluding remarks summarise the results of the investigations with the PA array in section 7.4.

7.1. Vortex Identification by IR Thermography

The base flow on the flat plate is already extensively investigated for the 2D case in Chapter 4 and Chapter 5. The steady, downstream directed force of each individual PA in the array introduces a spanwise modulation of the u -velocity component in the BL that can likely generate vortices or streaks. Quantitative measurements of the velocity fields with stereo PIV are not conducted here because only a small FOV can be covered (Barckmann et al. (2015)). In addition, image correlation and traversing the measurement equipment is time consuming. Therefore, the effects of the steady PA forcing on the BL development are investigated with IR thermography, which allows fast

measurements with a high spatial resolution and low experimental effort.

The heated surface downstream of the PA array (Fig. 3.10) allows for measuring of difference in heat transfer at the flat plate surface with an IR camera. Hence, laminar-turbulent transition, vortices and BL streaks can be identified in the following qualitative analysis of the IR images.

Figure 7.1 shows the dewarped IR images, normalized with the fully turbulent flow case. For more information about the dewarping procedure and the normalization technique, please refer to Simon et al. (2016c). The surface is heated with an IR heater from above (Fig. 3.10) but only the foil covered foam ($x > 454$ mm) delivers a good signal for the IR measurements. Red regions indicate higher surface temperatures and lower heat transfer while blue regions stand for lower surface temperatures and increased heat transfer. The heater is centered at $z \approx 100$ mm and aligned in streamwise direction. Therefore, the surface is not sufficiently heated in the region of -50 mm $> z > -100$ mm and the change in heat transfer cannot be detected. Nonetheless, the effects caused by the centered PA₃ ($z = 0$ mm) can be observed well.

The reference case without PA or DS operation at $U_{WT} = 12$ m/s is shown in Fig. 7.1(a). All PA electrodes, except the centered PA₃, are covered with one layer of polyimide tape to avoid any generation of plasma or volume force. The PA electrodes can be observed in the IR image at $x_c = 364$ mm and the surface hot-wires appear as heated dots at $x = 409$ mm. The flow behind the PA array is laminar for the reference case, indicated by the red color.

For the following investigation, PA₃ is operated in steady operation mode at different operating voltage amplitudes V_{pp} . The PA electrode edges are rounded to fade out the force and avoid an abrupt change in spanwise direction. Nevertheless, vortices can be generated at the edges. If PA₃ is operated in steady operation mode at $V_{pp} = 7.5$ kV (Fig. 7.1(b)), two streaky structures arise from the edges of PA₃ downstream ($z \approx \pm 25$ mm). The structures are hardly visible in the IR image and do not significantly influence the BL transition in the considered region.

Operating PA₃ at $V_{pp} = 9$ kV leads to the generation of two distinct vortices that are clearly visible in the IR image in Fig. 7.1(c). The integral PA force F_x is related to V_{pp} by $F_x \sim V_{pp}^{7/2}$ for a 2D actuator. Finite amplitude streaks can stabilize the laminar BL (Barckmann et al. (2015); Shahinfar et al. (2014)). In this case, the spanwise extend and amplitude of the vortices de-stabilize the BL and a breakdown to turbulence occurs as indicated by the yellow wedge,

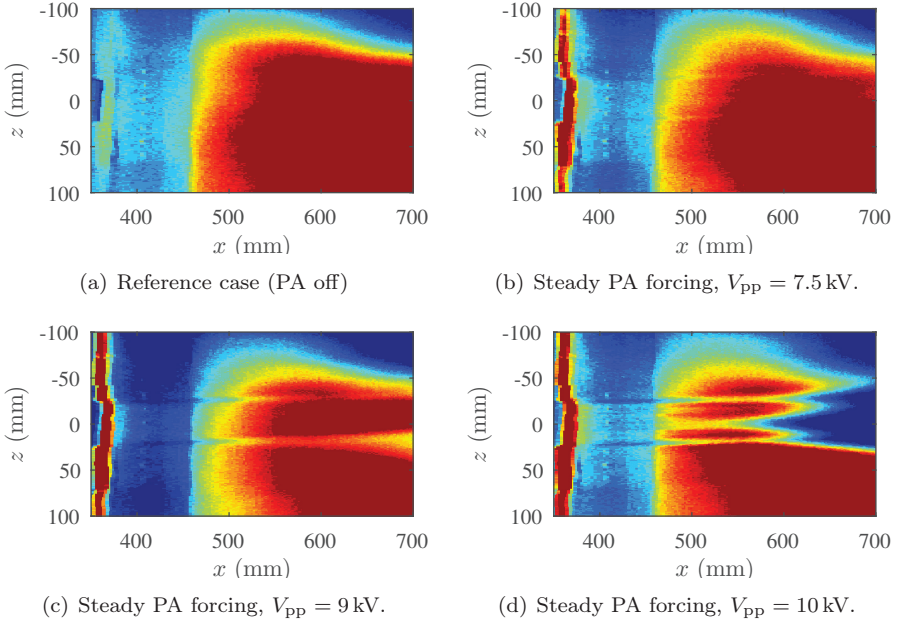


Figure 7.1.: IR images of the flat plate surface with different steady PA operating voltage amplitudes V_{pp} for the centered PA_3 at $U_{WT} = 12 \text{ m/s}$.

developing at $x \approx 650 \text{ mm}$, $z \approx 25 \text{ mm}$. An increase of the PA amplitude to $V_{pp} = 10 \text{ kV}$ leads to even stronger vortices as shown in Fig. 7.1(d). The vortices can be identified well from the IR image but do not lead to a turbulent wedge initially. The transition to turbulence is moved to $x \approx 600 \text{ mm}$ in the centered region, whereas the BL stays laminar in the remaining area.

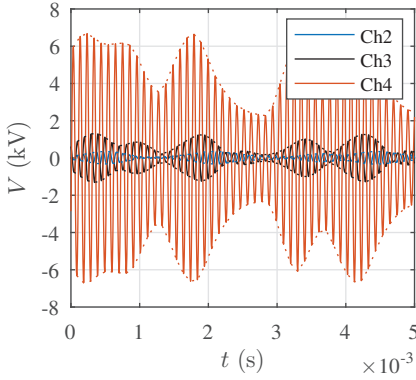
In conclusion, the localized steady forcing of the PA does not significantly influence the BL at a low amplitude of $V_{pp} = 7.5 \text{ kV}$. This is consistent with the 2D experiments with only one spanwise 2D PA in Chapters 4 and 5. At higher V_{pp} , vortices are generated at the edges of the electrodes and premature transition occurs. The hybrid PA operation mode (Kurz et al. (2013)) with a relatively high steady force offset ($V_{pp} > 8 \text{ kV}$) is therefore not a promising operation mode to delay natural transition with this PA array configuration.

7.2. Coupling of Transfer Paths in the Plasma Actuator Array Setup

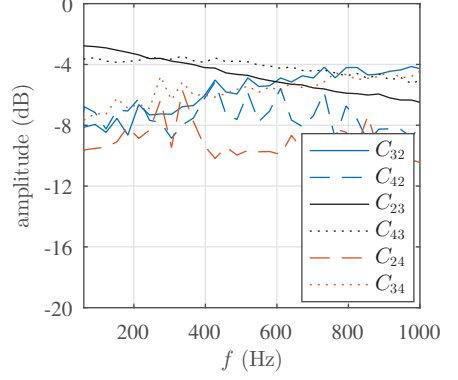
The operating frequency of $f_{PA} \approx 10$ kHz requires relatively large HV generators like the Minipuls 0.2-5. Because the HV generators cannot be integrated in the flat plate surface, the cables are lead individually to each PA electrode. Restrictions of the flat plate model and limited space in the cable ducts of the wind tunnel require a parallel guidance of the HV cables. As mentioned in section 3.4, the capacitive coupling is a potential issue that is discussed in the following. The coupling in the multi-channel HV generator itself is investigated in section 7.2.1 and the influence of the HV cables in section 7.2.2. In addition, the impact of the capacitive coupling on the secondary transfer paths is discussed in section 7.2.3. Finally, the potential of the PA array for future applications is discussed in section 7.2.4.

7.2.1. Capacitive Coupling in the High-voltage Generator

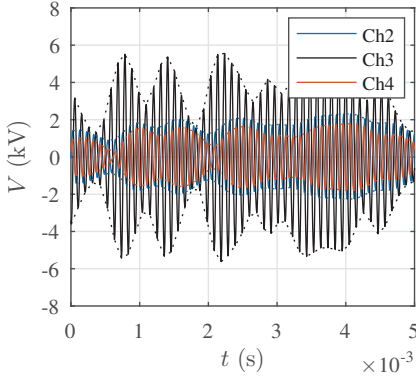
The capacitive coupling of the different channels in the Minipuls 0.2-5 HV generator itself is tested by operating the HV generator without PAs but only three HV probes, Pintek HVP-39pro, connected to Ch2-4. The input signal ζ and the signals of the three HV probes are simultaneously sampled with a Picoscope 4424 A/D converter at $f_S = 1$ MHz. Figure 7.2(a) exemplarily shows the time trace of the high voltage signals, generated by an PRBS input signal $\zeta_4 = 0.6 + 0.3$ for Ch4 ($\zeta_2 = \zeta_3 = 0$). The envelope (dotted line) represents the force variation in time. The time traces already indicate a coupling of the channels but a more detailed information can be obtained with the Bode diagram in Fig. 7.2(b,d). It shows the transmission behavior between the envelopes of the different channels, while C_{24} describes the impact on Ch2, caused by Ch4 (to Ch2, from Ch4). The transmission behavior is not symmetric ($C_{34} \neq C_{43}$) for the whole frequency band. Except C_{23} and C_{43} , all lines are close to -7 dB in the amplitude response in Fig. 7.2(b). If PA₃ is operated, the impact on the neighboured channels is ≈ 4 dB higher (C_{23} , C_{43}). This is also visible in the time trace that is exemplarily presented in Fig. 7.2(c).



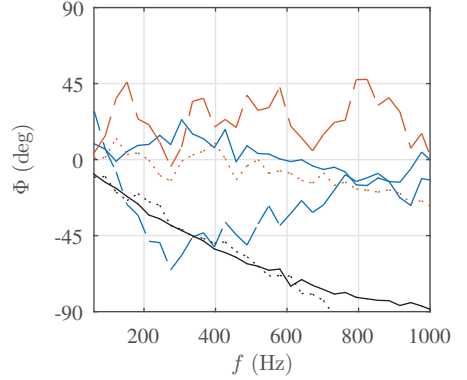
(a) Time traces of the HV signals for input signals $\zeta_2 = \zeta_3 = 0$, $\zeta_4 = 0.6 + 0.3j$.



(b) Amplitude response.



(c) Time traces of the HV signals for input signals $\zeta_2 = 0$, $\zeta_3 = 0.6 + 0.3j$, $\zeta_4 = 0$.



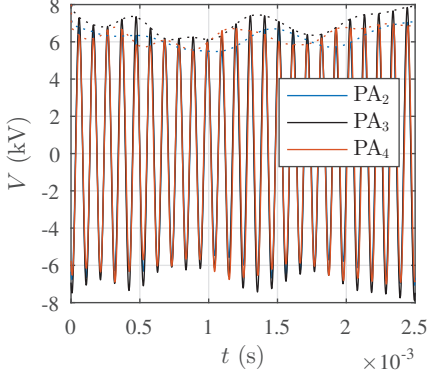
(d) Phase response.

Figure 7.2.: Capacitive coupling of the HV generator channels. The input voltage ζ is only applied for one channel. (a,c) Exemplary HV signals of Ch2-Ch4, generated by the HV generator and measured with HV probes; no PAs are connected. (b,d) Bode diagram of the coupling of different HV generator channels.

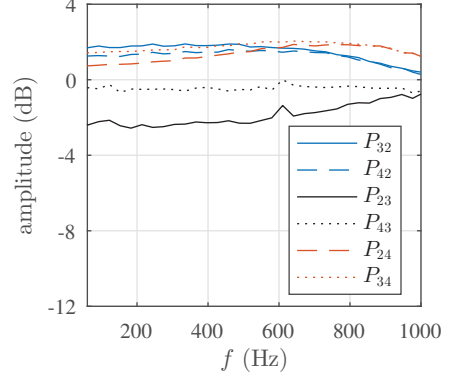
7.2.2. Capacitive Coupling of the Plasma Actuator Array

The coupling of the individual PA electrodes is of importance for the application of the PA array for the flow control approach. Therefore, two cabling configurations, config.I and config.II are tested, cf. Fig. 3.7. The multi-channel HV generator device was designed in a way that the driving signals of all channels run in phase at the operating frequency f_{PA} , if a load (PA) is attached to avoid sparking between the electrodes. The time traces for config.I in Fig. 7.3(a) show exactly this behavior but also a coupling of the operating voltage between the different PAs. Only Ch4 of the HV generator is supplied with a PRBS signal $\zeta_4 = 0.6 + 0.3$, while the other two input signals are set to a constant offset $\zeta_2 = \zeta_3 = 0.6$. The offset is required to avoid sparking between the upper electrodes due to a high potential difference. The coupling of the channels increases significantly compared to the measurements with only HV probes attached and the amplitude response in Fig. 7.3(b) even shows values above zero. Corresponding to the nomenclature in section 7.2.1, the transfer function between the envelope of the HV signals to PA₄ from PA₃ is called P_{43} . Hence, the close parallel guidance of the cables leads to a strong capacitive coupling and should be avoided. The setup with config.II (Fig. 3.7(b)) overcomes this problem by guiding the cables as far as possible from each other. The time trace of the HV signals (Fig. 7.3(c)) and the amplitude response (Fig. 7.3(d)) show much less coupling between the channels.

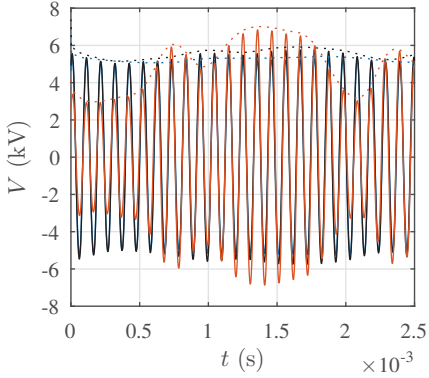
The amplitude response can be significantly reduced by ≈ 10 dB, if the cables are guided to each PA individually with a maximum spacing as it is done for the PA array config.II. The amplitude responses in Fig. 7.3(d) with PA array do look very similar to the curves in Fig. 7.2(b), where only HV probes are attached to the HV generator. The higher values of C_{23} and C_{43} in Fig. 7.2(b) are probably caused by additional capacitive coupling of the HV probe cables.



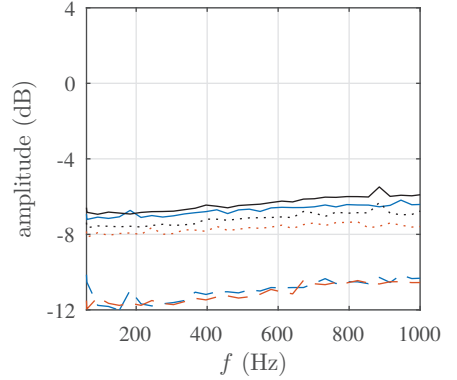
(a) Time traces of the HV signals, config I. Input signals: $\zeta_2 = \zeta_3 = 0.6$, $\zeta_4 = 0.6 + 0.3$.



(b) Amplitude response, config. I.



(c) Time traces of the HV signals, config II. Input signals: $\zeta_2 = \zeta_3 = 0.6$, $\zeta_4 = 0.6 + 0.3$.



(d) Amplitude response, config. II.

Figure 7.3.: Capacitive coupling of the PA electrodes in the array for two different PA array configurations.

7.2.3. Coupling of the Secondary Paths

The capacitive coupling of the PA electrodes can be significantly reduced with the PA array config. II, but not be avoided. In the following, the impact of the coupling on the secondary paths G_{lm} (to error sensor e_l , from PA_m) is investigated. The dotted lines in Fig. 7.4 show the transmission behavior for config. II with no electrodes covered, i.e. plasma is generated at all electrodes (reference case). The PAs are operated at the same mean amplitude V_{pp} but only PA_3 is intended to be modulated in time ($\zeta_2 = \zeta_4 = 0.6$, $\zeta_3 = 0.6 + 0.3$). The amplitude response in Fig. 7.4(a) shows that the secondary path G_{33} (to e_3 , from PA_3) is 5 dB to 7 dB higher in amplitude compared to G_{23} and G_{43} for the reference case (dotted lines). Physically, this is consistent as the generated wave package spreads in spanwise direction while traveling downstream (Erb (2002); Semeraro and Pralits (2017)). This is also the case here, but the recorded secondary paths (dotted lines) might be erroneous due to the capacitive coupling of the individual PAs. To check this hypothesis, the electrodes of PA_2 and PA_4 are partly covered with one layer of polyimide tape (thickness 0.06 mm) to avoid the plasma generation. The results with covered electrodes are presented as solid lines in Fig. 7.4. The FIR filter as well as the Bode diagram show significantly reduced amplitudes of the secondary path as well as a different phase of the waves that are generated by PA_3 . The waves only have a low impact on error sensors e_2 and e_4 . The low signal amplitude (and coherence) in the band of $160 \text{ Hz} < f < 200 \text{ Hz}$ leads to jumps in the phase response that are not related to any physical meaning.

In conclusion, the real secondary path can only be recorded with (partly) covered electrodes. Otherwise the neighbored error sensors also measure the waves generated unintentionally by another PA of the array.

7.2.4. Potential for Future Applications

The optimization of the cable guidance and the PA array design can significantly reduce the coupling between the actuators but not prevent erroneous secondary paths. These erroneous paths lead to an unstable MIMO fxLMS controller and do not allow AWC of 3D disturbances in the laminar BL.

In order to avoid the coupling, the HV generators should be distributed and placed directly below the upper PA electrode. With the available multi-

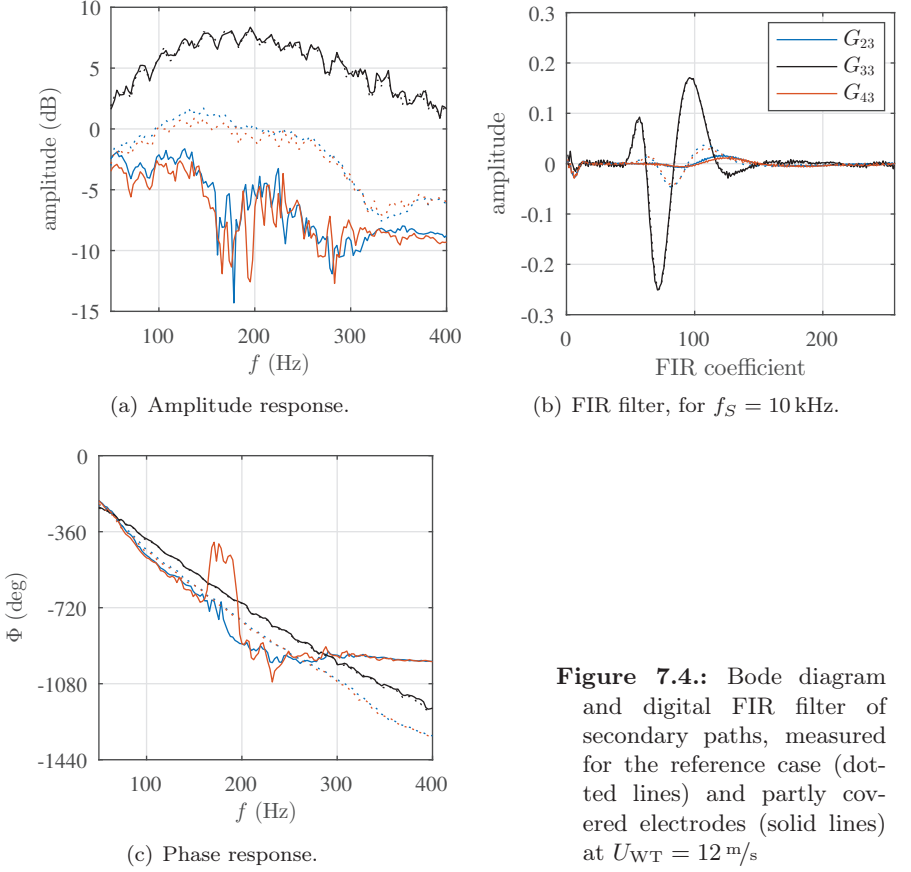


Figure 7.4.: Bode diagram and digital FIR filter of secondary paths, measured for the reference case (dotted lines) and partly covered electrodes (solid lines) at $U_{WT} = 12 \text{ m/s}$

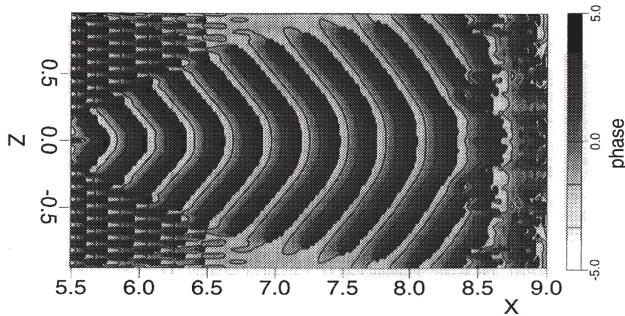


Figure 7.5.: TS-wave disturbances, developing from a point disturbance source in a flat plate BL, Stemmer et al. (1998).

channel HV generator (Minipuls 0.2-5), the implementation of the HV transformer cascades in the flat plate model is not feasible and would not solve the problem as the coupling occurs because of the proximity of the transformer cascades, cf. Fig. 3.7. Smaller HV transformers (e.g. the Heraeus trigger transformer NL-105) could be applied directly beneath the PA electrode but the operating frequency f_{PA} , which has to be close to the eigenfrequency of the electric circuit, rises from $f_{PA} \approx 10 \text{ kHz}$ to $f_{PA} \approx 100 \text{ kHz}$. Hence, the corresponding steady PA force F_x is 10 times higher, too. The higher steady force would cause vortices at the edges of the electrodes and lead to premature transition, cf. Fig. 7.1. In addition, the higher f_{PA} would increase the parasitic current I_{pc} as indicated by the term dV/dt in (3.3).

In the following, the transmission paths recorded with (partly) covered electrodes are investigated. Future investigation with PA arrays require a solution for the issues discussed above. Otherwise, the PA cannot be applied for the cancellation of natural TS-waves as they occur in 3D wave packages.

7.3. Transmission Behavior of the Generated Waves.

The propagation properties and the transmission behavior of the waves for the 3D case differ from the artificially 2D TS-waves that have been investigated in Chapters 4, 5 and 6. Similar to the pointwise induced disturbances that are

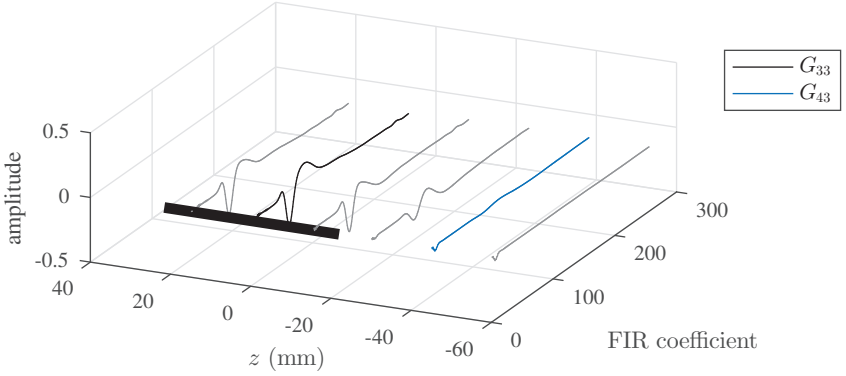


Figure 7.6.: Secondary paths, related to PA₃ and measured at $U_{WT} = 12 \text{ m/s}$. The paths to additional (temporarily installed) error sensors are shown as gray lines.

depicted in Fig. 7.5, the waves generated by the PA array and the DS propagate with a bent wavefront and spread with a certain angle Θ . In the following, the propagation behavior of the artificially generated waves is discussed for the PA array (section 7.3.1) and the disturbance source (section 7.3.2).

7.3.1. Counter-waves Generated by the Plasma Actuator

Despite the capacitive coupling, discussed in section 7.2, partly covered electrodes enable the investigation of the waves that are propagating from one single PA of the array. Figure 7.6 shows the FIR filters of the secondary paths that are related to PA₃. The black bar indicates the upper electrode of PA₃. The data of G_{33} and G_{43} are taken from Fig. 7.4(b). Additional sensors with a narrower spacing ($\Delta z = 15 \text{ mm}$) allow for more precise investigation of the generated waves. As the FIR filter describes the impulse response, the 3D plot in Fig. 7.6 illustrates the propagation behavior nicely. The three sensors downstream of the PA electrode show almost the same behavior. Hence, an even wavefront can be assumed just downstream of the electrode. The sensor mounted at $z = -30 \text{ mm}$ shows a reduced amplitude but clear influence of PA₃, while G_{43} and the most outside positioned sensor ($z = -60 \text{ mm}$) are not considerably affected.

7.3.2. Waves Generated by the Disturbance Source

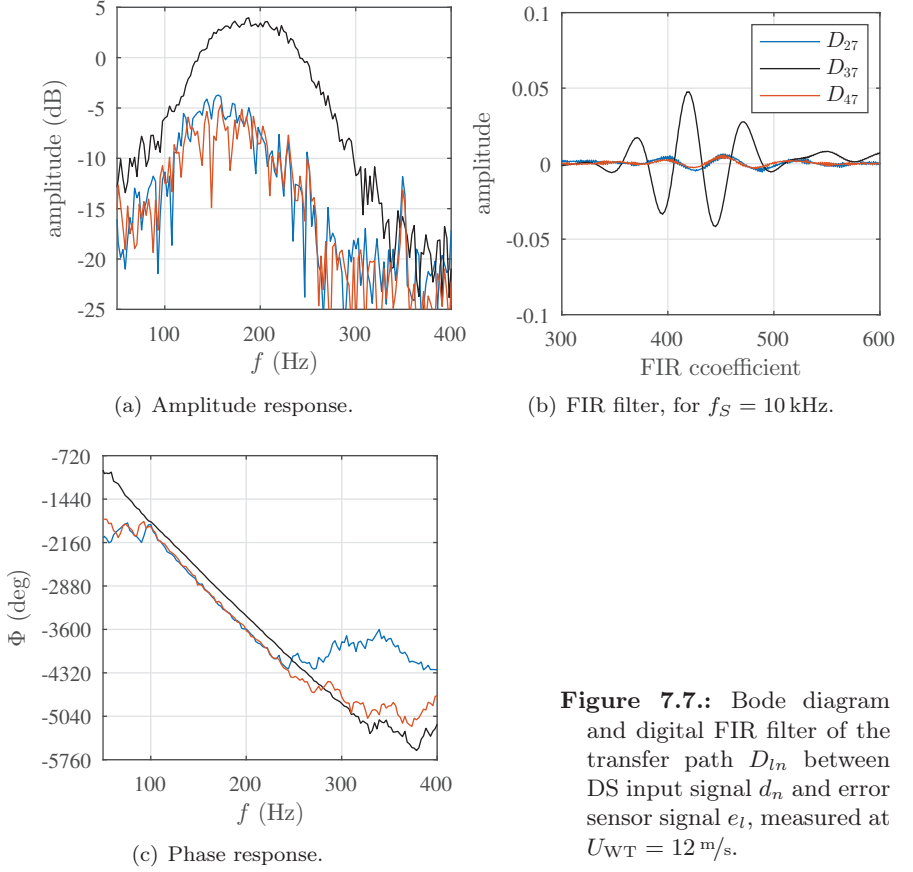
Compared to the waves described above, the waves that are generated by the DS travel a longer distance before they reach the error sensors e_l . This leads to an increased damping of the amplitude besides the TS-wave hump, cf. Fig. 7.7(a). The transfer function D_{37} indicates the transfer path to error sensor e_3 , from DS channel d_7 , which is centered on the flat plate ($z = 0$ mm). Sensor e_3 and d_7 are aligned in streamwise direction and the symmetric propagation behavior ($D_{27} \approx D_{47}$) supports this hypothesis. Similar to the PA generated waves (Fig. 7.4), the edges of the wavefront are bent and the phase response of the error sensors e_2 and e_4 in Fig. 7.7(c) is shifted by $\Delta\Phi \approx 240^\circ$ in the amplified frequency band ($100 \text{ Hz} < f < 250 \text{ Hz}$). This is consistent with the phase shift shown in Fig. 7.5. The geometric angle between d_7 and e_2 is $\Theta \approx 14^\circ$ and agrees well with the DNS calculations of the flat plate flow by Stemmer et al. (1998).

7.4. Conclusions

A plasma actuator array has been tested in a flat plate setup with the goal to attenuate 3D TS-wave disturbances in a laminar boundary layer and delay natural laminar-turbulent transition. An important finding is that a sufficiently low amplitude offset V_{pp} does not lead to unstable vortices at the PA electrode edges due to a spanwise force modulation. Higher V_{pp} can cause vortices that lead to premature transition but PA array operation at higher Re would reduce that effect.

A bigger issue is the capacitive coupling of the different PA channels in the array. The investigations showed that the coupling can be reduced an optimal cable guidance but even the reduced coupling does have a significant effect on the secondary paths. The coupling unintentionally generates counter-waves at the neighboured actuators and does not allow for stable MIMO controller operation.

The potential of future applications for AWC of 3D natural TS-wave disturbances has been discussed above but technical obstacles remain. Despite the issues discussed above, the acquired transfer path with covered electrodes allow for investigating future MIMO controller operation, which is done with an outlook in appendix B.



8. Conclusions and Outlook

Re-active laminar flow control has been investigated in this thesis with the overall goal of delaying natural laminar-turbulent transition by active cancellation of TS-waves with a DBD plasma actuator array. This goal could not be conclusively achieved due to EMC problems between the individual PAs. Nonetheless, many steps on the way to reach the overall goal have been successfully investigated in experimental studies, supported by numerical simulations.

The main questions, addressed in section 1.3, have been answered with fundamental experiments in a zero pressure gradient flat plate BL but also in a realistic environment on a manned glider in flight under varying inflow conditions. In the following, the questions mentioned above are discussed and an outlook for future research is given.

Active wave cancellation: How exactly do the counter-waves, generated by the PA, interact with the TS-wave disturbances in the boundary layer? (Chapter 4)

For the first time, phase-averaged PIV measurements have been conducted in the laminar BL in direct vicinity of a PA, operated in AWC mode. The interaction between the oncoming disturbance and the counter-waves can be observed well from the acquired velocity fields.

The cancellation process does not happen directly at the actuator but some distance downstream. The generated counter-waves do not have TS-wave character immediately but travel downstream and develop to a TS-wave by changing the shape and wavelength.

Are model-based control algorithms (e.g. LQG) or adaptive algorithms (e.g. fxLMS) better suited for active wave cancellation in terms of performance and controller stability? (Chapter 5)

A comparison of model-based (LQG) and adaptive (fxLMS) control algorithms for the AWC approach has been performed in a flat-plate experiment at different wind-tunnel speeds. Even if it showed very important in the first steps of the TS-wave control, the results with the model-based control approach demonstrated that optimality has been overemphasised in the past. The adaptive control algorithm performs equally well and even better for off-design operation. In terms of controller stability under variable inflow conditions and robustness against modelling errors, the adaptive character of the fxLMS makes it more suitable for real applications.

What are the implications for the controller stability under more realistic, varying inflow conditions in flight? (Chapter 6)

A flight setup has been developed to investigate and evaluate AWC of artificially generated 2D TS-waves on a manned glider. The in-flight experiments lift the flow-control approach on a higher technological level at relevant Reynolds numbers under more realistic (varying) inflow conditions. Issues that would not have been investigated by wind-tunnel experiments or numerical simulations (DNS) independently are implied due to the in-flight experiments. The inflow parameters vary during flight and therefore also the transfer paths of the controlled system that may lead to an unstable controller behavior. The application of the adaptive delayed-x-LMS control algorithm and its further development to a “black box” approach overcomes the problem of changing transfer paths because the algorithm is automatically adapting to the new situation.

How can naturally occurring TS-wave dominated transition be controlled with an array of spanwise arranged plasma actuators? What are the challenges of applying AWC to this transition scenario? (Chapter 7)

The question concerning the challenges of the application of DBD plasma actuator arrays can be clearly answered. Despite the optimization of the setup,

the capacitive coupling of the PAs in the array is a critical factor that does not allow the application of a PA array with this setup. Coupled actuators in the array lead to coupled secondary paths that cause an unstable controller behavior.

Outlook

All investigations that are discussed above dealt with artificially generated, mostly 2D, disturbances. The approach with the disturbance source allows for testing algorithms and actuators under controlled conditions, which are close to reality. Despite the scientific issues that have been investigated in this thesis, there are remaining questions that should be answered in future. In the following, an outlook is given regarding the development of DBD plasma actuators and active cancellation of naturally occurring TS-waves. The thesis is closed with some general thoughts on (re-)active flow control.

DBD Plasma Actuator Development

Prior to the investigations made in this thesis, the low fluid-dynamic efficiency, low momentum input and the limited durability were the main problems concerning the DBD PA. These issues are still present and only the durability problem has partly been solved by other researchers who used ceramic/glass dielectric materials. The capacitive coupling is now added to the list but the high voltage and unsteady discharge processes caused EMC problems before. One important result is that spanwise DBD PA arrays could not be used to delay natural laminar-turbulent transition due to this EMC problems.

The biggest advantage of the PA - no moving parts - avoids mechanical coupling, but the coupling problem in general has not been avoided by using this kind of actuator. New designs or operation modes for the DBD PA could overcome this problem in future. The poor fluid-dynamic efficiency could be increased by operating the DBD PA in direct frequency mode for AWC. This would allow to benefit from the unsteady force generation at the time scale of the PA operating frequency. The proof of concept was shown by Kurz et al. (2012) for artificially generated single-frequency 2D disturbances but the attenuation of broad-band 3D TS-waves would require the devel-

opment of a new generation of multi-channel HV generators. Nonetheless, capacitive coupling could be an even bigger issue, if the operating frequency of the PA electrodes is not in phase.

The DBD PA was intensively used for fundamental research on flow control for the last two decades, but its application has never left the lab - there might be a reason. Despite its limitations, it can be an excellent actuator to investigate different flow-control approaches in general. Fabbiane (2016) and Semeraro et al. (2013) stated that not the actuator is of importance, but its effect. The PIV experiments in Chapter 4 showed that the PA does not generate a counter-wave initially and the shape of the forcing might not be as important for the counter-wave generation. Experiments on AWC with other actuator types have been conducted successfully and the role of the actuator was probably overestimated in the past.

In the end, system integration is the critical factor for a flow control technology and this point is addressed in the following.

Active Wave Cancellation: Technological Issues

Active wave cancellation is a promising technology, if the related technological issues can be handled. The effect of an impulse introduced to the flow by an actuator can be multiplied by a power gain Γ , if an advantage of the receptivity of the flow on that actuation is taken. Often small perturbations can significantly influence the flow around a body: the transition to turbulence is the best example. The power gain should be used by every flow control approach to make it more energy efficient. The approaches for delaying transition in the laminar BL that have been discussed in this thesis are boundary-layer stabilization and active wave cancellation. Duchmann et al. (2014) only reached a gain of $\Gamma = 50$ with BL stabilization, which is equivalent to an efficiency of $\eta_{\text{eff}} = 5\%$, if the fluid-dynamic efficiency of the PA $\eta_{\text{FM}} = 0.1\%$ is considered. Acting only on small perturbations and taking advantage of the receptivity of the flow instead of changing the mean flow, enables a power gain of up to $\Gamma = 1000$ (Fabbiane et al. (2017)).

Arguments against the AWC technology are mostly the number of required sensors and actuators required on an aircraft wing (Saric (2013)). When talking about “smart surfaces” with future materials/actuators (not necessarily PA) the number of actuators/sensors is actually rather low. A CCD camera

sensor and a plasma screen have a much higher density of sensors/actuators. Besides the actuators/sensors, a stable control system with a rather simple and robust control algorithm is necessary. The dxLMS algorithm with its “black box” approach for online-delay adaption could be one solution. New approaches, like machine learning, might be interesting, but the rather simple relation of controller stability and BL properties that has been investigated thoroughly in this thesis, can be of importance for the design of a system. Future developments on the MIMO control algorithm should try to optimize this approach as discussed in the outlook in appendix B.

(Re-)Active Laminar Flow Control in General

Regardless if wind-tunnel experiments or in-flight experiments are conducted, passive and (re-)active flow control approaches should be investigated under realistic (varying) inflow conditions. Active flow control that is only working optimal under certain conditions is static and therefore comparable to passive techniques. Smart control algorithms are the key technology to ensure a broader operation range. This approach was taken in this thesis with the adaptive dxLMS “black box” algorithm.

Yet, a clear advantage of active over passive systems has to be shown.

Nomenclature

Small Greek Characters

α	m^2/s	thermal diffusivity
α	—	step size of the LMS algorithm
α	deg	angle of attack
β	deg	sideslip angle
δN	samples	resolution of the delay N
δ	m	boundary-layer thickness
$\delta\Phi$	deg	phase-angle resolution
δ_1	m	displacement boundary-layer thickness
δ_1^*	m	δ_1 at the beginning of the domain
δ_2	m	momentum boundary-layer thickness
η_{eff}	—	overall efficiency (of the PA)
η_{FM}	—	fluid mechanic efficiency (of the PA)
γ	samples/m	normalized time delay
γ_{xy}^2	—	coherence of the signals x and y
λ_x	m	wavelength in x -direction
λ_z	m	wavelength in z -direction
μ	$\text{Pa} \cdot \text{s}$	dynamic viscosity
ν	m^2/s	kinematic viscosity

ω	1/s	angular frequency
ρ	kg/m ³	density
σ	—	standard deviation
τ	s	time shift
τ_w	N/m ²	wall shear stress
ζ	V	input signal of the HV generator Minipuls

Capital Greek Characters

Δt	s	time between two laser pulses for PIV
ΔT_w	K	difference in wall temperature (laminar-turbulent)
ΔU_{WT}	m/s	change in wind-tunnel speed
Δx_{pr}	m	streamwise distance between position x_p and x_r
Δz	m	spanwise distance between two sensors
$\Delta \Phi$	deg	phase-angle shift
$\Delta \Phi_0$	deg	zero-cross phase
$\Delta \Phi_{TS}$	rad	phase-angle resolution of the PIV measurements
$\Delta \Phi_d$	deg	phase-angle difference
$\Delta \Phi_e$	deg	phase-angle error
$\Delta \Phi_{e,ul}$	deg	phase-angle error at the upper TS-band limit
Λ	—	wing aspect ratio
Φ	deg	phase angle
Φ_{ref}	deg	reference phase-angle
Φ_{TS}	rad	phase angle in the TS-wave cycle
Θ	deg	propagation angle of a TS-wave

Small Roman Characters

a	m/s	sonic speed
b	m	wing span
$c(n)$	V	time discrete output signal of the controller
c_ω	m/s	phase speed
c_f	$-$	local friction coefficient
c_g	m/s	group speed
c_p	$-$	local pressure coefficient
$d(n)$	V	time discrete disturbance source signal
\mathbf{e}	V	vector of L error sensor signals
e'	V	simulated error sensor signal
$e(n)$	V	time discrete error sensor signal
f	Hz	frequency
f_{acq}	Hz	acquisition frame rate of the camera
f_b	Hz	base clock frequency of the digital timer card
f_m	Hz	PA modulation frequency
f_{PA}	Hz	plasma actuator operating frequency
f_S	Hz	sample rate
f_{TS}	Hz	TS-wave frequency
f_x	N/m^3	local PA body force in x -direction
g	m/s^2	gravitational constant
h	$\text{W/m}^2\text{K}$	heat transfer coefficient
\vec{k}	$1/\text{m}$	wavenumber vector

k	$1/\text{m}$	modulus of the wavenumber vector \vec{k}
k_f	W/mK	thermal conductivity coefficient of the fluid
k_x	$1/\text{m}$	(angular) streamwise wavenumber
k_z	$1/\text{m}$	(angular) spanwise wavenumber
$k_{x,i}$	$1/\text{m}$	streamwise disturbance growth rate
l	m	chord length
m	—	number of periods
m	kg	mass
n	—	n -factor, amplification for discrete frequencies
n	—	time discrete sample point
p	Pa	pressure
p'	Pa	pressure fluctuation
$p(n)$	V	time discrete phase-speed sensor signal
p_∞	Pa	far field static pressure
p_{dyn}	Pa	dynamic pressure
\dot{q}_{conv}	W/m^2	convective heat flux (per area)
\hat{q}	m/s	disturbance function amplitude
q'	m/s	disturbance fluctuation
\mathbf{r}	—	vector of K reference sensor signals
$r(t)$	V	reference sensor time signal
s	m	surface layer material thickness
t	s	time
\hat{u}	m/s	amplitude of the velocity fluctuations in x -direction

\vec{u}	m/s	flow velocity vector
u	m/s	flow velocity in x -direction
u'	m/s	flow velocity fluctuations in x -direction
v	m/s	flow velocity in y -direction
v'	m/s	flow velocity fluctuations in y -direction
\mathbf{w}	—	FIR filter coefficient vector
w	—	FIR filter coefficient
x	m	streamwise coordinate
x'	m	streamwise coordinate, $x' = 0$ at the PA position
y	m	wall normal coordinate
z	m	spanwise coordinate

Capital Roman Characters

A_{TS}	—	integral TS-wave amplitude, normalized with U_e
Bi	—	Biot number
C	F	probe-capacitor capacitance
C_{ij}	—	transfer path in the HV generator (to Ch i from Ch j)
C_L	—	global lift coefficient
C_{pc}	F	capacitance, caused by parallel HV cable wiring
D	—	ratio between the RMS of $r(t)$ and U_{WT}
D_{es}	—	transfer path to error sensor e from DS Ch s
E_{max}	dB	maximum error sensor signal reduction
E_{TS}	m ³ /s ²	local perturbation energy of a TS-wave disturbance
F_L	N	lift force

Fo	—	Fourier number
F_x	N/m	integral PA body force in x -direction
\mathbf{G}	—	secondary path matrix of a MIMO system
G_{lm}	—	secondary path of a MIMO system (to l from m)
H_{12}	—	boundary-layer shape factor
\hat{H}_{ec}	—	secondary path model
H_{ec}	—	secondary path
H_{er}	—	primary path
H_{yx}	—	transfer function (to y from x)
I	—	number of FIR coefficients of the compensator \mathbf{W}
I	A	electric current
I	counts	IR camera signal Intensity
I^*	—	normalized IR camera signal Intensity
I_{pc}	A	parasitic current, induced by capacitive coupling
J	—	number of FIR coefficients of the plant \mathbf{G}
K	—	number of reference sensors in z -direction
L	—	number of error sensors in z -direction
L	samples	time discrete lag between two sensor signals
M	—	number of actuators in z -direction
Ma	—	Mach number
N	samples	number of samples
N_{\max}	—	local maximum of the n -factor
N_P	samples	delay, based on the global maximum (peak) of \hat{H}_{ec}

P_{PA}	W	plasma-actuator power
Pr	—	Prandtl number
P_{ij}	—	transfer path between the PAs (to Ch i from Ch j)
Q	C	probe-capacitor charge
R	J/kgK	specific gas constant
Re	—	Reynolds number
Re_1	—	Reynolds number, calculated with δ_1
Re_{crit}	—	critical Reynolds number
Re_{ind}	—	indifference Reynolds number
Re_l	—	chord Reynolds number
Re_x	—	local Reynolds number
S	—	number of disturbance sources
S	m ²	wing surface area
S_{xx}	V ² /Hz	power-spectral density of the signal x
S_{yx}	V ² /Hz	cross-spectral density of the signals x and y
T	s	cylce length
T_∞	K	fluid temperature
T_w	K	wall temperature
Tu	—	turbulence intensity
\tilde{U}	—	flow speed U_∞ , normalized with a reference speed
U	m/s	steady part (mean) of the velocity u
U_∞	m/s	free-stream velocity, flight speed
U_e	m/s	boundary-layer edge velocity

U_{TS}	m/s	integral TS-wave amplitude (at one phase-angle)
$U_{\text{WT, ident}}$	m/s	wind-tunnel speed, at which \hat{H}_{ec} is identified
U_{WT}	m/s	wind-tunnel speed
V_c	V	voltage at the probe capacitor
V_{pc}	V	voltage, induced by capacitive coupling
V_{pp}	V	PA operating voltage amplitude (peak-peak)
\mathbf{W}	—	compensator kernel matrix of a MIMO system
Z	—	controller performance indicator

Shortcuts

2D2C	two-dimensions, two (velocity) components
AWC	active wave cancellation
BL	boundary layer
Ch	channel
CSD	cross-spectral density
DBD	dielectric barrier discharge
DFG	Deutsche Forschungsgemeinschaft
DLR	Deutsches Zentrum für Luft- und Raumfahrt e. V.
DNS	direct numerical simulation
DS	disturbance source
dxLMS	delayed-x-LMS algorithm
EMC	electromagnetic compatibility
exp	experiment
FIR	finite impulse response (filter)

FOV	field of view
fxLMS	filtered-x-LMS algorithm
HLFC	hybrid laminar flow control
HV	high voltage
HW	hot-wire (sensor)
IA	interrogation area
IIR	infinite impulse response (filter)
IR	infra-red
LBA	Luftfahrtbundesamt
LMS	least-mean-squares (algorithm)
LQG	linear-quadratic-gaussian (regulator) algorithm
LST	linear stability theory
MIMO	multiple-input-multiple-output
MPC	model predictive control
NLF	natural laminar flow
PA	plasma actuator
PIV	particle image velocimetry
PSD	power-spectral density
PSE	parabolized stability equations
RMS	root mean square
SISO	single-input-single-output
SNR	signal to noise ratio
TS	Tollmien-Schlichting (waves)

TTL	transistor-transistor logic (signal)
WN	white noise
ZPG	zero pressure gradient

Bibliography

- Amitay, M., Tuna, B. A., and Dell’Orso, H. (2016). Identification and mitigation of T-S waves using localized dynamic surface modification. *Phys. Fluids*, 28(064103).
- Bagheri, S., Brandt, L., and Henningson, D. S. (2009). Input-output analysis, model reduction and control of the flat-plate boundary layer. *J. Fluid Mech.*, 620:263–298.
- Bagheri, S. and Henningson, D. S. (2011). Transition delay using control theory. *Philos. Trans. R. Soc. A-Math. Phys. Eng. Sci.*, 369:1365–1381.
- Barckmann, K., Tropea, C., and Grundmann, S. (2015). Attenuation of Tollmien-Schlichting waves using plasma actuator vortex generators. *AIAA J.*, 53(5):1384–1388.
- Belson, B. A., Semeraro, O., Rowley, C. W., and Henningson, D. S. (2013). Feedback control of instabilities in the two-dimensional Blasius boundary layer: The role of sensors and actuators. *Phys. Fluids*, 25(054106).
- Benard, N. and Moreau, E. (2014). Electrical and mechanical characteristics of surface ac dielectric barrier discharge plasma actuators applied to airflow control. *Exp. Fluids*, 55(11):1846.
- Bewley, T. R. and Liu, S. (1998). Optimal and robust control and estimation of linear paths to transition. *J. Fluid Mech.*, 365:305–349.
- Boermans, L. (2006). Research on sailplane aerodynamics at delft university of technology. *Technical Soaring*, 30(1-2):10–12.
- Boeuf, J., Lagmich, Y., and Pitchford, L. (2009). Contribution of positive and negative ions to the electrohydrodynamic force in a dielectric barrier discharge plasma actuator operating in air. *J. Appl. Phys.*, 106(2), 023115.

- Boiko, A. V., Grek, G. R., Dovgal, A. V., and Kozlov, V. V. (2002). *The origin of turbulence in near-wall flows*. Springer, Heidelberg.
- Borodulin, V., Kachanov, Y., Koptsev, D., and Roschekhtayev, A. (2002). Experimental study of resonant interactions of instability waves in a self-similar boundary layer with an adverse pressure gradient: I. Tuned resonances. *J. Turbul.*, 3:N62.
- Boucinha, V., Jousot, R., Magnier, P., Weber, R., and Leroy-Chesneau, A. (2008). Characterization of the ionic wind produced by a DBD actuator designed to control the laminar-to-turbulent transition. In *Proceedings of the 14th Int Symp on Applications of Laser Techniques to Fluid Mechanics, Lisbon, Portugal*.
- Braslow, A. (1999). *A History of Suction-Type Laminar-Flow Control with Emphasis on Flight Research*. Books Express Publishing.
- Brunton, S. L. and Noack, B. R. (2015). Closed-loop turbulence control: Progress and challenges. *Appl. Mech. Rev.*, 67(5), 050801.
- Brynjell-Rahkola, M. (2015). *Global stability analysis of three-dimensional boundary-layer flows*. Lic. thesis, KTH, Stockholm.
- Cattafesta, L. and Sheplak, M. (2011). Actuators for active flow control. *Annu. Rev. Fluid Mech.*, 43:247–272.
- Chernyshev, S. L., Gamirullin, M. D., Khomich, V. Y., Kuryachii, A. P., Litvinov, V. M., Manuilovich, S. V., Moshkunov, S. I., Rebrov, I. E., Rusyanov, D. A., and Yamshchikov, V. A. (2016). Electrogasdynamic laminar flow control on a swept wing. *Aerosp. Sci. Technol.*, 59:155 – 161.
- Chevalier, M., Schlatter, P., Lundbladh, A., and Henningson, D. S. (2007). A pseudo-spectral solver for incompressible boundary layer flows. Technical Report TRITA-MEK 2007:07, KTH Mechanics, Stockholm, Sweden.
- Corke, T. C., Enloe, C. L., and Wilkinson, S. P. (2010). Dielectric barrier discharge plasma actuators for flow control. *Ann. Rev. Fluid Mech.*, 42:505–529.

- Dadfar, R., Fabbiane, N., Bagheri, S., and Henningson, D. S. (2014). Centralised versus decentralised active control of boundary layer instabilities. *Flow, Turb. and Comb.*, 93(4):537–553.
- Dadfar, R., Hanifi, A., and Henningson, D. S. (2015). Feedback control for laminarization of flow over wings. *Flow, Turb. and Comb.*, 94(1):43–62.
- Dörr, P. C. and Kloker, M. J. (2017). Crossflow transition control by upstream flow deformation using plasma actuators. *J. Phys. D-Appl. Phys.*, 121, 9707.
- Duchmann, A. (2012). *Boundary-layer stabilization with dielectric barrier discharge plasmas for free-flight application*. PhD thesis, Technische Universität Darmstadt.
- Duchmann, A., Grundmann, S., and Tropea, C. (2013). Delay of natural transition with dielectric barrier discharges. *Exp. Fluids*, 54(3):1–12.
- Duchmann, A., Reeh, A., Quadros, R., Kriegseis, J., and Tropea, C. (2010). Linear stability analysis for manipulated boundary-layer flows using plasma actuators. In *Proceedings of the Seventh IUTAM Symposium on Laminar-Turbulent Transition, Stockholm, Sweden, 2009*, pages 153–158. Springer Netherlands.
- Duchmann, A., Simon, B., Tropea, C., and Grundmann, S. (2014). Dielectric barrier discharge plasma actuators for in-flight transition delay. *AIAA J.*, 52(2):358–367.
- Elliott, S. (2000). *Signal processing for active control*. Academic Press, London.
- Erb, P. (2002). *Untersuchung der Grenzschichttransition im Flugversuch*. PhD thesis, Technische Universität Darmstadt.
- Fabbiane, N. (2016). *Transition delay in boundary-layer flows via reactive control*. PhD thesis, KTH, Stockholm.
- Fabbiane, N., Bagheri, S., and Henningson, D. S. (2017). Energy efficiency and performance limitations of linear adaptive control for transition delay. *J. Fluid Mech.*, 810:60–81.

- Fabbiane, N., Semeraro, O., Bagheri, S., and Henningson, D. S. (2014). Adaptive and model-based control theory applied to convectively unstable flows. *Appl. Mech. Rev.*, 66(6), 060801.
- Fabbiane, N., Simon, B., Fischer, F., Grundmann, S., Bagheri, S., and Henningson, D. S. (2015). On the role of adaptivity for robust laminar flow control. *J. Fluid Mech.*, 767:1469–7645.
- Fischer, P., Kruse, J., Mullen, J., Tufo, H., Lottes, J., and Kerkemeier, S. (2008). NEK5000-open source spectral element CFD solver. *Argonne National Laboratory, Mathematics and Computer Science Division, Argonne, IL*, see <https://nek5000.mcs.anl.gov/index.php/MainPage>.
- Gad-el-Hak, M. (2007). *Flow control: passive, active, and reactive flow management*. Cambridge University Press, Cambridge.
- Goldin, N., King, R., Pätzold, A., Nitsche, W., Haller, D., and Woias, P. (2013). Laminar flow control with distributed surface actuation: damping Tollmien-Schlichting waves with active surface displacement. *Exp. Fluids*, 54(3):1–11.
- Grundmann, S. and Tropea, C. (2007). Experimental transition delay using glow-discharge plasma actuators. *Exp. Fluids*, 42:653–657.
- Grundmann, S. and Tropea, C. (2008). Active cancellation of artificially introduced Tollmien-Schlichting waves using plasma actuators. *Exp. Fluids*, 44:795–806.
- Grundmann, S. and Tropea, C. (2009). Experimental damping of boundary-layer oscillations using DBD plasma actuators. *Int. J. Heat Fluid Flow*, 30(3):394–402.
- Hansen, C. (2002). *Understanding active noise cancellation*. Taylor & Francis, New York.
- Hansen, C. and Snyder, S. (2012). *Active control of noise and vibration*. CRC Press, Boca Raton.
- Joslin, R. (1998). Aircraft laminar flow control 1. *Annu. Rev. Fluid Mech.*, 30(1):1–29.

- Jousset, R., Weber, R., Leroy, A., and Hong, D. (2013). Transition control using a single plasma actuator. *International Journal of Aerodynamics*, 3:26–46.
- Juniper, M. P., Hanifi, A., and Theofilis, V. (2014). Modal stability theory lecture notes from the FLOW-NORDITA summer school on advanced instability methods for complex flows, Stockholm, Sweden, 2013. *Appl. Mech. Rev.*, 66(2), 024804.
- Kachanov, Y. (1994). Physical mechanisms of laminar-boundary-layer transition. *Annu. Rev. Fluid Mech.*, 26(1):411–482.
- Kendall, J. (1990). Boundary layer receptivity to freestream turbulence. In *Proceedings of the 21st AIAA Fluid Dynamics, Plasma Dynamics and Lasers Conference*.
- Kim, H.-S. and Park, Y. (1998). Delayed-x LMS algorithm: An efficient ANC algorithm utilizing robustness of cancellation path model. *J. Sound Vibr.*, 212(5):875–887.
- Kotsonis, M. (2015). Diagnostics for characterisation of plasma actuators. *Meas. Sci. Technol.*, 26(9):092001.
- Kotsonis, M., Giepman, R., Hulshoff, S., and Veldhuis, L. (2013). Numerical study of the control of Tollmien–Schlichting waves using plasma actuators. *AIAA J.*, 51(10):2353–2364.
- Kotsonis, M., Shukla, R. K., and Pröbsting, S. (2015). Control of natural Tollmien-Schlichting waves using dielectric barrier discharge plasma actuators. *International Journal of Flow Control*, 7(1-2):37–54.
- Kriegseis, J., Maden, I., Schwarz, C., Tropea, C., and Grundmann, S. (2015). Addendum to ‘velocity-information based force-term estimation of dielectric barrier discharge plasma actuators’. *J. Phys. D: Appl. Phys.*, 48(32), 329401.
- Kriegseis, J., Moeller, B., Grundmann, S., and Tropea, C. (2011). Capacitance and power consumption quantification of dielectric barrier discharge(DBD) plasma actuators. *J. Electrostat.*, 69(4):302–312.

- Kriegseis, J., Schröter, D., Duchmann, A., Barckmann, K., Grundmann, S., and Tropea, C. (2013a). Closed-loop performance control of DBD plasma actuators. *AIAA J.*, 51(4):961–967.
- Kriegseis, J., Schwarz, C., Tropea, C., and Grundmann, S. (2013b). Velocity-information-based force-term estimation of dielectric-barrier discharge plasma actuators. *J. Phys. D: Appl. Phys.*, 46(5), 055202.
- Kriegseis, J., Simon, B., and Grundmann, S. (2016). Towards in-flight applications? A review on DBD-based boundary-layer control. *Appl. Mech. Rev.*, 68(2), 020802.
- Kuhnhehn, M. (2014). Phase-averaged volume force measurements of DBD plasma actuators with particle image velocimetry. Master’s thesis, Technische Universität Darmstadt.
- Kuhnhehn, M., Simon, B., Maden, I., and Kriegseis, J. (2016). Interrelation of phase-averaged volume force and capacitance of dielectric barrier discharge plasma actuators. *J. Fluid Mech.*, 809.
- Kuo, S. M. and Morgan, D. (1995). *Active noise control systems: algorithms and DSP implementations*. John Wiley & Sons, Inc., Hoboken, NJ.
- Kurz, A., Goldin, N., King, R., Tropea, C., and Grundmann, S. (2013). Hybrid transition control approach for plasma actuators. *Exp. Fluids*, 54(11):1–4.
- Kurz, A., Simon, B., Tropea, C., and Grundmann, S. (2014). Active wave cancelation using plasma actuators in flight. In *Proceedings of the 52nd Aerospace Sciences Meeting*. AIAA.
- Kurz, A., Tropea, C., Grundmann, S., Forte, M., Vermeersch, O., Seraudie, A., Arnal, D., Goldin, N., and King, R. (2012). Transition delay using DBD plasma actuators in direct frequency mode. In *Proceedings of the 6th Flow Control Conference*. AIAA.
- Li, Y. and Gaster, M. (2006). Active control of boundary-layer instabilities. *J. Fluid Mech.*, 550:185–206.

- Liepmann, H. and Nosenchuck, D. (1982). Active control of laminar-turbulent transition. *J. Fluid Mech.*, 118:201–204.
- Markus, D. (2016a). Characterization of the Eiffel wind tunnel of the institute SLA. Technical report.
- Markus, D. (2016b). Phase averaged PIV measurements for the investigation of active wave cancelation in a laminar boundary layer. Master’s thesis, Technische Universität Darmstadt.
- Milling, R. W. (1981). Tollmien-Schlichting wave cancellation. *Phys. Fluids*, 24(5):979–981.
- Moore, B. (1981). Principal component analysis in linear systems: Controllability, observability, and model reduction. *IEEE Trans. Autom. Control*, 26(1):17–32.
- Moreau, E. (2007). Airflow control by non-thermal plasma actuators. *J. Phys. D-Appl. Phys.*, 40:605–636.
- Morino, L. and Kuot, C.-C. (1974). Subsonic potential aerodynamics for complex configurations: a general theory. *AIAA J.*, 12(2):191–197.
- Nitsche, W. and Brunn, A. (2006). *Strömungsmesstechnik*. Springer Verlag, Heidelberg.
- Nordström, J., Nordin, N., and Henningson, D. (1999). The fringe region technique and the fourier method used in the direct numerical simulation of spatially evolving viscous flows. *SIAM J. Sci. Comp.*, 20(4):1365–1393.
- Opfer, H. (2002). *Active cancellation of 3D Tollmien-Schlichting waves in the presence of sound and vibrations*. PhD thesis, Georg-August-Universität Göttingen.
- Parikh, P. (2011). Passive removal of suction air for laminar flow control, and associated systems and methods. US Patent 7,866,609.
- Patera, A. T. (1984). A spectral element method for fluid dynamics: laminar flow in a channel expansion. *J. Comput. Phys.*, 54(3):468–488.

- Pätzold, A. (2013). *Experimentelle Untersuchungen aktiv ausgelenkter Oberflächen zur Reduktion der Wandreibung durch Transitionsverzögerung*. PhD thesis, TU Berlin.
- Peltzer, I., Pätzold, A., and Nitsche, W. (2009). In-flight experiments for delaying laminar-turbulent transition on a laminar wing glove. *Proc. Inst. Mech. Eng. Part G-J. Aerosp. Eng.*, 223(6):619–626.
- Reeh, A. (2014). *Natural laminar flow airfoil behavior in cruise flight through atmospheric turbulence*. PhD thesis, Technische Universität Darmstadt.
- Reeh, A. and Tropea, C. (2015). Behaviour of a natural laminar flow aerofoil in flight through atmospheric turbulence. *J. Fluid Mech.*, 767:394–429.
- Roth, J., Sherman, D., and Wilkinson, W. (1998). Boundary layer flow control with a one atmosphere uniform glow discharge surface plasma. In *Proceedings of the 36th Aerospace Sciences Meeting*. AIAA.
- Roth, J., Sherman, D., and Wilkinson, W. (2000). Electrohydrodynamic flow control with a glow-discharge surface plasma. *AIAA J.*, 38(7):1166–172.
- Saric, W. (2013). On why active cancellation does not work. Personal communication letter.
- Saric, W. S., Reed, H. L., and Kerschen, E. J. (2002). Boundary-layer receptivity to freestream disturbances. *Annu. Rev. Fluid Mech.*, 34:291–319.
- Schlichting, H. and Gersten, K. (2000). *Boundary-layer theory*. Springer, Heidelberg.
- Schmid, P. J. and Henningson, D. S. (2012). *Stability and transition in shear flows*. Springer, New York.
- Schmid, P. J. and Sipp, D. (2016). Linear control of oscillator and amplifier flows. *Phys. Rev. Fluids*, 1:040501.
- Schrauf, G. (2004). The need of large-scale HLFC testing in Europe. *AFLoNext project*.
- Semeraro, O., Bagheri, S., Brandt, L., and Henningson, D. S. (2013). Transition delay in a boundary layer flow using active control. *J. Fluid Mech.*, 731(9):288–311.

- Semeraro, O. and Pralits, J. O. (2017). Full-order optimal compensators for flow control: the multi-input case. *J. Fluid Mech.*, (submitted).
- Shahinfar, S., Sattarzadeh, S. S., and Fransson, J. H. (2014). Passive boundary layer control of oblique disturbances by finite-amplitude streaks. *J. Fluid Mech.*, 749:1–36.
- Simon, B., Fabbiane, N., Nemitz, T., Bagheri, S., Henningson, D. S., and Grundmann, S. (2016a). In-flight active wave cancelation with delayed-x-LMS control algorithm in a laminar boundary layer. *Exp. Fluids*, 57(10):1–16.
- Simon, B., Filius, A., Tropea, C., and Grundmann, S. (2016b). IR thermography for dynamic detection of laminar-turbulent transition. *Exp. Fluids*, 57(5):1–12.
- Simon, B., Nemitz, T., Rohlfing, J., Fischer, F., Mayer, D., and Grundmann, S. (2015). Active flow control of laminar boundary layers for variable flow conditions. *Int. J. Heat Fluid Flow*, 56:344–354.
- Simon, B., Schnabel, P., and Grundmann, S. (2016c). IR measurements for quantification of laminar boundary layer stabilization with DBD plasma actuators. In *New Results in Numerical and Experimental Fluid Mechanics X*. Springer International Publishing Switzerland.
- Snyder, S. and Hansen, C. (1990). The influence of transducer transfer functions and acoustic time delays on the implementation of the LMS algorithm in active noise control systems. *J. Sound Vibr.*, 141(3):409–424.
- Snyder, S. D. and Hansen, C. H. (1994). The effect of transfer function estimation errors on the filtered-x LMS algorithm. *IEEE Trans. Signal Process.*, 42(4):950–953.
- Snyder, S. D. and Tanaka, N. (1997). Algorithm adaptation rate in active control: Is faster necessarily better? *IEEE Trans. Speech Audio Process.*, 5(4):378–381.
- Spurk, H. and Aksel, N. (2006). *Strömungslehre*. Springer, Berlin.

- Stemmer, C., Kloker, M., and Wagner, S. (1998). DNS of harmonic point source disturbances in an airfoil boundary layer flow. In *Proceedings of the 29th AIAA Fluid Dynamics Conference*.
- Sturzebecher, D., Anders, S., and Nitsche, W. (2001). The surface hot wire as a means of measuring mean and fluctuating wall shear stress. *Exp. Fluids*, 31(3):294–301.
- Sturzebecher, D. and Nitsche, W. (2003). Active cancellation of Tollmien-Schlichting instabilities on a wing using multi-channel sensor actuator systems. *Int. J. Heat Fluid Flow*, 24:572–583.
- Thomas, A. S. (1983). The control of boundary-layer transition using a wave-superposition principle. *J. Fluid Mech.*, 137:233–250.
- Turkac, Y. (2016). Analysis of a dxLMS control algorithm for active wave cancellation in a laminar boundary layer with linear stability theory. Bachelor’s thesis, Technische Universität Darmstadt.
- van Ingen, J. (2008). The e^N method for transition prediction. Historical review of work at TU Delft. In *Proceedings of the 38th AIAA Fluid Dynamics Conference and Exhibit*. AIAA.
- Vollmer, M. and Möllmann, K.-P. (2010). *Infrared thermal imaging: fundamentals, research and applications*. John Wiley & Sons, Weinheim.
- Wang, J.-J., Choi, K.-S., Feng, L.-H., Jukes, T. N., and Whalley, R. D. (2013). Recent developments in DBD plasma flow control. *Prog. Aeosp. Sci.*, 62:52–78.
- Weismüller (2012). *A new approach to aerodynamic performance of aircraft under turbulent atmospheric conditions*. PhD thesis, Technische Universität Darmstadt.
- White, F. (1974). *Viscous fluid flow*. McGraw-Hill, New York.
- Wicks, M., Thomas, F. O., Corke, T. C., Patel, M., and Cain, A. B. (2015). Mechanism of vorticity generation in plasma streamwise vortex generators. *AIAA J.*, 53(11):3404–3413.

- Widmann, A. (2010). Developing a method for phase-averaged particle image velocimetry measurements in boundary-layer flows. Master's thesis, Technische Universität Darmstadt.
- Widmann, A., Duchmann, A., Kurz, A., Grundmann, S., and Tropea, C. (2012). Measuring Tollmien-Schlichting waves using phase-averaged particle image velocimetry. *Exp. Fluids*, 53(3):707–715.
- Widmann, A., Kurz, A., Simon, B., Grundmann, S., and Tropea, C. (2013). Characterization of the interaction between Tollmien-Schlichting waves and a DBD plasma actuator using phase-locked PIV. In *Proceedings of PIV13; 10th International Symposium on Particle Image Velocimetry*. Delft University of Technology.
- Zhang, M., Lan, H., and Ser, W. (2003). A robust online secondary path modeling method with auxiliary noise power scheduling strategy and norm constraint manipulation. *IEEE Trans. Speech Audio Process.*, 11(1):45–53.

A. Additional PIV Results

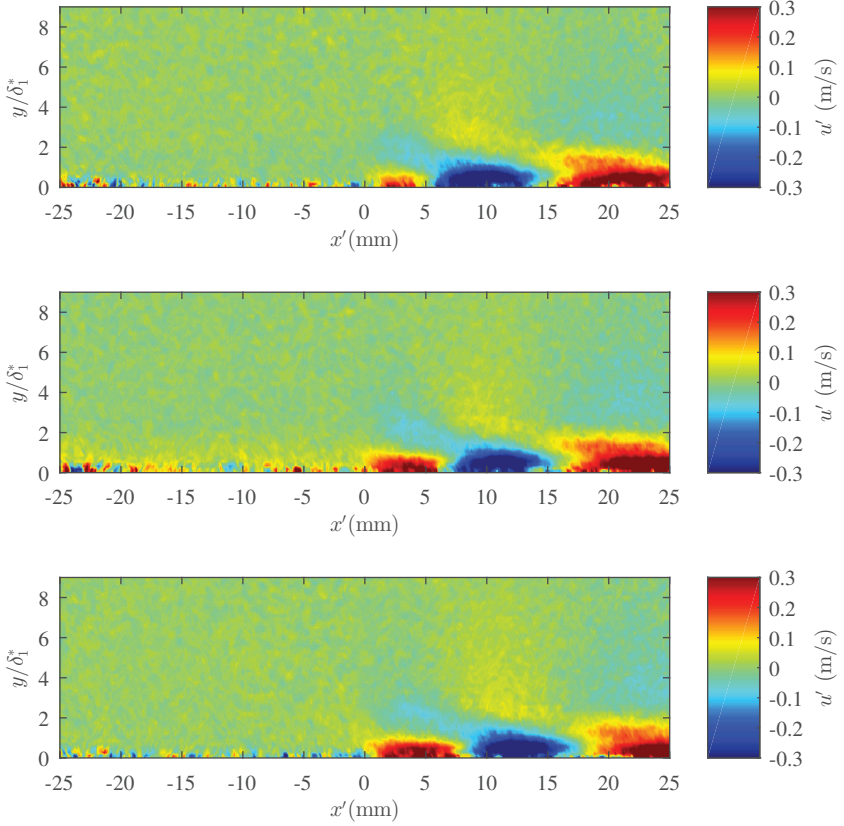


Figure A.1.: Phase-averaged velocity field of u' at $U_e = 15$ m/s at different (relative) phase angles $\Phi_{TS} = \frac{1}{8}\pi$, $\Phi_{TS} = \frac{2}{8}\pi$ and $\Phi_{TS} = \frac{3}{8}\pi$ (top to bottom). The PA force is modulated at $f_{TS} = 250$ Hz and generates counter-waves.

B. Outlook for Future MIMO Controller Operation

For future operation of the MIMO controller, simplifications are discussed in order to reduce the required computational power. Simplifications for the secondary paths (section B.1) as well as the control kernels (section B.2) that could be applied are discussed in the following. Numerical investigations on the simplification of the control paths by Dadfar et al. (2014) propose control units of three spanwise sensors/actuators, which is mainly motivated by the spatial and temporal scales of the perturbation inside the boundary layer. Semeraro et al. (2013) also shows a strong dependence of the sensor spacing and the controller performance.

The simplifications that are discussed in the following have not been tested in an experiment and some may appear too radical. Nevertheless, it should give an outlook for future simplifications of MIMO controller operation. The successful dxLMS approach in Chapter 6 shows that rather radical model simplifications need not lead to lower controller performance.

B.1. Simplifications for the Secondary Paths

The discussion on the transmission behavior in section 7.3 showed that the spanwise connections of G_{lm} are limited. Therefore, the complexity of the secondary path G can be reduced significantly. For the following example, a system of $K = 3$ reference sensors, $M = 3$ actuators and $L = 3$ error sensors is considered. The number of FIR coefficients J of the secondary path (plant) is equal to those of the compensator kernel J ($I = J$) and set to $I = J = 256$.

The investigations in section 7.2.3 showed that only the sensors next to the PA and directly downstream are connected. The secondary path model of the

plant $\hat{\mathbf{G}}$ (2.48) is therefore reduced to:

$$\hat{\mathbf{G}}_j = \begin{bmatrix} \hat{g}_{22j} & \hat{g}_{23j} & 0 \\ \hat{g}_{32j} & \hat{g}_{33j} & \hat{g}_{34j} \\ 0 & \hat{g}_{43j} & \hat{g}_{44j} \end{bmatrix}. \quad (\text{B.1})$$

For further simplification, the entries on the secondary diagonal of (B.1) could be set to zero (Fig. 7.4). Hence, only the entries of the diagonal are left (B.2).

In a 2D laminar boundary layer, the assumption of a spanwise homogeneous transmission behavior is valid (Fabbiane et al. (2017)). This implies that all elements on the main diagonal of (B.2) are equal - but also all elements on the secondary diagonal of (B.1). Figure B.1(a) shows that this is assumption is valid; the FIR filters of the measured secondary paths G_{11} , G_{22} and G_{33} are similar. Figure B.1(b) shows only a minor phase shift because of differences in the steady force of each individual PA electrode. With all the assumptions discussed above, only one transfer path has to be identified or modeled prior to the controller operation as indicated in (B.3). This could be done with the “black box” approach (dxLMS) presented in Chapter 6.

$$\hat{\mathbf{G}}_j = \begin{bmatrix} \hat{g}_{22j} & 0 & 0 \\ 0 & \hat{g}_{33j} & 0 \\ 0 & 0 & \hat{g}_{44j} \end{bmatrix} \quad (\text{B.2})$$

$$\approx \begin{bmatrix} \hat{g}_{22j} & 0 & 0 \\ 0 & \hat{g}_{22j} & 0 \\ 0 & 0 & \hat{g}_{22j} \end{bmatrix}. \quad (\text{B.3})$$

B.2. Simplifications for the Control Kernel

Following the assumptions made above, simplifications can also be made for the control kernel matrix \mathbf{W}_i (2.45). Assuming the limited spanwise influence of each PA in spanwise direction, \mathbf{W}_i simplifies to equation (B.4). If a spanwise homogeneous control law (Fabbiane et al. (2017)) is assumed and the entries on the secondary diagonal are neglected, equation (B.5) is valid. The MIMO control circuit (Fig. 2.9) reduces to a parallel execution of three SISO control circuits, while the adaption of the compensator does only have to be conducted for one channel. One could also think about using all sensors

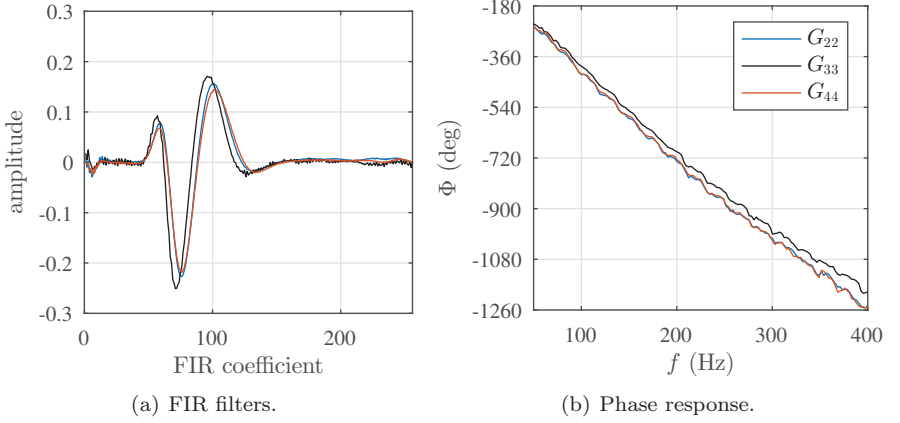


Figure B.1.: Secondary paths G_{11} , G_{22} and G_{33} , measured at $U_{WT} = 12 \text{ m/s}$.

for faster convergence of \mathbf{W} .

$$\mathbf{W}_i = \begin{bmatrix} w_{22i} & w_{23i} & 0 \\ w_{32i} & w_{33i} & w_{34i} \\ 0 & w_{43i} & w_{44i} \end{bmatrix} \quad (\text{B.4})$$

$$\approx \begin{bmatrix} w_{22i} & 0 & 0 \\ 0 & w_{22i} & 0 \\ 0 & 0 & w_{22i} \end{bmatrix}. \quad (\text{B.5})$$

The computational power that is required to calculate the upper part of the block diagram in Fig. 2.9 is influenced by the spanwise homogeneous assumption. The limited spanwise influence of the actuators lead to zero elements in the compensator kernel matrix \mathbf{W}_i . For the case with $K = L = M = 3$, the computation of $\mathbf{u}(n) = \sum_{i=0}^{I-1} \mathbf{W}_i \mathbf{x}(n-i)$ reduces from $M \times K \times I = 9I$ to $3I$ operations.

